Planke, S., Berndt, C., Alvarez Zarikian, C.A., and the Expedition 396 Scientists
Proceedings of the International Ocean Discovery Program Volume 396
publications.iodp.org

Expedition 396 summary[1]

S. Planke, C. Berndt, C.A. Alvarez Zarikian, A. Agarwal, G.D.M. Andrews, P. Betlem, J. Bhattacharya, H. Brinkhuis, S. Chatterjee, M. Christopoulou, V.J. Clementi, E.C. Ferré, I.Y. Filina, J. Frieling, P. Guo, D.T. Harper, M.T. Jones, S. Lambart, J. Longman, J.M. Millett, G. Mohn, R. Nakaoka, R.P. Scherer, C. Tegner, N. Varela, M. Wang, W. Xu, and S.L. Yager[2]

[1] Planke, S., Berndt, C., Alvarez Zarikian, C.A., Agarwal, A., Andrews, G.D.M., Betlem, P., Bhattacharya, J., Brinkhuis, H., Chatterjee, S., Christopoulou, M., Clementi, V.J., Ferré, E.C., Filina, I.Y., Frieling, J., Guo, P., Harper, D.T., Jones, M.T., Lambart, S., Longman, J., Millett, J.M., Mohn, G., Nakaoka, R., Scherer, R.P., Tegner, C., Varela, N., Wang, M., Xu, W., and Yager, S.L., 2023. Expedition 396 summary. In Planke, S., Berndt, C., Alvarez Zarikian, C.A., and the Expedition 396 Scientists, Mid-Norwegian Margin Magmatism and Paleoclimate Implications. Proceedings of the International Ocean Discovery Program, 396: College Station, TX (International Ocean Discovery Program). https://doi.org/10.14379/iodp.proc.396.101.2023
[2] **Expedition 396 Scientists' affiliations.**

Contents

Keywords
International Ocean Discovery Program, IODP, *JOIDES Resolution*, Expedition 396, Mid-Norwegian Margin Magmatism and Paleoclimate Implications, Earth Connections, Climate and Ocean Change, Site U1565, Site U1566, Site U1567, Site U1568, Site U1569, Site U1570, Site U1571, Site U1572, Site U1573, Site U1574, North Atlantic Igneous Province, NAIP, volcanic rifted margin, large igneous province, LIP, Paleogene hothouse, Paleocene–Eocene Thermal Maximum, PETM, Norwegian continental margin

Core descriptions

Supplementary material

References (RIS)

MS 396-101
Published 6 April 2023

Funded by NSF OCE1326927

Abstract

The opening of the northeast Atlantic, starting around 56 My ago, was associated with the emplacement of the North Atlantic Igneous Province, including the deposition of voluminous extrusive basaltic successions and intrusion of magma into the surrounding sedimentary basins. The mid-Norwegian Margin is a global type example of such a volcanic rifted margin and is well suited for scientific drilling with its thin sediment cover and good data coverage. During International Ocean Discovery Program Expedition 396, 21 boreholes were drilled at 10 sites in five different geological settings on the mid-Norwegian Margin. The boreholes sampled a wide variety of igneous and sedimentary settings ranging from lava flow fields to hydrothermal vent complexes, along with thick successions of Upper Paleocene and Lower Eocene strata. A comprehensive suite of wireline logs was collected in eight boreholes. These data provide new constraints for geodynamic models to explain the rapid emplacement of large igneous provinces and will also allow us to test the hypothesis that the Paleocene–Eocene Thermal Maximum (PETM) was caused by hydrothermal release of carbon in response to magmatic intrusions and/or flood basalt eruption. Successful drilling and high core recovery of target intervals at all nine primary sites and one additional alternate site will allow us to achieve these goals during postcruise work. Expedition 396 highlights include (1) drilling and coring a unique, multihole transect across a supra-sill hydrothermal system and crater that was filled in during the PETM, (2) drilling and coring all the major lithofacies at each of the component parts of a volcanic rifted margin from terrestrial to deep marine, and (3) acquiring excellent petrophysical data and imaging support for core analyses of complex and diverse volcanic and volcaniclastic intervals across the terrestrial to marine transition.

1. Introduction

Continental extension, breakup, and the formation of new mid-oceanic spreading centers are fundamental parts of the plate tectonic cycle and have wide implications for the global environment (Berndt et al., 2019). Rifted margin studies have been at the core of the International Ocean Discovery Program (IODP) and its predecessors since the 1960s. Deep Sea Drilling Project (DSDP) and Ocean Drilling Program (ODP) drilling, along with extensive seismic surveying of the northeast Atlantic conjugate margins, demonstrated anomalously high volcanic activity during continental breakup. This led to the classification of these margins as volcanic rifted margins (Talwani and Eldholm, 1977; Eldholm et al., 1987, 1989; Saunders et al., 1998; Sengör and Burke, 1978; Ziegler and Cloetingh, 2004; Abdelmalak et al., 2016a, 2016b) (Figure **F1**).

Expedition 396 builds on previous successful drilling campaigns in the northeast Atlantic (DSDP Leg 38 [1974] and ODP Legs 104 [1985], 152 [1993], and 163 [1995]) that were instrumental in developing the concepts of volcanic rifted margins and large igneous provinces (LIPs) (see Mahoney and Coffin [1997], Ernst [2014], and Svensen et al. [2019] for a summary). There are, however, many unresolved scientific questions related to the formation and environmental implications of breakup volcanism that can only be addressed by new scientific drilling.

Despite unsurpassed constraints on conjugate crustal structure between the northeast Atlantic Norwegian, Jan Mayen, and Greenland rifted margins, the mechanisms behind rift-related, anomalously voluminous magmatic productivity are still debated (Lundin and Doré, 2005; Brown and

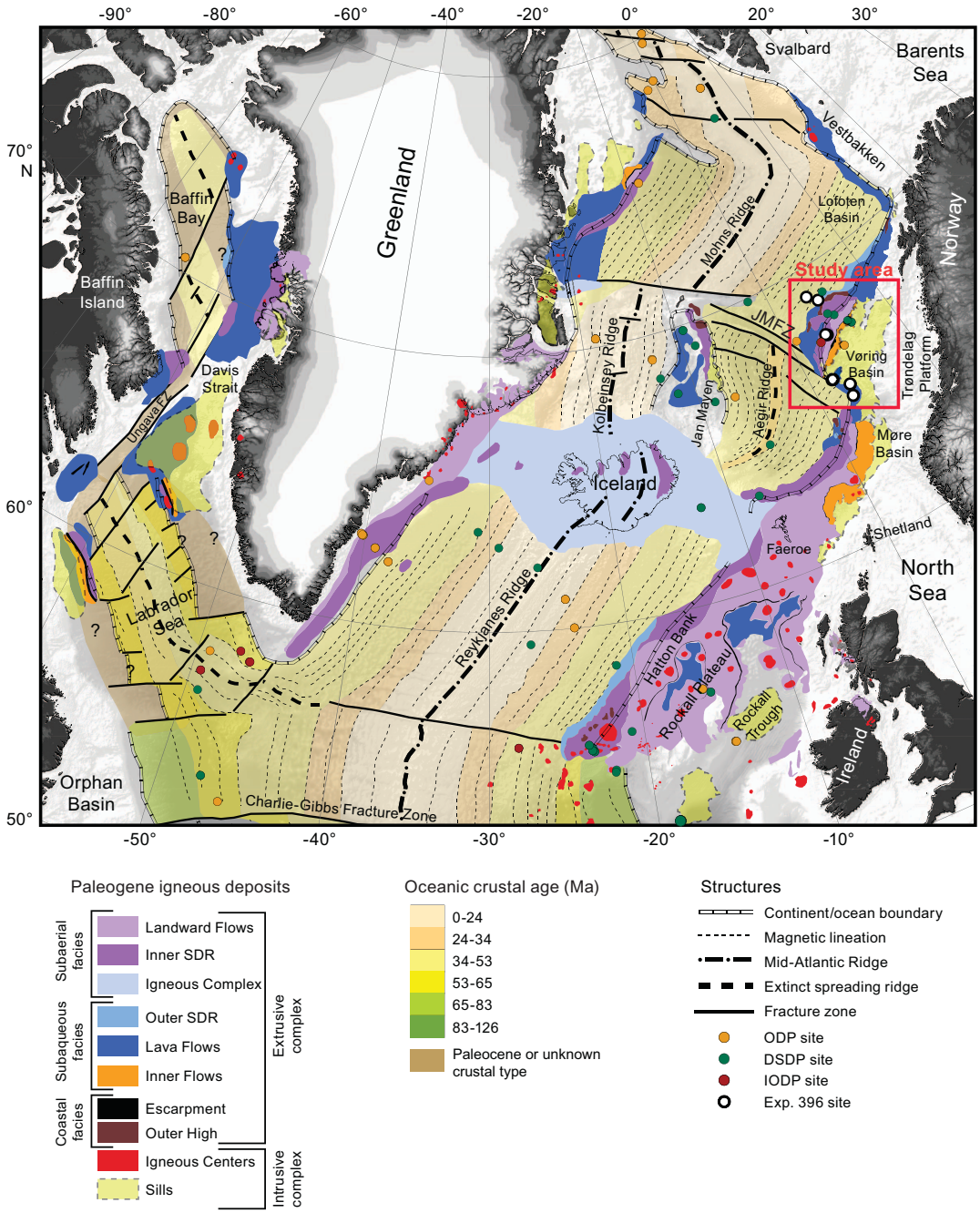

Figure F1. Distribution of Paleogene igneous breakup complexes and oceanic structures in the northeast and northwest Atlantic. Scientific boreholes and proposed drilling sites are shown. Compiled from Abdelmalak et al. (2016a, 2016b, 2017, 2019), Berndt et al. (2001b), Boldreel and Andersen (1994), Davison et al. (2010), Elliott and Parson (2008), Geissler et al. (2016), Reynolds et al. (2017), and Ritchie et al. (1999). JMFZ = Jan Mayen Fracture Zone, FZ = fracture zone.

Lesher, 2014; Foulger et al., 2020; Lu and Huismans, 2021). The controversy centers on three competing hypotheses:

- Excess magmatism derived from elevated mantle potential temperatures resulting from mantle plume processes;
- Small-scale convection at the base of the lithosphere enhancing the flux of material through the melt window during rifting and breakup; and
- Mantle source heterogeneity contributing to anomalously high melt production during continental breakup.

Although the mantle plume mechanism requires anomalously high temperatures resulting in high degrees of partial melting during asthenosphere upwelling, small-scale convection at the base of the lithosphere operates without involving significantly elevated potential temperatures and is inherently connected to the rifting process (Boutilier and Keen, 1999).

Temporal correlations between mass extinctions, global warming, and formation of LIPs have long been recognized but rarely demonstrated (e.g., only in the case of the late Permian extinctions) (Vogt, 1972; Eldholm and Thomas, 1993; Wignall, 2001). However, the reasons for related paleoenvironmental crises are highly debated (Bond and Wignall, 2014; Courtillot and Renne, 2003). For example, volcanic eruptions release large volumes of sulfur, halogens, and carbon to the atmosphere (Jones et al., 2016), which may cause environmental disturbances on a variety of timescales. A potential complementary but perhaps asynchronous mechanism is that large volumes of greenhouse gases can be released from metamorphic aureoles around sill intrusions emplaced in sedimentary basins (Svensen et al., 2004). New information on eruption styles, volumes and rates, and sedimentological data in a proximal region to the eruptions is important to document and understand the environmental impact of LIP emplacement.

2. Background

Scientific drilling of northeast Atlantic continental margins since the 1970s has been essential for understanding the architecture and implications of igneous deposits associated with continental breakup. In particular, drilling of deep boreholes in the feather edge of the seaward-dipping reflectors (SDR) offshore mid-Norway and southeast Greenland (Eldholm et al., 1989; Larsen, Saunders, Clift, et al., 1994; Duncan, Larsen, Allan, et al., 1996; Saunders et al., 1998; Larsen et al., 1999) demonstrated that voluminous subaerial volcanic sequences are common along rifted margins. The drilling results further suggested that continental breakup magmatism has had a major impact on the global environment and mass extinctions (Hinz, 1981; Eldholm and Thomas, 1993). Interpretation of oil and gas industry seismic and borehole data from the Vøring Basin led to the hypothesis that voluminous intrusion of magma in organic-rich sedimentary basin deposits may have triggered the Paleocene–Eocene Thermal Maximum (PETM) by release of aureole gases through hydrothermal vent complexes (Svensen et al., 2004). This hypothesis will be tested with the results of Expedition 396.

Breakup volcanism along rifted margins is highly variable in both time and space. Mantle melting during the formation of mid-oceanic ridges is relatively well understood and mostly a function of spreading rate and mantle potential temperature. It leads to accretion of 6–8 km of magmatic crust at standard mantle potential temperature and full spreading rates greater than 2 cm/y (Bown and White, 1994). On the other hand, factors controlling magmatic activity during continental rifting and breakup are not well known. The variation in the degree of magmatism at rifted margins can, to the first order, be characterized in three contrasting modes of behavior (e.g., Huismans and Beaumont, 2011, 2014; Lu and Huismans, 2021). Mode 1 margins are characterized by a sharp transition from the continent/ocean boundary (COB) to normal thickness (6–8 km) magmatic ocean crust. At Mode 2 margins, magmatic productivity exceeds that expected from decompression melting at normal mantle temperature. Mode 3 margins have little to no magmatism at the COB and a broad transition zone with an exposed mantle at the seafloor preceding formation of mature oceanic crust.

A comprehensive understanding of what controls this range of behaviors and the volume, distribution, and timing of magmatism during continental rifting and breakup is, however, lacking. Magmatic crustal thickening at Mode 2 margins often exceeds 20 km, more than three times as thick as normal oceanic crust produced by passive upwelling of normal potential temperature mantle (i.e., Mode 1). This excess magmatism has been related to both mantle plume and contrasting nonplume mechanisms (McKenzie and Bickle, 1988; Mutter et al., 1988; White and McKenzie, 1989). Continental breakup is often associated with extensive volcanism over large distances along strike of the rifted margins, as exemplified in the northeast Atlantic (Figure **F1**). Magmatic products emplaced along these volcanic rifted margins have four major characteristics:

- Wedges of SDR and associated volcanic seismic facies units interpreted to be massive, subaerial and submarine lava flows and volcaniclastic sediments are found on both sides of the COB;
- Extensive sill and hydrothermal vent complexes are emplaced in organic-rich sedimentary basins around the incipient breakup axis;
- Thick, high–seismic velocity bodies are found in the lower crust along the COB and commonly interpreted to be magmatic underplated material; and
- Extensive pre- to synrifting volcanic sequences that comprise subaerial lava flows, lava deltas, and volcaniclastic sediments are found.

It appears that volcanic rifted margins require mantle that is either anomalously hot, actively upwelling at rates higher than the plate half-spreading rate, anomalously fertile, or some combination of these factors.

2.1. Geological setting

The northeast Atlantic rift system developed as a result of a series of rift episodes succeeding the Caledonian orogeny that ultimately led to continental breakup and passive margin formation in the earliest Eocene (Talwani and Eldholm, 1977; White and McKenzie, 1989; Skogseid et al., 2000; Abdelmalak et al., 2016a; Zastrozhnov et al., 2020). The mid-Norwegian Margin is well covered by 2-D and 3-D reflection and refraction seismic surveys, potential field and heat flow data, and borehole data that allow a refined structural and stratigraphic framework (Figure **F2**) (Brekke, 2000; Gernigon et al., 2003, 2020, 2021; Mjelde et al., 2005; Breivik et al., 2006; Theissen-Krah et al., 2017; Zastrozhnov et al., 2018, 2020; Polteau et al., 2020).

The mid-Norwegian Margin is segmented by the northwest-trending Jan Mayen Fracture Zone, which separates the Møre and Vøring Margins (Figure **F3**). The margin segments are characterized by different tectonomagmatic styles and sediment distributions (Berndt et al., 2001a; Gernigon et al., 2020). The largest magmatic accumulation is observed in the Vøring segment, and volumes decrease to the south and north (Millett et al., 2022). In the southern segment, passive margin formation and oceanic spreading was accommodated by the Aegir Ridge between the Møre and Jan Mayen (at the time connected to Greenland) conjugate margins in the Paleocene and Eocene.

Rifting and passive margin formation in the northeast Atlantic was accompanied by strong volcanic activity (White and McKenzie, 1989; Eldholm and Grue, 1994; Larsen and Saunders, 1998; Wright et al., 2012). Evidence for extensive magmatism is provided by SDR, magmatic intrusions,

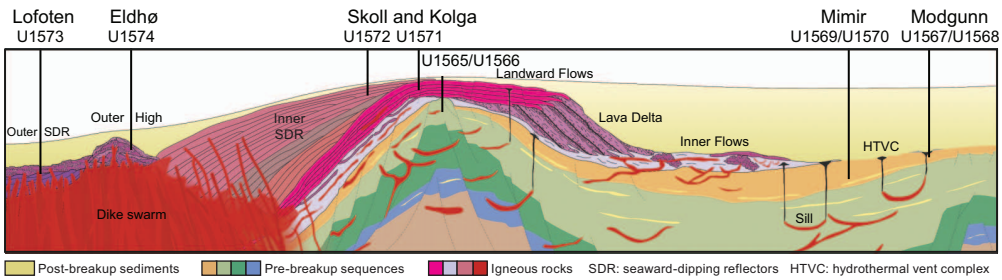

Figure F2. Schematic cross-section through a volcanic passive margin indicating the relative position of the volcanic seismic facies units and Expedition 396 site locations.

and high-velocity bodies at the base of the continental crust underlying the COB, which in the distal margin are unequivocally interpreted to be magmatic underplate (Figures **F2**, **F3**) (Berndt et al., 2001a; Mjelde et al., 2005; Planke et al., 2005). ODP drilling of the Vøring Margin (Leg 104) and off southeast Greenland (Legs 152 and 163) recovered volcanic rock successions erupted during the initial stages of opening of the northeast Atlantic. Drilled rocks range from prebreakup continental tholeiitic flood basalt to synbreakup picrites to oceanic-type basalts that form the main part of the SDR (Fitton et al., 2000). Oceanic-type lavas show an increasing degree of melting and contribution from asthenospheric mantle sources with time (Fram et al., 1998; Fitton et al., 1998). The thickness of igneous crust accreted at the southeast Greenland COB increases from about 18 km

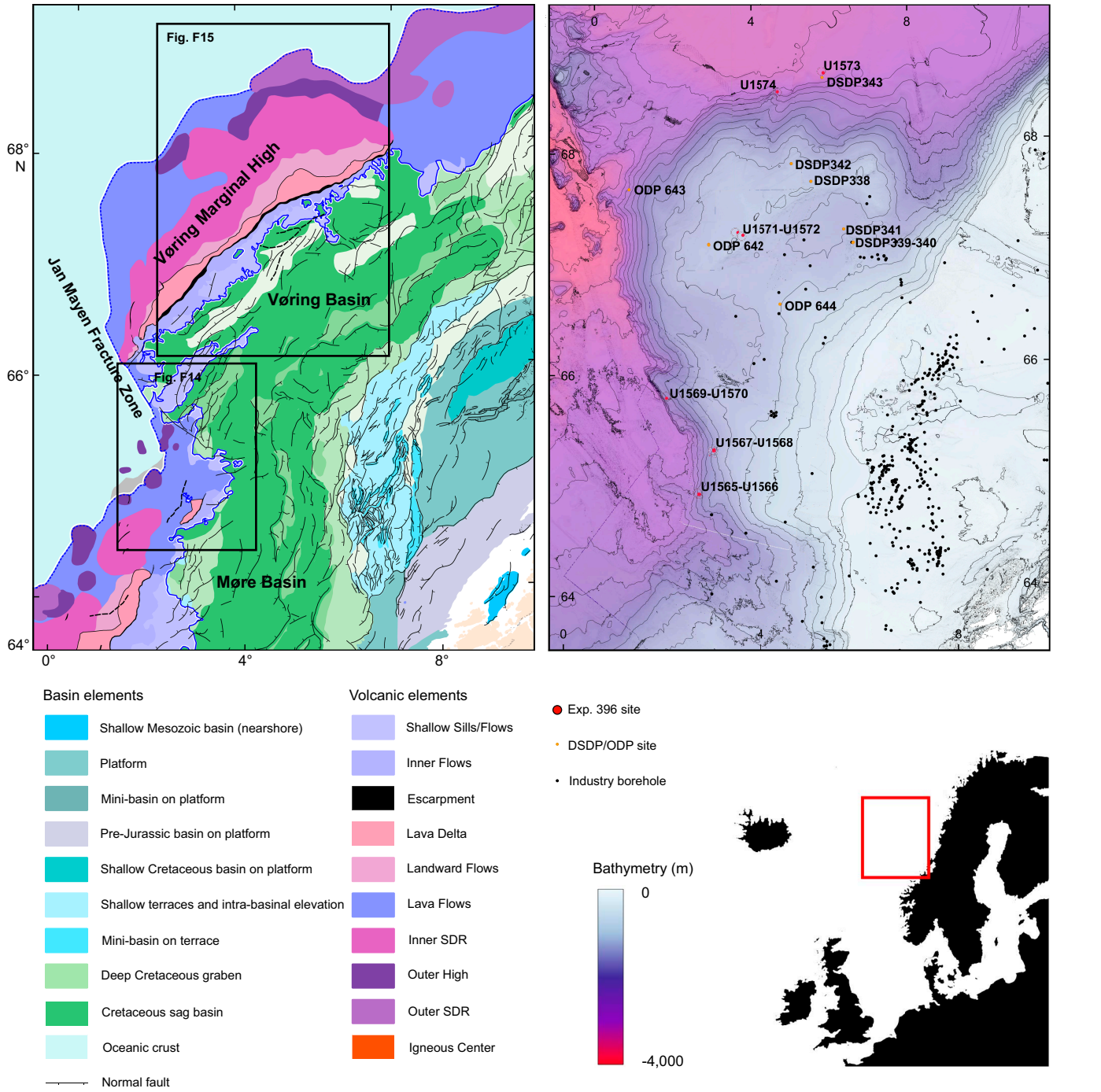

Figure F3. Bathymetric map and structural elements of the study area (after Gernigon et al., 2021). The Vøring Transform Margin is the landward extension of the Jan Mayen Fracture Zone.

in the south to about 30 km near the Greenland-Iceland Rise (Holbrook et al., 2001). Similarly, geochemical enrichment of volcanic rocks of the East Greenland Margin (chondrite-normalized [Ce/Y]N and isotopes; Fitton et al., 1998; Tegner et al., 1998; Brown and Lesher, 2014) increases from south to north. In addition to scientific drilling results, evidence from the thick onshore Faroe Islands and East Greenland exposures reveal a temporal evolution that supports fluctuations in mantle potential temperature with time (e.g., Tegner et al., 1998; Millett et al., 2020). Temporal fluctuations in mantle potential temperature are also invoked from independent geophysical observations, which reveal major uplift and subsidence events during the North Atlantic Igneous Province (NAIP) history that have been invoked as evidence for plume pulsing within the province (e.g., Champion et al., 2008; Hartley et al., 2011; Parnell-Turner et al., 2014).

Correlation of crustal thickness and compositional enrichment suggests a combination of changes in source composition, source temperature, and/or melting dynamics (e.g., Hole and Millett, 2016; Hole and Natland, 2020). It is not known whether a similar correlation of crustal thicknesses and magma compositions exists along the Norwegian Margin. To establish the relationship between chemistry of the volcanic successions and crustal configuration is a milestone of the proposed investigations. Geochemical data show strong chemical and isotopic similarities between the upper series from the Vøring Plateau and southeast Greenland. In contrast, the lower series from both areas are fundamentally different from each other in many aspects, pointing to either substantial differences in prebreakup lithosphere composition at the two localities or different styles of mantle-crust interaction (Abdelmalak et al., 2016a).

Periods of elevated magmatism such as the emplacement of the NAIP often coincide with considerable environmental perturbations. This may include short-term events such as the PETM (56 Ma) or long-term climate warming such as the Early Eocene Climatic Optimum (EECO) (~50–53 Ma) (Bond and Wignall, 2014; Eldholm and Thomas, 1993), or both. The total volume of magma emplaced during the Paleogene is estimated to be 6–10 × 10^6 km^3 (Saunders et al., 2007; Horni et al., 2017), with the most voluminous activity roughly coinciding with the Paleocene/Eocene boundary (Storey et al., 2007a), although volcanism associated with the province spans >10 My (Wilkinson et al., 2017). Greenhouse gas emissions were likely generated by magmatic degassing (Storey et al., 2007b; Gutjahr et al., 2017) and by explosive discharge of thermogenic gases generated by contact metamorphism (Svensen et al., 2004; Frieling et al., 2016; Aarnes et al., 2010). Therefore, the emplacement of the NAIP is one of the primary contenders for instigating hyperthermal events and long-term warming in the Paleogene, either as a direct forcing or as an initiator of positive climate feedbacks such as methane hydrate dissociation.

3. Scientific objectives

The key objectives of Expedition 396 are (1) to understand the relationship between rifting, excess magmatism, and paleoclimate and (2) to resolve the relative contribution from plume upwelling, small-scale convection, and mantle heterogeneity and their relation to the formation of the northeast Atlantic volcanic rifted margins. This requires additional constraints on the following:

- Melting conditions (degree, pressure, and temperature of melting);
- Age distribution of volcanic products, which is essential to constrain magmatic productivity in time and space;
- Variation of pre-, syn-, and postbreakup magmatic activity across the margin;
- Variation of magmatic activity along strike across the major Møre and Vøring Margin segments;
- Eruption rates, environment, and volcanic morphologies; and
- The relationship between climate change and timing, volume, and style of magma emplacement.

The sedimentary proxy-based environmental reconstructions provide a semiquantitative record of paleobathymetry (water depth) and vertical motion as early rifting progressed to seafloor spreading, with the potential additional influence of dynamic support originating from the plume-pulsing hypothesis (e.g., Champion et al., 2008; Parnell-Turner et al., 2014).

Sampling of breakup volcanic successions and proximal sediment cores through IODP drilling, in conjunction with geochemical constraints on melt conditions and integrated quantitative models of melting and mantle convection, is crucial to advance our understanding of breakup processes and resolve competing hypotheses for excess magmatism and paleoenvironmental consequences.

The mid-Norwegian Margin is a unique area in which well-characterized volcanic features related to volcanic rifted margins worldwide are readily drillable (Figure **F3**). Here, igneous rocks and Paleogene sediments are locally buried by thin postbreakup sediment cover. Large regions along the outer margins have recently been covered by industry 3-D seismic surveys, and this unique database allows the identification of shallow (<200 meters below seafloor [mbsf]) volcanic and Paleogene sedimentary targets (Millett et al., 2022).

There were seven scientific objectives for Expedition 396, divided into primary and secondary objectives:

Objective 1 (primary) was to determine the role of the Iceland plume in producing excess magma along the mid-Norwegian segment of the northeast Atlantic volcanic rifted margin during the Paleogene by constraining the conditions of melting (temperature, pressure, mantle sources, and total degree of melting).

Objective 2 (primary) was to determine the cause for along-axis variation in melt production. In the case of the northeast Atlantic volcanic margins, magmatic productivity changes from the Møre Margin (~12–15 km thick magmatic crust) in the south toward the Vøring Margin (>20 km thick magmatic crust) and the Lofoten Margin (~8 km regular thickness magmatic crust). This pattern suggests a local, structural control because models of plume behavior would suggest the largest excess magmatic activity is at the southernmost conjugate sections (e.g., Møre–Jan Mayen) closest to the Iceland thermal anomaly.

Objective 3 (primary) was to determine the environment (subaerial versus submarine) in which the Inner and Outer SDR and the implications for vertical crustal motions during late synrift, breakup, and early postrift oceanic spreading. Some of the lava flows may not have erupted subaerially (e.g., Planke et al., 2000, 2017). This has important implications for the distribution of buoyancy forces and isostasy during breakup where sections without continental crust would, under normal conditions, be expected at water depths >2 km (e.g., Kusznir et al., 2004).

Objective 4 (primary) was to determine the timing of magmatic activity and potential relationship(s) through analysis of a large variety of paleoenvironmental proxies proximal to the NAIP.

Objective 5 (primary) was to use the integrated paleoclimatic and paleoenvironmental proxies, and geochronological data, to assess the relative importance of volcanism and thermogenic release from hydrothermal vent complexes as potential drivers of climate change events.

Objective 6 (secondary) was to study Early Eocene hothouse and freshwater incursions into the North Atlantic. The early Paleogene (~66–45 Ma) was characterized by warm global greenhouse conditions culminating in the EECO (~53–50 Ma), the warmest sustained climates of the last 65 My (Bijl et al., 2009; Anagnostou et al., 2016; Cramwinckel et al., 2018), inducing an intensified hydrological cycle with strongly increased precipitation at high latitudes (e.g., Pagani et al., 2006; Suan et al., 2017). Paleogene sediments obtained during Integrated Ocean Drilling Program Expedition 302 (Arctic Coring Expedition) show large quantities of free-floating freshwater *Azolla*, which grew and reproduced in the Arctic Ocean by the latest early to earliest Middle Eocene (~48 Ma; Brinkhuis et al., 2006). The newly drilled sites penetrate Eocene sediments and will allow testing of the extent of freshwater incursions, constraining paleoceanographic boundary conditions for the incursions, including the evolution of oceanic gateways and their influence on global ocean circulation. The Early Eocene sediments also provide a unique opportunity to reconstruct northern mid–high latitude climate, allowing a detailed comparison to Southern Ocean records (e.g., Bijl et al., 2009, 2013; Hollis et al., 2012).

Objective 7 (secondary) was to study carbon capture and storage in basalt provinces. Industrial-scale injection of CO_2 into volcanic reservoirs has been developed in recent years with test sites in Iceland (Matter et al., 2016) and Washington State (USA; McGrail et al., 2011). Carbon capture

and storage is an integral component of meeting climate change targets of the Intergovernmental Panel on Climate Change (IPCC), and as such, the extensive offshore volcanic sequences of the mid-Norwegian volcanic rifted margin form potential storage targets (Planke et al., 2021). Better petrophysical and geophysical constraints on the volcanic rock sequences collected during Expedition 396 are needed to effectively appraise the reservoir properties and storage potential in this area.

Observations of meteoric water and high dissolved calcium concentration from the bottom of ODP Sites 642 and 643 show that the Vøring Plateau is ideal for studying circulation of freshwater in such large basaltic formations and assessing its potential for CO_2 sequestration. Previous ODP holes did not address the origin of meteoric water and trigger(s) for such large-scale circulation. Dating of borehole water samples with ^{14}C, ^{36}Cl, and $^{234}U/^{238}U$ tracers and systematic analyses of fluid geochemistry (Inagaki et al., 2015) will allow the determination of the source of meteoric waters and provide constraints on their circulation systems, which are crucial for assessing the CO_2 storage potential of breakup basalts. Pore fluids have been sampled along the complete drilling transect to investigate the potential extent of meteoric water flow. The outcome of fluid geochemical analyses will be quantitatively interpreted with hydrological modeling using software such as MODFLOW to investigate the flow path of meteoric water. The sampling for water geochemistry will follow the standard IODP protocol for pore fluid analyses.

4. Operations and coring strategy

The mid-Norwegian Margin is the type locality for volcanic rifted margins and is probably the best studied volcanic margin worldwide. The detailed geometry and amount of volcanic products in the form of underplated bodies and intrusive and extrusive volcanic rocks are well constrained through geophysical imaging (e.g., Mjelde et al., 2005; Berndt et al., 2001b; Planke et al., 2017; Abdelmalak et al., 2016a, 2016b, 2017). However, new information on the age, nature, and depositional environment of the volcanic rocks is required to constrain melt production rates and vertical motions.

Answering the fundamental questions outlined in the scientific objectives required extensive sampling of both late synrift/early postrift sediments and magmatic products from the continental into the oceanic domain (Figures **F2**, **F3**). Collection of sedimentary records proximal to the volcanic and magmatic activity will allow the application of numerous proxies (e.g., geochemical and sedimentological) to distinguish between volcanic and hydrothermal vent complex sources.

The expedition sites were located based on interpretation of very extensive high-quality modern 3-D data, and locally, 2-D profiles where 3-D data did not exist (Millett et al., 2022; Gernigon et al., 2021). All proposed sites were located in regions with thin post-Eocene sediments. Site-specific high-resolution 2-D and 3-D P-Cable seismic data were subsequently acquired in 2020 across six of the approved sites (Bünz et al., 2020).

The expedition boreholes are located along three transects:

- The Modgunn transect targets the crater of a hydrothermal vent complex. Five boreholes were drilled at two sites.
- The Mimir transect targets Paleogene sediments and the PETM. Five boreholes were drilled at two sites.
- The basement transect (Kolga, Skoll, Eldhø, and Lofoten Basin areas) targeted both basalt and interbasaltic sediments, prebasalt, and postbasalt sequences. Eleven boreholes were drilled at six sites.

Drilling was highly successful, with clement weather, smooth operations, and good core recovery. In total, 21 holes were drilled at 10 different sites (Table **T1**). The total drilling depth was 3950 m, including more than 600 m of basement rocks. Overall recovery was 57%; however, the recovery of key PETM and basalt stratigraphic intervals was as high as 78% and 61%, respectively. A comprehensive suite of wireline logs were collected in eight boreholes, with a logged interval of 913 m. A summary of the drilling and logging results from the sites are presented in Figure **F4** and located on a cross-section of the volcanic margin in Figure **F2**. The coring results for each of the main

recovered stratigraphic units are presented in Table **T2**, and a summary of the wireline logging intervals is presented in Table **T3**.

Paleogene sediments were drilled along the 1 and 3 km long Modgunn and Mimir transects (Figures **F5**, **F6**). Initially, the primary sites were drilled in both these areas. Preliminary results from the coring operations, including palynological analyses and physical property interpretations, were integrated with revised interpretation of the high-resolution P-Cable 3-D seismic data to refine the location of additional holes to optimize recovery of the targeted sedimentary strata (e.g., the PETM interval).

The drilling strategy for the basement transect was somewhat more complicated because several different areas along the margin were targeted (Figure **F3**). The two Kolga sites targeted subbasalt and initial basalt sequences, followed by the two Skoll sites, which targeted different volcanic seismic facies units and sequences near the feather-edge of the SDR (Figure **F7A**). Farther north, the Eldhø (Figure **F7B**) and Lofoten Basin sites targeted the characteristic Outer High and Outer SDR volcanic seismic facies units, respectively. A summary of the drilling and logging results from the sites are presented in Figure **F4**.

All basement sites were initially drilled using the rotary core barrel (RCB) coring system for optimal basalt recovery (Figure **F4**). The main site objectives were typically 100 m of basement drilling or drilling to bit destruction. Half-coring was used extensively in the basement intervals to improve recovery. Wireline logs were acquired in most basement holes; the main objective was to image interbasaltic sediments and fracture intervals that are difficult to recover with the RCB system. The advanced piston corer (APC) and extended core barrel (XCB) coring systems were used at three basement sites (two at Skoll and Eldhø) to optimize recovery of the Eocene sedimentary

Table T1. Hole summary, Expedition 396. — = not applicable. **Download table in CSV format.**

Hole	Longitude (WGS84)	Latitude (WGS84)	Water depth (m)	Penetration (m)	Drilled interval (m)	Cored interval (m)	Recovered length (m)	Recovery (%)	Total cores (*N*)	APC cores (*N*)	HLAPC cores (*N*)	XCB cores (*N*)	RCB cores (*N*)	Start date (2021)	Start time UTC (h)	End date (2021)	End time UTC (h)	Time on hole (days)
U1565A	2°44.989′E	64°57.761′N	2072	28.0	—	28.0	4.21	15.04	4	0	0	0	4	14 Aug	1600	15 Aug	1515	0.97
U1565B	2°44.845′E	64°57.804′N	2070	31.7	—	31.7	15.45	48.74	5	0	0	0	5	15 Aug	1515	16 Aug	0215	0.46
				Site U1565 totals:	0	59.7	19.66	31.89	9	0	0	0	9					1.43
U1566A	2°43.753′E	64°57.887′N	2099	181.7	—	181.7	100.50	55.31	33	0	0	0	33	16 Aug	0400	21 Aug	0754	5.16
				Site U1566 totals:	0	181.7	100.50	55.31	33	0	0	0	33					5.16
U1567A	3°3.256′E	65°21.851′N	1703	195.9	—	195.9	181.58	92.69	23	6	1	16	0	21 Aug	1205	23 Aug	0640	1.77
U1567B	3°3.208′E	65°21.768′N	1704	83.0	25	58.0	55.29	95.33	10	3	0	7	0	23 Aug	0640	23 Aug	1850	0.51
U1567C	3°3.219′E	65°21.785′N	1705	106.0	30	76.0	66.48	87.47	13	2	0	11	0	26 Aug	2005	27 Aug	1340	0.73
				Site U1567 totals:	55	329.9	303.35	91.83	46	11	1	34	0					3.01
U1568A	3°3.109′E	65°21.594′N	1704	200.0	—	200.0	156.61	78.31	28	7	0	21	0	23 Aug	1936	25 Aug	2200	2.10
U1568B	3°3.154′E	65°21.663′N	1706	94.6	30	94.6	82.76	87.48	16	2	0	14	0	25 Aug	2201	26 Aug	1920	0.89
				Site U1568 totals:	30	294.6	239.37	82.90	44	9	0	35	0					2.99
U1569A	2°1.608′E	65°49.878′N	2171.1	404.0	—	404.6	144.91	35.82	44	0	0	0	44	27 Aug	1759	30 Aug	2020	3.10
				Site U1569 totals:	0	404.6	144.91	35.82	44	0	0	0	44					3.10
U1570A	1°59.623′E	65°49.890′N	2196.4	200.0	—	200.0	98.59	49.30	36	0	0	0	36	30 Aug	2020	1 Sep	1159	1.65
U1570B	1°57.361′E	65°49.679′N	2270	163.5	—	163.6	71.42	43.66	25	0	0	0	25	1 Sep	1159	3 Sep	0100	1.54
U1570C	1°58.707′E	65°49.849′N	2225	200.0	—	200.0	49.59	24.80	23	0	0	0	23	3 Sep	0100	4 Sep	0030	0.98
U1570D	1°59.174′E	65°49.871′N	2207	200.0	—	200.0	50.49	25.25	28	0	0	0	28	4 Sep	0030	5 Sep	2348	1.97
				Site U1570 totals:	0	763.6	270.09	35.75	112	0	0	0	112					6.14
U1571A	3°44.250′E	67°18.402′N	1205.7	247.6	—	247.6	116.55	47.07	39	0	0	0	39	6 Sep	0952	10 Sep	0730	3.9
U1571B	3°44.277′E	67°18.402′N	1205.3	143.7	—	143.7	112.51	78.30	20	7	0	13	0	10 Sep	0730	11 Sep	1351	1.26
				Site U1571 totals:	0	391.3	229.06	62.685	59	7	0	13	39					5.16
U1572A	3°37.162′E	67°19.847′N	1206	330.5	—	330.5	139.53	42.22	46	0	0	0	46	11 Sep	1345	15 Sep	0400	3.59
U1572B	3°37.057′E	67°19.918′N	1206	224.3	—	224.3	218.35	97.35	33	16	13	4	0	15 Sep	0400	16 Sep	1612	1.51
				Site U1572 totals:	0	554.8	357.88	69.785	79	16	13	4	46					5.10
U1573A	5°47.688′E	68°45.624′N	3167	440.9	300	140.9	100.97	71.66	18	0	0	0	18	17 Sep	0153	21 Sep	0705	4.22
				Site U1573 totals:	300	140.9	100.97	71.66	18	0	0	0	18					4.22
U1574A	4°38.436′E	68°36.011′N	2825	260.0	—	260.0	88.41	34.00	38	0	0	0	38	24 Sep	1200	30 Sep	0520	5.72
U1574B	4°38.463′E	68°36.012′N	2825	9.5	—	9.5	9.72	102.32	1	1	0	0	0	30 Sep	0520	30 Sep	1530	0.42
U1574C	4°38.463′E	68°36.001′N	2819	171.5	—	171.5	174.97	102.02	20	19	0	1	0	30 Sep	1530	2 Oct	0231	1.46
				Site U1574 totals:	0	441.0	273.10	79.45	59	20	0	1	38					7.60
				Expedition 396 totals:	385	3562.1	2038.89	57.24	503	63	14	87	339					

rocks. APC coring was guided and constrained by results from the somewhat limited recovery in previously drilled RCB holes at each site. Half-length APC (HLAPC) coring was used extensively to ensure high recovery in critical intervals (Figure **F8**). This approach gave an almost complete recovery of the postbasalt sediments at two sites.

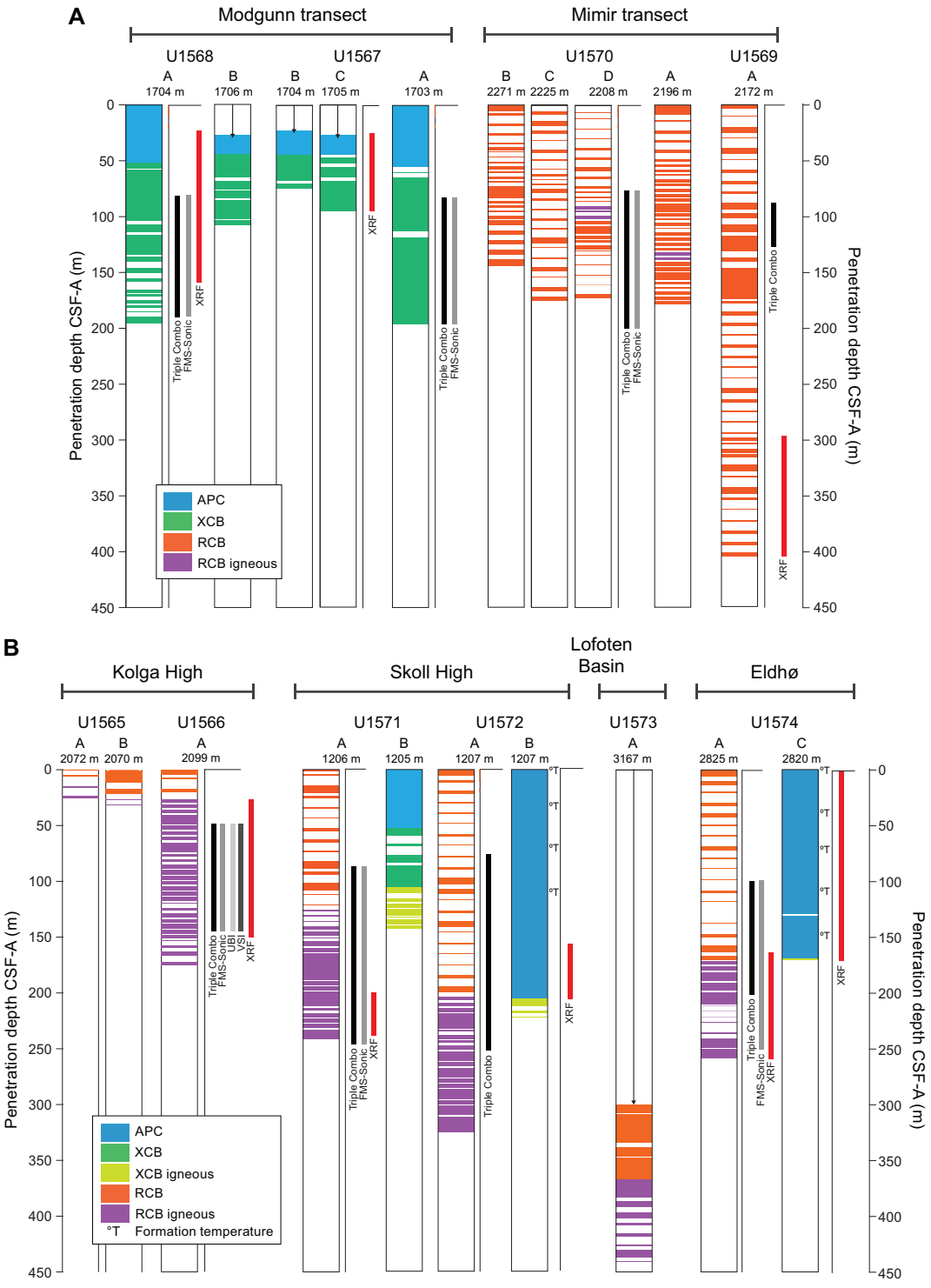

Figure F4. Sites, recovery, and downhole measurements, Expedition 396. A. Transects that addressed PETM causes and evolution at Modgunn Arch and Mimir High. B. Transects that addressed igneous basement objectives, including sampling of the subbasalt geology at Kolga High, the Inner SDR units at Skoll High, the Outer High at Eldhø, and the Outer SDR in the Lofoten Basin. FMS = Formation MicroScanner, XRF = X-ray fluorescence, UBI = Ultrasonic Borehole Imager, VSI = Versatile Seismic Imager.

The typical IODP shipboard workflow, including core description, imaging, physical property measurements, and geochemical analyses of rocks and fluids, was followed by the shipboard scientists and IODP staff. Headspace gas was routinely analyzed for safety reasons. Interstitial water (IW) and microbiological samples were also obtained soon after core recovery. Table **T4** gives an overview of the comprehensive amount of data acquired in the targeted stratigraphic intervals during the cruise. Figures **F9**, **F10**, **F11**, **F12**, and **F13** highlight results from the different shipboard laboratories (biostratigraphy, core description, geochemistry, wireline logging, and paleomagnetism groups).

Table T2. Target interval core recovery, Expedition 396. **Download table in CSV format.**

Target interval	Thickness (m)	Recovery (m)	Recovery (%)	Holes
Oligocene–Holocene	969	531	55	19
Eocene	1000	575	57	15
PETM	308	240	78	8
Paleocene	647	311	48	9
Basalt	587	357	61	8
Granitoids	44	15	34	3
Total cored:	3555	2028	57	21
Total drilled:	3950			

Table T3. Downhole measurements summary, Expedition 396. **Download table in CSV format.**

					Triple combo (m)				FMS-sonic (m)				UBI (m)			
Hole	Water depth (m)	Total depth DSF (m)	Pipe depth WMSF (m)	Top basalt WMSF (m)	Top depth	Bottom depth	Total thickness	Basalt thickness	Top depth	Bottom depth	Total thickness	Basalt thickness	Top depth	Bottom depth	Total thickness	Basalt thickness
U1566A	2099	182	46	24	46	140	95	94	57	140	83	83	57	140	83	83
U1567A	1703	196	84		84	195	111		76	197	122					
U1568A	1704	200	82		82	188	106		82	186	104					
U1569A	2171	405	82		84	128	44									
U1570D	2208	200	72		72	196	124		72	195	123					
U1571A	1206	248	87	117	86	247	161	130	86	248	162	131	129	237	109	109
U1572A	1207	331	87	209	87	250	163	41								
U1574A	2825	260	105	171	104	213	109	42	147	248	101	77				
					Total logged interval:		913	307			695	291			192	192
					Logged sediment interval:		606				404					

Wireline logs. VSI: 17–137 m (11 stations) in Hole U1566A
APC temperature 2 wells 7 temps

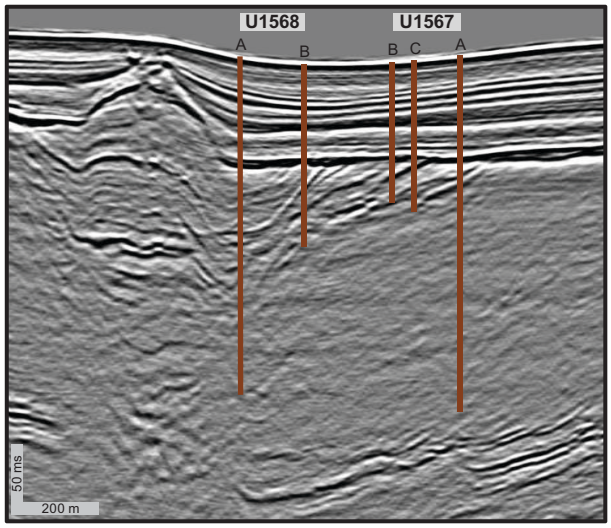

Modgunn Transect
Upper part of a hydrothermal vent complex

Two sites	U1567 and U1568
Five holes	85 to 200 m deep (total 710 m)
Core recovery	543 m core recovered, described and analyzed
Wireline logs	Two holes logged; conventional and Formation MicroScanner (FMS) runs
Lithologies	Dominantly mud, mudstones, and ash layers
Age range	Quaternary to middle Paleocene age, including potential PETM interval
Seismic data	High-resolution P-Cable 3D seismic data from CAGE20-4 cruise (Bünz, 2020)

Figure F5. High-resolution 3-D seismic data showing the position of Site U1567 and U1568 holes along the Modgunn Transect across the upper part of a hydrothermal vent complex.

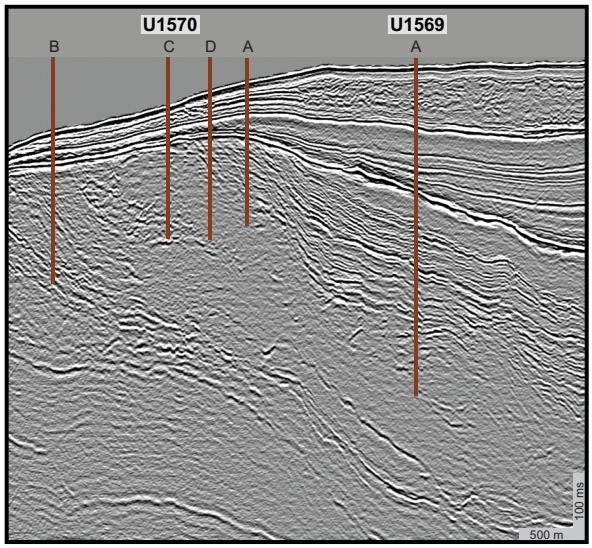

Mimir Transect

Paleogene sediments and PETM

Two sites	U1569 and U1570
Five holes	1179 m of penetration
Core recovery	415 m core recovered, described and analyzed
Wireline logs	One hole logged with conventional and Formation MicroScanner (FMS) runs
Lithology	Mix of mud, mudstones, carbonates, igneous units and ash layers
Age range	Quaternary to Paleocene ages, including PETM interval
Seismic data	High-resolution P-Cable 3D seismic data from CAGE20-4 cruise (Bünz, 2020)

Figure F6. Arbitrary high-resolution 3-D seismic line along the Mimir Transect on the Vøring Transform Margin showing the relative location of Site U1569 and U1570 boreholes.

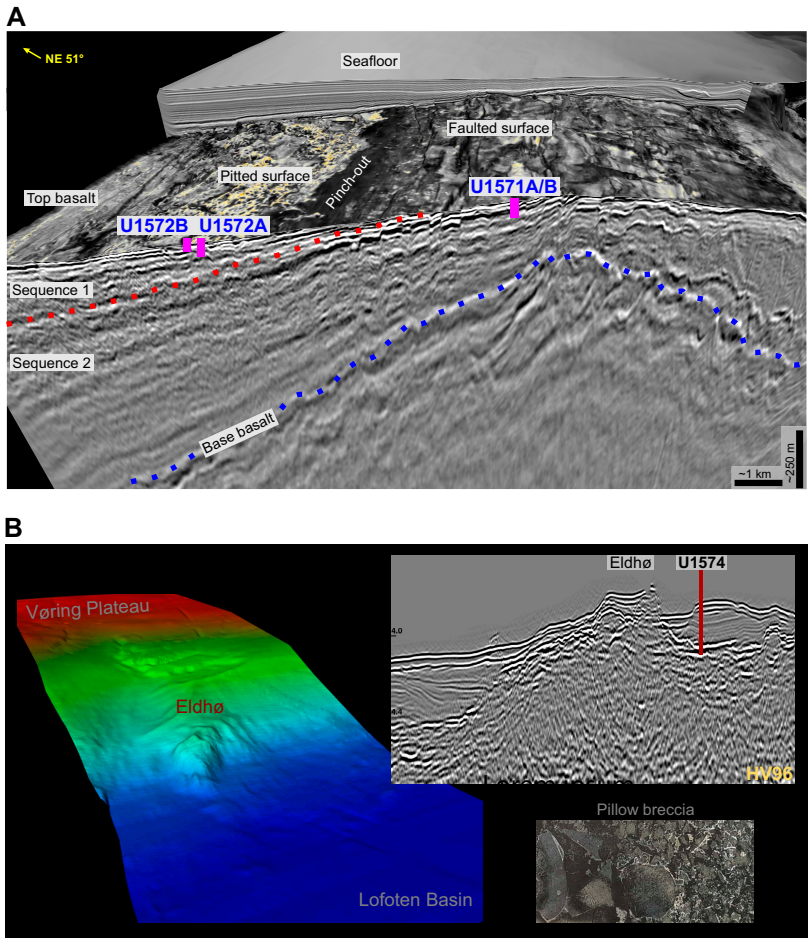

Figure F7. Basement transect, Expedition 396. A. 3-D seismic view of Sites U1571 and U1572. Note the distinct difference in top basalt morphology between the two sites: smooth but faulted at Site U1571 and pitted at Site U1572. B. Site U1574 on the southern flank of Eldhø recovered hyaloclastites and pillow basalts below Eocene sediments. Seismic data from the NPD (HV96 survey) and 3-D view of bathymetry viewed toward the south are included. Depths: Lofoten Basin = ~3200 m, Vøring Plateau = ~1500 m.

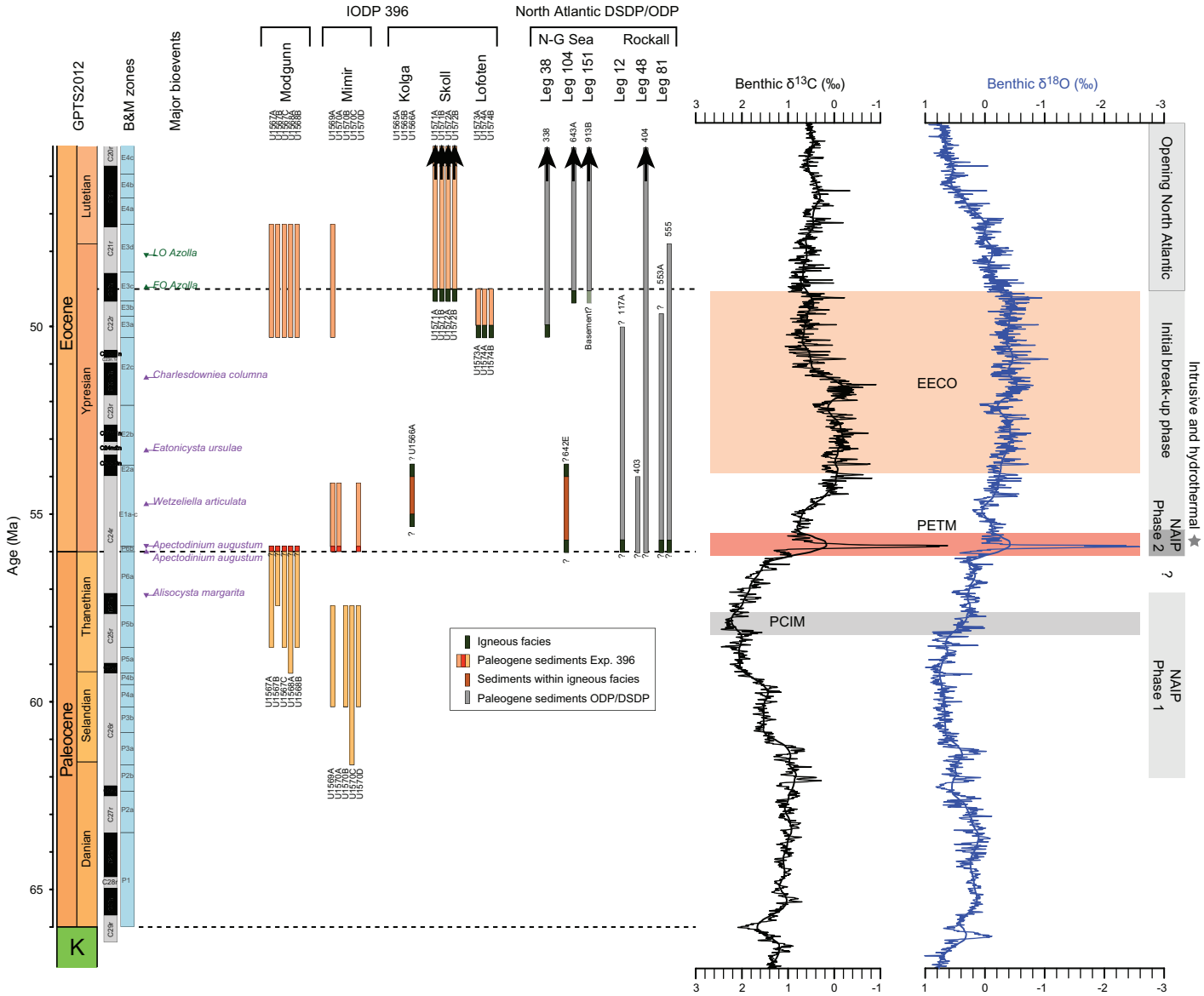

Figure F8. Age of cored intervals with respect to target intervals and existing borehole information for the northeast Atlantic margins. GPTS2012 = geomagnetic polarity timescale of Ogg (2012), B&M zones = zonation by Bujak and Mudge (1994), PCIM = Paleocene Carbon Isotope Maximum.

Table T4. Summary of onboard measurements of target intervals, Expedition 396. Gantry = Section Half Measurement Gantry, WRMSL = Whole-Round Multisensor Logger, MAD = moisture and density, SHMSL = Section Half Multisensor Logger, GRA = gamma ray attenuation, CHNS = carbon-hydrogen-nitrogen-sulfur, ICP-AES = inductively coupled plasma–atomic emission spectrometry, XRD = X-ray diffraction, pXRF = portable X-ray fluorescence spectrometry, PMAG = paleomagnetism. **Download table in CSV format.**

Shipboard data and number of measurements	Post-Eocene	Eocene	PETM interval	Paleocene	Basalt interval	Granitoids	Barren	Total
Core recovery (m)	501	432	240	311	356	15		1,854
Recovery (%)	52	43	78	48	61	34		52
P-wave caliper (Gantry)	898	892	226	392	2,225	82		4,715
P-wave (WRMSL)	12,409	13,763	3,990	5,456	85			35,703
Discrete samples: *P*-wave and MAD	443	185	49	23	93	12		805
Magnetic susceptibility (SHMSL + WRMSL)	38,805	42,722	17,491	22,192	25,379	834		147,423
GRA bulk density (WRMSL)	18,788	20,333	8,230	10,503	11,281	377		69,512
Thermal conductivity	124	89	9	2	54	5		283
Interstitial water (IW)	137	101	28	48	15			329
Carbonates and organics (coulometry and CHNS)	135	110	35	51	19			350
Headspace gas	39	31	20	22	7			119
ICP-AES (hard rock)	5	1			121	6		133
XRD	116	118	72	142	58			506
pXRF	24	41	5		399	17		486
Source rock analyzer (SRA)	13	21	31	25				90
Biostratigraphy	121	96	25	61			67	370
PMAG cubes (JR6 and Kappabridge)	97				83	3		183
PMAG sections (2.5 cm intervals measured)	1,226				281			389,577
Thin sections	14				36	3		53

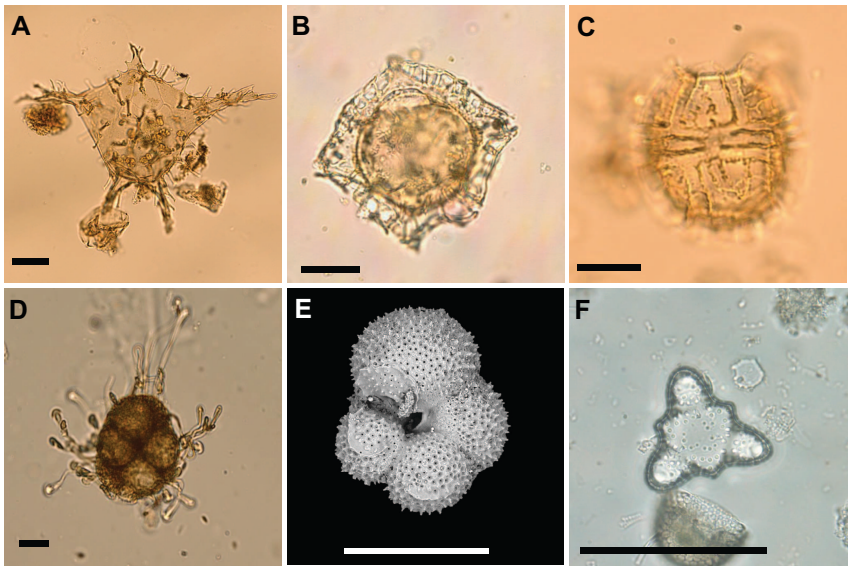

Figure F9. Selected microfossils. A. *Apectodinium augustum*, the dinoflagellate cyst marker taxon for the PETM age. B. Dinoflagellate cyst *Charlesdowniea columna* (Hole U1572B). C. Dinoflagellate cyst *Alisocysta margarita* (Hole U1567A). D. Massulae of *Azolla* spp. (Hole U1572A). E. Planktonic foraminifer *Acarinina* sp. (Hole U1574A). F. Diatom *Sheshukovia flos* (Hole U1567A). Scale bar = ~25 µm for A–D and F and ~200 µm for E.

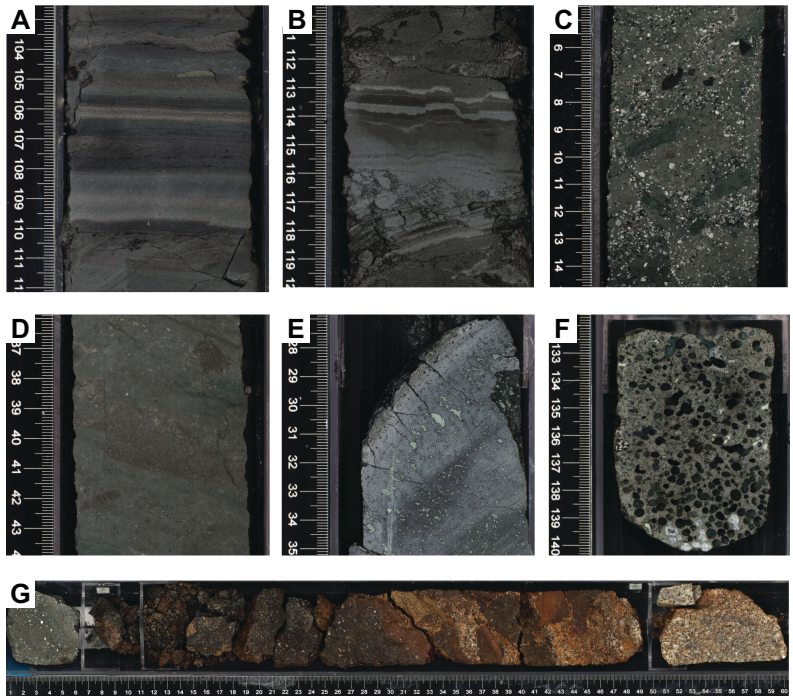

Figure F10. Typical lithologies recovered from Site U1566 at the Kolga High. Lithologies for Sites U1573, U1569, U1570, U1574, and U1566 are also shown. A. Dark gray organic-rich claystone with sand and thin parallel lamination (Early Eocene; 396-U1573A-7R-1). B. Very dark gray claystone with silt and dark gray to black ash (Early Eocene; 396-U1569A-36R-1). C. Dark green tuffaceous siltstone (earliest Eocene/PETM; 396-U1570D-20R-CC). D. Dark greenish gray to very dark gray bioturbated claystone with silt (Late Paleocene; 396-U1570C-13R-1). E. Aphyric pillow basalt (Early Eocene; 396-U1574A-20R-1). F. Highly vesicular aphyric basalt (Early Eocene; 396-U1566A-27R-1). G. Contact between aphyric basalt (Early Eocene) and alkali granite with biotite (29R-1).

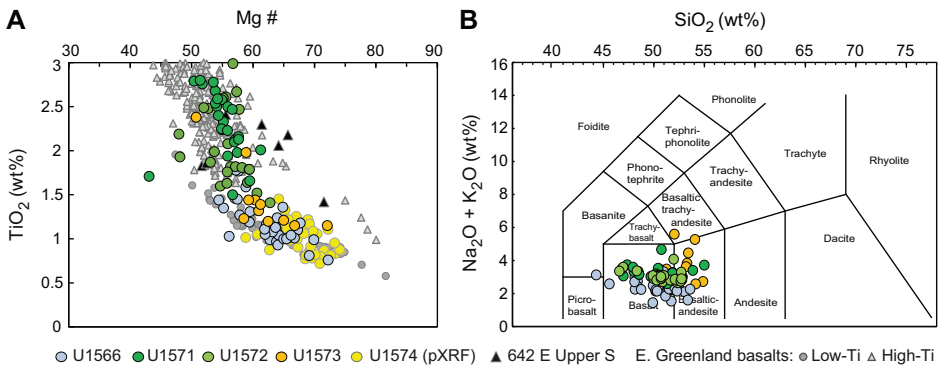

Figure F11. Geochemical composition of igneous rocks, Sites U1566 and U1571–U1573 (ICP-AES) and Site U1574 (pXRF). Compositions are compared with basalts recovered in Greenland (Tegner et al., 1998) and the upper basalt series of ODP Hole 642E (Leg 104; Meyer et al., 2009). Note the affinity of Site U1566 and U1574 basalts with low-Ti basalts and the affinity of the Site U1571 and U1572 basalts with high-Ti basalts. In (B), concentrations of SiO_2 were normalized to 100 wt%.

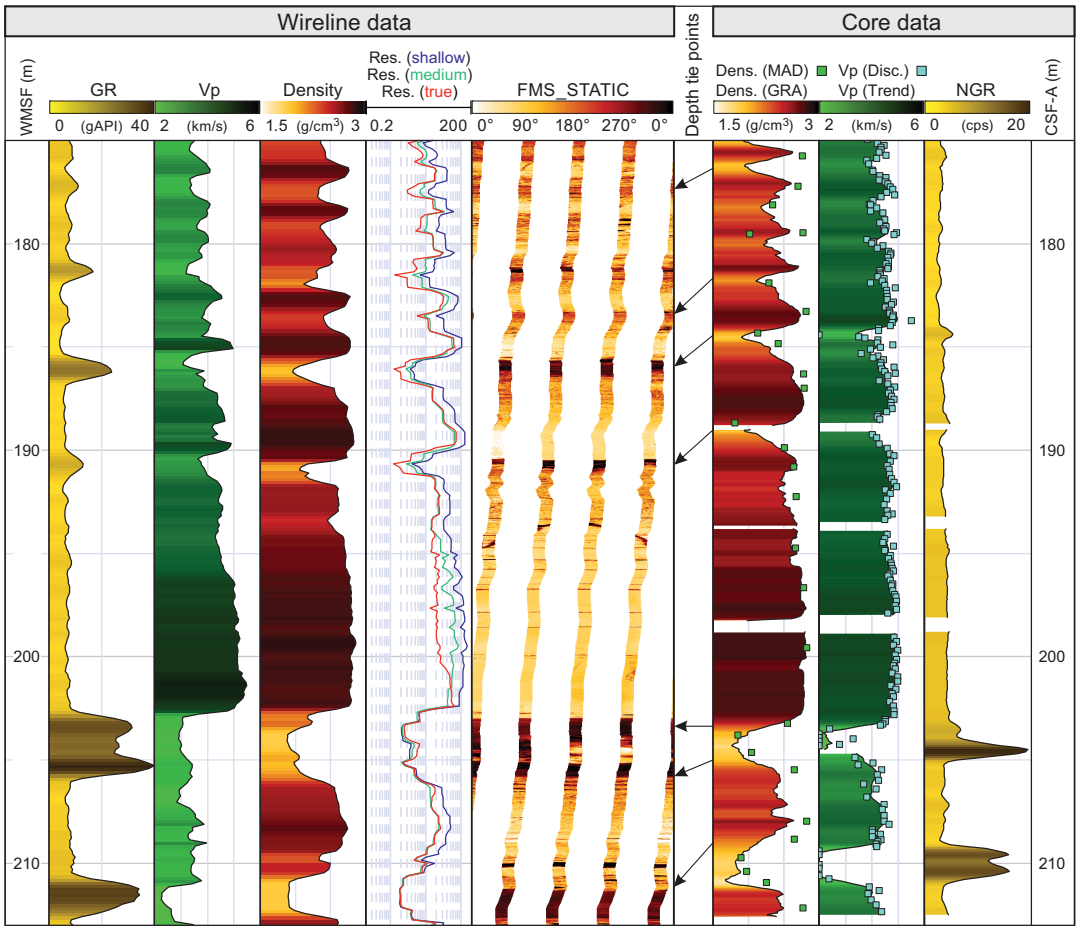

Figure F12. Downhole wireline log and discrete core-based physical property data, Hole U1571A. WMSF = wireline log matched depth below seafloor, GR = natural gamma ray logging tool, Res. = resistivity, Dens. = density, Disc. = discrete, cps = counts/s.

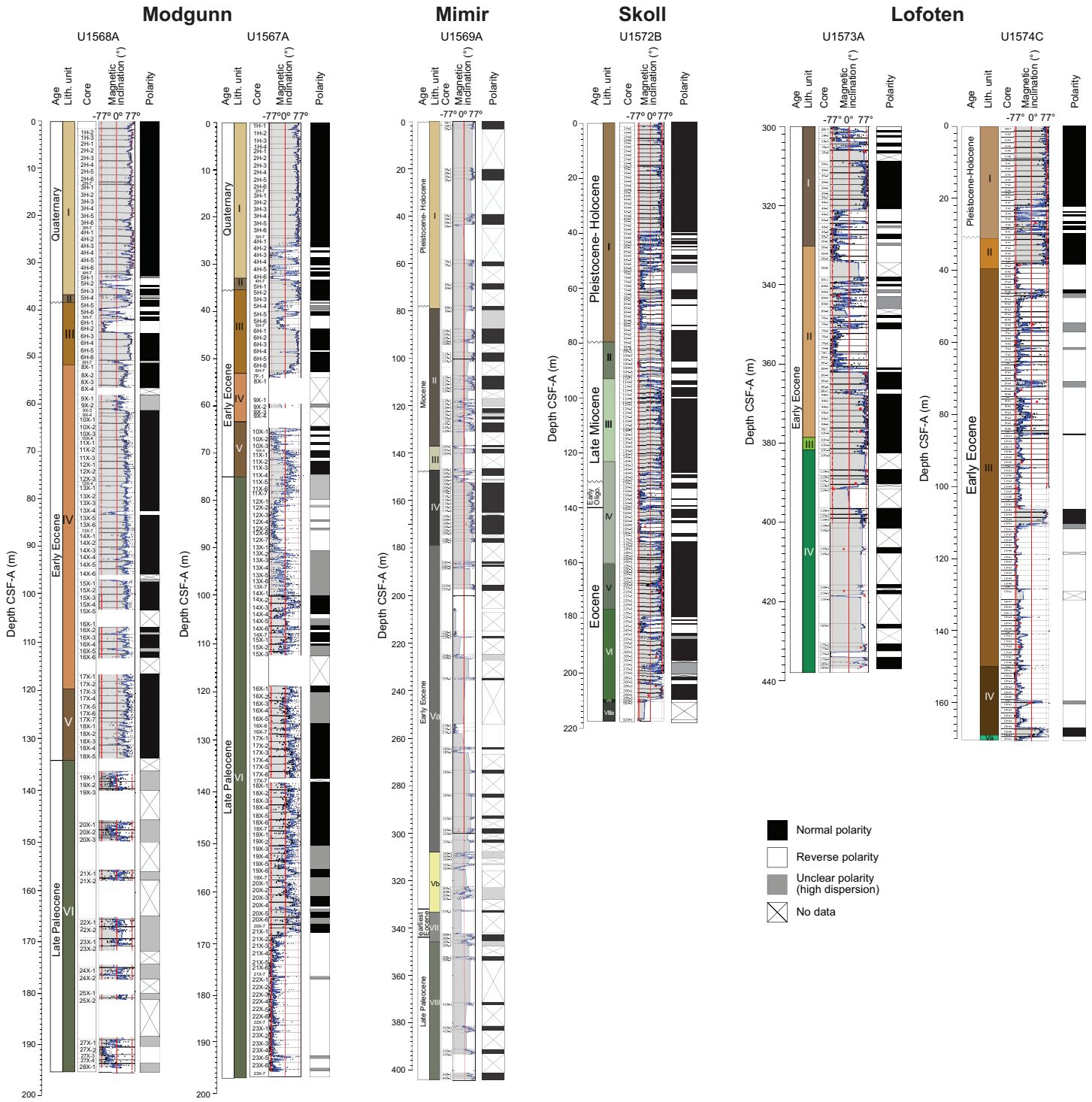

Figure F13. Magnetic inclination measured on the superconducting rock magnetometer for Sites Modgunn (Holes U1568A and U1567A), Mimir (Hole U1569A), Skoll (Hole U1572B), and Lofoten (Holes U1573A and U1574C).

5. Site summaries

5.1. Site U1565

Two short holes were drilled at Site U1565 to determine the nature of the subbasalt basement in the western part of the Kolga High. Both holes recovered altered granitic basement below ~25 m of Quaternary sediments.

5.1.1. Background and objectives

Site U1565 is located at 2071 meters below sea level (mbsl) on the western flank of the Kolga High, a pronounced structural high in the Jan Mayen Corridor (Figure **F14**). The site was located using a combination of conventional 3-D and high-resolution seismic data. Comprehensive 3-D seismic mapping shows that the Kolga High is covered by a variable-thickness Paleogene basalt unit overlying a complex and previously untested subbasalt sequence that had been interpreted as potentially sedimentary because of the presence of local intrusions of Paleogene sills and dikes (Millett et al., 2022; Zastrozhnov et al., 2020). SDR wedges exist on the Møre Marginal High toward the south, and similar but smaller seismic reflections lap onto the western part of the Kolga High. A classic lava delta and escarpment defines the eastern limit of the high. The basalt cover is absent in two small (5 km × 3 km sized) areas just west of the summit of the Kolga High (Millett et al., 2022). Here, the seismic data show a transparent seismic basement that extends down to a strong seismic reflection at about 7.5 s two-way traveltime (TWT). The gap in the basalt cover makes the Kolga High a unique place on the Vøring and Møre Margins where the subbasalt sequence can be sampled with shallow coring.

The primary objective of Site U1565 was to core and sample the subbasalt geology that is largely unconstrained along the mid-Norwegian Margin. Sampling the subbasalt succession would provide important constraints on the rifting history both in time and space, as well as constraints on the vertical movements of this margin segment prior to breakup (Gernigon et al., 2015, 2020). We expected to sample the subbasalt rocks after penetrating about 25–30 m of Quaternary sediments. The plan was to core for 2 days or to a maximum depth of 200 mbsf to recover representative samples of the basement rocks to characterize the lithologies and alternation. We encountered

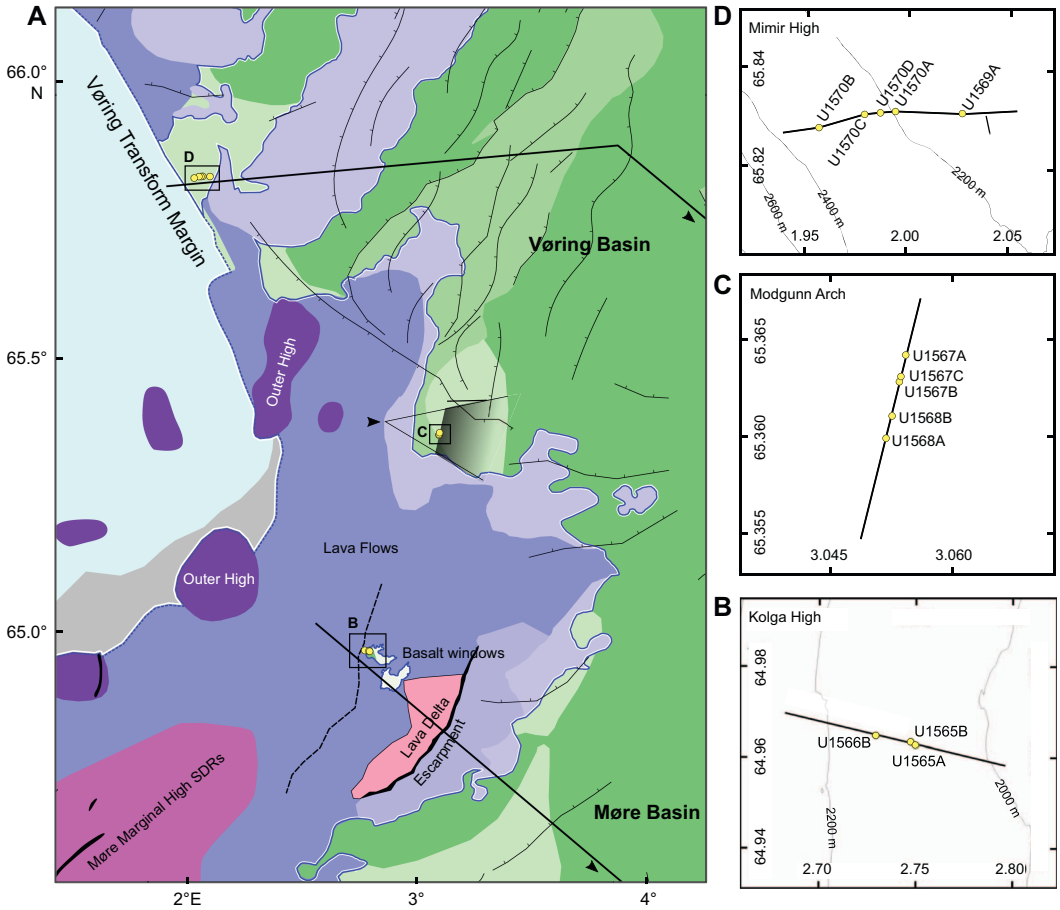

Figure F14. A. Tectonic and magmatic elements of the Jan Mayen Corridor. Geology from Gernigon et al. (2021); legend in Figure F3. B. Kolga High (see Figures F2 and F3 in the Site U1565 chapter [Planke et al., 2023a]). C. Modgunn Arch (see Figures F1 and F2 in the Sites U1567 and U1568 chapter [Planke et al., 2023d]. D. Mimir High (see Figures F1 and F2 in the Sites U1569 and U1570 chapter [Planke et al., 2023e]).

altered granitic basement immediately below the soft-sediment cover in Hole U1565A; therefore, we decided to drill a second hole approximately 140 m west to verify the lateral continuity of the basement rocks rather than spending time deepening the initial hole at a very low penetration rate.

5.1.2. Operations

Site U1565 consists of two shallow holes. Hole U1565A was cored using the RCB system to 28.0 mbsf. Coring was stopped because of very slow penetration rates while drilling into granitoid that was sampled in Cores 3R and 4R. With the objective to confirm the lateral extent of the granite, Hole U1565B was added. This hole was drilled 138 m west-northwest of the first hole in the direction of the next site (U1566). Hole U1565B was cored to 31.7 mbsf and yielded core material similar to that recovered in Hole U1565A. Operations were ended at 0215 h on 16 August 2021, and the drill string was pulled clear of the seafloor to begin the short transit of 900 m to the next site.

Nine cores were recorded for the site. The RCB system was used exclusively (Figure **F4**). It cored 59.7 m and recovered 19.66 m of core (32.9%). A total of 34.25 h or 1.4 days were spent on Site U1565.

5.1.3. Principal results

5.1.3.1. Lithostratigraphy

The lithology of Holes U1565A and U1565B is divided into two lithostratigraphic units. Unit I consists of unconsolidated sediment, and Unit II consists of altered monzogranite. The boundary between the two units was determined using the drilling data where the bit depth shows a sharp decrease in the rate of penetration from about 15 to 1–2 m/h at 20.9 mbsf in U1565A and 28.0 mbsf in U1565B. The thicknesses of granite drilled in Holes U1565A and U1565B are 7.1 and 3.6 m, respectively. Unit I is 7.1 m thinner in Hole U1565A than in Hole U1565B. High-resolution seismic data show that the expected sediment thickness is the same in both holes. The thickness discrepancy in the drilling data is attributed to uncertainties in the determination of the seabed depth for RCB drilling because seabed depth was determined using the increase in torque in Hole U1565A and the mudline recovery in Hole U1565B.

Unit I sediments in Hole U1565A are primarily composed of olive brown to reddish brown clay, whereas Unit I in Hole U1565B is mainly composed of brown, grayish brown to dark gray clay. Generally, this unit contains varying amounts of silt, sand, calcareous nannofossils, and planktonic foraminifers, and diatoms are common in the first core section of Hole U1565A. Amphibolite and granite dropstones also are observed in this core. The unit is typically moderately to very well sorted. Smear slide analyses indicate that Unit I consists of abundant undifferentiated clay-sized minerals, rare to trace foraminifers and nannofossils with larger silt- and sand-sized grains comprised of common quartz and undifferentiated feldspar, and rare lithics. Trace amounts of diatoms, zircon, chlorite, and glauconite are also present. Slight to moderate drilling disturbances were observed in parts of the unit. The base of Unit I in Hole U1565B, which lies directly above Unit II, consists of a mixture of sand, subrounded yellow brown clay clasts, and granules to medium pebbles with a poorly sorted grain size. Smear slide analysis of matrix material from this interval indicates abundant undifferentiated clay-sized minerals with rare nannofossils, rare organic debris, and trace diatoms. Silt and sand grains consist of common undifferentiated feldspar, rare quartz, and rare lithics. Dark gray polymetallic concentric nodules were observed at the base of Unit I in Hole U1565A (interval 2R-1, 75–79 cm). Portable X-ray fluorescence (pXRF) data collected from nodules at ~5.80 mbsf (Section 2R-CC) show that their composition consists of low to moderate concentrations of transition metals (10.7 wt% Fe_2O_3, 2.6 wt% Mn_2O_3, 210 ppm Ni, 80 ppm Cu, and 94 ppm Zn). The silica content (~35 wt%) is considered relatively high for such nodules and suggests the presence of clay materials.

The Unit I–II transition was not retrieved in Hole U1565A. Based on the low penetration rates and drilling data, we cored 7.1 m into Unit II in Hole U1565A, recovering more than 3 m of granite. In Hole U1565B, the transition between the two units was recovered in Core 4R, and we cored 3.6 m into the basement, recovering only 10 pebbles and a 10 cm core of highly altered granite conglomerate. Unit II represents one igneous unit consisting of moderately to highly altered medium-grained biotite monzogranite with local, fine-grained mafic and felsic enclaves (Figure

F10G). Throughout Unit II, the monzogranite rocks remain mineralogically and texturally consistent. Observations of two thin sections confirmed the mineralogy and pervasive alteration observed at macroscopic scale. Alkali feldspars are generally partially or totally replaced by undetermined brownish clay minerals and zeolite. Biotite grains show coronae of limonite.

5.1.3.2. Biostratigraphy

Unconsolidated mixed gray and brown sands, silts, and clays with intervals containing gravel and larger clasts, interpreted as ice-rafted detritus, were recovered from Lithostratigraphic Unit I in Holes U1565A and U1565B. Clay- and silt-rich samples from Sections 396-U1565A-1R-CC through 2R-CC and 396-U1565B-1R-CC through 4R-CC were analyzed for microfossil content. All sedimentary samples yield common to trace diatoms, in situ and reworked dinoflagellate cysts, reworked sporomorphs, rare ostracods, common to trace benthic foraminifers, and common planktonic foraminifers. The age diagnostic microfossils indicate an overall Quaternary age. In addition, palynomorphs (mainly dinocysts) indicate reworking from Paleogene and (Lower) Cretaceous strata, and pollen and spores also indicate reworking from Lower Cretaceous rocks. Diatoms and foraminifers are common in the mudline samples and suggest a Middle Pleistocene–Holocene age.

5.1.3.3. Paleomagnetism

Lithostratigraphic Unit I sediments show consistent and continuous variations in inclination and intensity despite drilling disturbance. Some of the locally high values of magnetic inclination (>80°) might be due to drilling-induced magnetization. The sediments have an average intensity of ~3.6×10^{-2} A/m, a magnetic susceptibility (MS; κ) of ~707×10^{-6} [SI], and a low magnetic anisotropy (P') (~1.001). The nonhorizontal magnetic foliation suggests drilling disturbance. In Holes U1565A and U1565B, the geomagnetic polarity is normal, except at 5.58–5.78 mbsf in Hole U1565A, where a magnetic reversal may occur. The sediments have higher magnetic coercivity than the granites. One discrete sample shows limited demagnetization up to a field of 100 mT indicative of a high-coercivity magnetic phase (goethite or hematite) and confirms the normal polarity of this interval.

Granites in Unit II have an average magnetic intensity of 1.17×10^{-2} A/m, likely due to loss of magnetite through alteration, MS of 212×10^{-6} [SI], and low P' (~1.001). Two discrete samples show a normal polarity and the presence of a low-coercivity phase (magnetite, titanomagnetite, or maghemite) consistent with thermal remanent magnetization.

5.1.3.4. Geochemistry

Six IW samples were collected in Hole U1565B. Slight increases in dissolved Cl, Ca, Na, and Si are documented with depth, whereas Mg and Li decrease with depth. Little to no change is observed for K or Sr. Increasing Ca and decreasing Mg could reflect the diagenetic alteration of volcaniclastic material or seawater-basalt interactions. Downcore increases in alkalinity, Mn, NH_4^+, and PO_4^{3-} are paired with decreasing pH and may reflect microbially mediated oxidation of organic matter, although little change is observed for SO_4^{2-}.

Total carbon (TC), total inorganic carbon (TIC), calcium carbonate ($CaCO_3$), total organic carbon (TOC), total nitrogen (TN), and sulfur were determined on six discrete sediment samples. TIC content ranges from 1.25 wt% in the upper section of the cored sediments (0.09–2.91 mbsf) to below 0.01 wt% (average = 0.69 wt%). Assuming TIC is purely representative of $CaCO_3$, values range <0.1 to 10.4 wt%. TC varies between 0.2 and 1.6 wt% (average = 1.2 wt%). TOC is between 0.17 and 0.63 wt% (average = 0.33 wt%) with no clear trend downcore. TOC/TN ratios are between 3 and 25 (average = 9), representative of primarily marine organic matter. In all samples, sulfur is below detection limits.

5.1.3.5. Physical properties

Physical property data acquired at Site U1565 include density, MS, *P*-wave velocity, natural gamma radiation (NGR), color reflectance, X-ray imaging, thermal conductivity, and spectral imaging. Gamma ray attenuation (GRA) bulk density of the sedimentary section varies from 1.4 to 1.79 g/cm^3. Moisture and density (MAD) measurements collected for each section yielded very similar bulk densities (average = 1.69 g/cm^3; n =11), and measured grain densities vary from 2.63 to 2.79 g/cm^3 (average = 2.72 g/cm^3). Porosities range 9%–67%, reflecting the sediment's noncompacted

nature. MS measured on whole rounds and split sections are very similar and range ~34×10^{-5} to 90×10^{-5} [SI]. A MS peak (566×10^{-5} [SI]) in Section 396-U1565A-1R-1 correlates to a dropstone found in the core.

Thermal conductivity measured at 40 cm in Section 396-U1565A-2R-1 yielded an average of 1.42 W/(m·K). NGR for the sedimentary unit varies from 27.7 to 38.1 counts/s (average = 33 counts/s). A MAD sample collected at 61 cm in Section 2R-1 yielded a bulk density of 1.78 g/cm^3, grain density of 2.7 g/cm^3, and porosity of 55%. *P*-wave velocity measured at 60 cm in Section 2R-1 using the Section Half Measurement Gantry (SHMG) resulted in 1530 m/s in the *x*-direction and 1510 m/s in the *z*-direction.

Cores 396-U1565A-3R and 4R penetrated granitic basement (Lithostratigraphic Unit II). The average GRA bulk density of the hard rocks in these core sections is 2.56 cm^3 after the liner correction is applied, which agrees with the three MAD samples collected from these cores. MAD measurements revealed relatively high porosities of ~10% in the granite cubes. MS in the hard rocks is significantly lower than that of the overlying sediments (0 to 22×10^{-5} [SI]).

5.2. Site U1566

A complete section of the feather edge of an SDR sequence below a thin Quaternary sediment unit was recovered at Site U1566. The basalt flows and interbasaltic sediment units were deposited in a subaerial environment and overlie the same weathered granitic basement that was sampled at Site U1566.

5.2.1. Background and objectives

Site U1566 is a companion site to Site U1565. Both sites are located on the western flank of the Kolga High (Figure **F14**) about 1 km apart at a water depth just above 2000 m. The Kolga High is one of several areas along the rifted margin that are characterized by a thin sediment cover on the top basalt surface and a rapidly westward-shoaling Base Cretaceous Unconformity (BCU) (Zastrozhnov et al., 2020).

Interpretation of extensive 3-D seismic reflection data shows that the Kolga High is covered by breakup-related basalts except for two small windows (5 km × 3 km sized) just west of the Kolga High summit (Millett et al., 2022). Characteristic SDR lap onto the Kolga High along its western margin, thinning toward the basalt windows where the lavas have been eroded, making the Kolga High one of the few sites along the Vøring and Møre Margins where the transition from the lowermost extrusive volcanic rocks to the subbasalt strata is accessible by drilling. A previous attempt to determine the nature of this boundary was carried out during ODP Leg 104 in 1985 on the Vøring Marginal High. Hole 642E showed that the SDR represent thick piles of subaerially emplaced basalt flows (Eldholm et al., 1989; Planke, 1994), but unfortunately did not get through the entire lava pile. The Norwegian Petroleum Directorate (NPD) drilled the eastern part of the Kolga High in 2014 (Hole 6403/1-U-1) and recovered 38 m of hyaloclastite with a tholeiitic composition (Bakke, 2017) in the upper part of a lava delta, as defined by eastward prograding reflections, but did not penetrate through the entire extrusive volcanic sequence.

The primary objective of Site U1566 was to sample the lowermost part of the SDR on the Kolga High and, if possible, drill through the entire basalt sequence, but this was not the primary target because the nearby Site U1565 targeted the subbasalt units. By drilling Site U1566, we first aimed to determine the emplacement environment of the initial volcanism on the Kolga High because it provides important constraints on the vertical movement of the margin prior to the onset of extrusive volcanism and extension during the final rifting phase prior to breakup. A second objective at Site U1566 was to constrain the timing of the onset of extrusive volcanism in this area and to provide further insights into the hypothesis that breakup and extrusive volcanism on the Møre Margin predated breakup along the Vøring Margin (e.g., Gernigon et al., 2003). A third objective of Site U1566 was to characterize the magma source of the earliest extrusive basalts and determine whether it was primordial, which would imply rapid ascent through the crust, or it evolved during storage at crustal levels with potential incorporation of continental crustal rocks. A fourth objective was to constrain the rates of magma production both from geochemical analyses and poten-

tially by biostratigraphic dating of interlayered sediments. The final objective of Site U1566 was to gather information on the extent of the basement lithologies drilled at Site U1565 and on lava-subsurface interaction if the bottom of the lava pile could be reached. Although Site U1566 was placed only 1 km away from Site U1565, the seismic data were inconclusive about the dip of the basal surface of the lava pile and hence the depth to this interface.

5.2.2. Operations

Site U1566 consists of a single hole cored to 181.7 mbsf. Coring started at 0525 h on 16 August 2021 and ended at 2230 h on 19 August to accommodate the Versatile Seismic Imager (VSI) logging run in daylight hours on 20 August. A total of 33 cores were taken using the RCB system (Figure **F4**), recovering 100.5 m (55%) of core. Cores 396-U1566A-1R through 3R and 32R–33R were taken with full-length advances. Cores 4R (26.2 mbsf) through 31R (162.3 mbsf) were taken with half-length advances to improve core recovery of the basaltic basement.

All four logging tool strings, the triple combination (triple combo), VSI, Formation MicroScanner (FMS)-sonic tool, and Ultrasonic Borehole Imager (UBI) tool strings, were run to 145 mbsf in the hole. After the wireline logging concluded, the drill string was pulled back to the surface and secured, ending Hole U1566A and Site U1566 at 0230 h on 21 August. The time spent on Hole U1566A was 124 h or 5.2 days.

5.2.3. Principal results

5.2.3.1. Lithostratigraphy

The succession recovered at Site U1566 is divided into three lithostratigraphic units. Unit I (0–19.05 m core depth below seafloor, Method A [CSF-A]) is unconsolidated clay with varying amounts of silt and sand as well as foraminifers. Some of the intervals contain clasts and nodules. Unit II (26.20–148 m CSF-A) is basalt and interbasaltic sediment divided into 14 igneous subunits and 13 sedimentary subunits with a total cored thickness of 121.8 m. Each igneous subunit is composed of one to several discrete lava flows. The dominant facies is aphyric basalt with rare microphenocrysts of plagioclase and characteristically variable vesicularity (Figure **F10**). The chemostratigraphy of the igneous subunits obtained using pXRF shows significant and abrupt variations of the magma composition downhole. Unit III (148–175.4 m CSF-A) is weakly to moderately altered, medium-grained monzogranite with biotite, alternating with decomposed granite and granite-derived sandstones (Figure **F10**).

5.2.3.2. Biostratigraphy

Sedimentary samples analyzed from the first three cores in Hole U1566A yield common to trace diatoms and other biosiliceous debris, trace in situ dinoflagellate cysts, sporomorphs, rare ostracods, common to trace benthic foraminifers, and common planktonic foraminifers. Age diagnostic microfossils indicate an overall Quaternary age for the sedimentary deposits above the uppermost igneous facies.

In addition, a single sample taken from sediments interbedded between igneous rocks in Section 396-U1566A-11R-1 yielded a diverse terrestrial pollen and spore assemblage and a few aquatic elements. Age diagnostic pollen encountered at this level suggest an earliest Eocene age for this sample.

5.2.3.3. Paleomagnetism

Cores 396-U1566A-1R through 3R show normal polarity, followed by reversed polarity from Core 4R to the bottom of the hole, with some data points showing evidence of normal polarity. Lithostratigraphic Unit I has an average initial intensity of natural remanent magnetization (NRM) of 4.3×10^{-2} A/m. The average NRM of Units II and III is ~1.4 A/m, which is two orders of magnitude higher than that of the sediments.

Stepwise demagnetization was conducted on 32 discrete samples from Hole U1566A (thermal demagnetization) with a focus on unaltered basalt flow samples (30 samples). One sediment and one alkali granite sample were also analyzed. The basalt sequence records mostly a reversed magnetic polarity.

5.2.3.4. Geochemistry

Three IW samples were collected from Hole U1566A, including one mudline sample. Alkalinity increases from the mudline (2.3 mM) to the deepest IW sample taken at 18 mbsf (3.1 mM) in Hole U1566A. pH is 7.8 in the mudline and declines to 7.7 at the base of the sediments. PO_4^{3-} content ranges from 4.04 µM at 2.95 mbsf to 2.16 µM at 18 mbsf. NH_4^+ is below detection limit in the mudline but increases to 56.6 mM in the deepest sample.

The hard rock samples (n = 42) recovered from Hole U1566A (Lithostratigraphic Unit II) are mostly subalkaline basalt, with one picrite, and three samples from Unit III plot as granodiorite and granite. Comparison of the data obtained from inductively coupled plasma–atomic emission spectrometry (ICP-AES) with pXRF analysis with basalts from the upper series in ODP Hole 642E (Meyer et al., 2009) and flood basalts from East Greenland (Tegner et al., 1998) indicates an overlap of most samples from Site U1566 with the low-Ti basalts of Greenland (Figure **F11**). Another two samples from Unit III show compositions of high-K granite (Rickwood, 1989), consistent with the high proportion of alkali feldspar, a typical signature of an A-type granitoid (Frost et al., 2001).

TC, TIC, $CaCO_3$, TOC, TN, and sulfur were determined on three discrete sediment samples. TIC content ranges 1.1 wt% at 2.95 mbsf to 0.02 wt% at 18 mbsf. $CaCO_3$ ranges 0.2–11.3 wt%. TOC ranges 0.21–0.03 wt%. All TOC/TN ratios are below 5, indicating marine organic matter. H and sulfur were below detection limits.

5.2.3.5. Physical properties

Physical properties were measured on all whole-round cores, archive and working-half sections, and discrete samples from Hole U1566A. Measurements included GRA bulk density, MS, NGR, *P*-wave velocity, X-ray imaging, MAD and porosity (n = 102) analysis, and thermal conductivity (n = 30).

Lithostratigraphic Unit I cores have *P*-wave velocities of 1489–2909 m/s and whole-round GRA bulk density from 1.51 to 2.10 g/cm^3. Whole-round MS has a mean of 77.7 × 10^{-5} [SI] compared to a mean of 86.9 × 10^{-5} [SI] from discrete half-round measurements. NGR for the sediments varies from 19 to 44 counts/s. The bulk density of discrete samples ranges 1.54–1.82 g/cm^3 (n = 6), and grain densities range 2.74–2.80 g/cm^3.

The ~121 m thick Unit II succession revealed dominantly very low gamma radiation counts (<10 counts/s) in the basalt subunits, whereas the intervolcanic sediment subunits show more variation and values as high as 62.8 counts/s. Discrete samples have bulk densities ranging 1.69–2.84 g/cm^3. Discrete measurements of *P*-wave velocity range 1530–5884 m/s and display systematic variations associated with the varying lithologies. In total, 23 successful thermal conductivity measurements were made across a range of lithologies in Unit II, ranging 1–1.9 W/(m·K). The MS in the sequence (mean = 482 × 10^{-5} [SI]) is significantly higher than that of the overlying soft sediments (mean = 78 × 10^{-5} [SI]).

The granitic basement in Unit III has higher gamma radiation readings (mean = 53.5 counts/s) compared to the overlying volcanic sequence, and discrete bulk densities range 1.97–2.58 g/cm^3. SHMG *P*-wave velocity measurements range 1502–4501 m/s, and thermal conductivity measurements have a mean of 2.1 W/(m·K).

5.2.3.6. Downhole measurements

Wireline data from the four log runs comprise sonic velocities, MS, NGR, bulk density, resistivity measurements, and UBI and FMS image data of the basalt-sediment sequence of Lithostratigraphic Unit II. The lava package displays a consistently low background gamma radiation trend, with three clear peaks in the NGR log linked to siliciclastic sediment interlayers. The MS log reveals clear variations, with higher MS in the basalt flow subunits and almost zero MS in the interbasaltic sediments. The porosity-dependent resistivity, bulk density, photoelectric effect (PEF), and *P*-wave and *S*-wave velocity logs show systematic variations throughout basalt subunits similar to logs collected in other subaerial basalt flow sequences in the province (e.g., Planke, 1994). For instance, the *P*-wave velocity is as low as 2.5 km/s in the interbasaltic sediment subunits and flow tops and increases toward the massive basalt interiors, reaching almost 6 km/s. The

imaging logs (FMS-sonic and UBI) similarly display systematic variations in lava flow facies, with vesicular, low-resistivity flow tops and massive, resistive interiors with probable amygdules.

5.3. Sites U1567 and U1568

Sites U1567 and U1568 comprise a transect of five holes that sample the upper part of the Modgunn hydrothermal vent complex. The vent complex is truncated by an intra-Early Eocene erosional unconformity and is overlain by 20–50 m of Eocene to recent sediments. It consists of a feeder system and a crater at the paleoseafloor. The crater was rapidly infilled during the PETM, presenting an expanded section that consists of diatom-bearing mudstones and ash layers.

5.3.1. Background and objectives

A key objective of Expedition 396 was to constrain the role of breakup volcanism in the PETM. It has long been argued that LIPs may have dramatic impacts on the Earth's environment (e.g., Eldholm and Thomas, 1993; Svensen et al., 2019) and likely caused past mass extinctions (e.g., Ernst and Youbi, 2017). Explosive volcanism influences the climate by the eruption of large volumes of aerosols and ash into the stratosphere, affecting the climate over short time periods of days to years. Long-term climate effects of volcanism are mainly related to emission of sulfur dioxide that causes global cooling and greenhouse gases such as carbon dioxide that cause global warming.

Very large volumes of greenhouse gases must be emitted in short time periods to trigger global warming. One potential mechanism for the eruption of several thousands of gigatons of carbon-bearing gases is the thermal maturation of sedimentary rocks by igneous intrusions offshore mid-Norway (Svensen et al., 2004). The key aspects of this hypothesis are that (1) magma injected as sill intrusions into organic-rich sedimentary rocks generates large volumes of greenhouse gases, namely methane and carbon dioxide, in metamorphic aureoles and (2) pressure buildup due to gas generation causes fracturing of the host rocks, forming hydrothermal vent complexes where the gas and associated solids are transported from the deep sediment basins to the hydrosphere and atmosphere.

Although this process may release the amount of carbon required for the observed climate change, specifically between 2000 and 12000 Gt (Dickens et al., 1995; Dickens, 2011), it is not immediately clear if the bulk of the intrusions were emplaced over the geologically short time span that is required to, for example, explain the observed global warming during the PETM. Also, it is unclear whether the carbon would have been emitted as CO_2 or CH_4.

The hydrothermal systems associated with sill intrusions are manifested as pipe-like seismic anomalies that typically root at the tips of saucer-shaped sill intrusions (Planke et al., 2005). These so-called hydrothermal vent complexes are divided into a lower part (the pipe) and an upper part characterized by crater, eye, or dome-shaped seismic features at the paleoseafloor. The pipes are hundreds of meters long, sometimes up to 6 km. The upper part is typically 1–2 km in diameter but may vary in size from some hundreds of meters to >5 km. Many of the crater-shaped depressions are infilled by stratified seismic units and topped by characteristic mounds above the paleoseafloor. More than 1000 of these hydrothermal vent complexes have been mapped in sedimentary basins along the northeast Atlantic margins (Skogseid and Eldholm, 1989; Planke et al., 2005; Manton, 2015; Reynolds et al., 2017; Kjoberg et al., 2017; Omosanya et al., 2018; Roelofse et al., 2021).

Information on the nature of the pipes exists from cuttings from a single well in the Vøring Basin (6607/12-1; Svensen et al., 2003; Frieling et al., 2016) and from (much older) field analogs, such as in the Karoo Basin in South Africa (Jamtveit et al., 2004; Svensen et al., 2006) and the Tunguska Basin in Siberia (Svensen et al., 2009, 2018). The nature of the mound structures, however, is largely unconstrained. Their interpretation ranges from mud volcano–like sediment deposition to buildup of massive sulfide deposits that are formed at the hydrothermal vent sites by precipitation from hot vent fluids (Berndt et al., 2016).

Sites U1567 and U1568 are located on the Modgunn Arch (Figure **F14**) some 50 km north of the basalt flows sampled at the Kolga High on a dome structure that is interpreted to have formed in the Miocene (Gernigon et al., 2021). The sites were selected because the regional doming uplifted

the vent sites to within reach of IODP drilling. Such shallow burial depths of vent complexes are currently only identified in the Modgunn Arch area in the Vøring Basin and in the Danmarkshavn Basin on the northeast Greenland shelf.

The seismic data clearly show the presence of sill intrusions at shallow depth, ~1 km below seafloor, on the Modgunn Arch. The sills are located in a deformed sedimentary unit with weak reflections that terminate against an angular unconformity (Figure **F5**). A hydrothermal vent complex is interpreted above the upper margin of the sill. The unconformity truncates the dipping reflections in the upper part of the hydrothermal vent complex. At the center of the depression, immediately above the pipe structure, the reflections bend upward, forming a mound. This mound is overlain by draped and onlapping reflections up toward the seafloor.

The aim of Sites U1567 and U1568 was to sample the upper part of the Modgunn hydrothermal vent complex and a nearby reference site along a 500 m long transect to characterize the geology of the vent complex while avoiding the dome-shaped central part of the structure.

The first drilling objective was to constrain the processes that form the seafloor depressions and the infill. At least four potential scenarios are conceivable for this. First, pipe initiation may be explosive due to interaction of sill intrusions with preexisting zones of overpressure that may lead to hydrofracturing of the host rock and rapid ascent of expanding gas. This will result in blowouts that can create craters with similar dimensions as the observed eye structure within days (Thatje et al., 1999; Leifer and Judd, 2015) and infill within a few hundred years. Second, they may be caused by long-term seepage of gas and aqueous fluids liquefying the surface sediments, such as the Lusi mud volcano in Indonesia (Mazzini et al., 2007). Third, they may be caused by repeated mobilization of mud by sills intruding into unconsolidated sediments leading to mud volcanism (e.g., Perez-Garcia et al., 2009) over a time span of thousands of years. Finally, they may result from venting of hydrothermal fluids and precipitation of pyrites and pyrotites over thousands of years (Berndt et al., 2016). Although the first two processes would require a later mobilization of the infill to form the observed domes at the upper termination, for example by gas-controlled seafloor doming (Koch et al., 2015), the domes in the latter two scenarios would be explained by the ejection of vent material.

Each of the four processes would be associated with very different types of material that was ejected during the time that the pipe was formed, both for the solid and the fluid phase. Therefore, understanding the formative processes for the eye structures is intrinsically linked to the second objective: to obtain information on the fluid and gas compositions (i.e., CO_2, CH_4, or higher hydrocarbons) and concentrations and the amount of carbon released because this is crucial for understanding the potential role of hydrothermal venting as a driver of PETM climate change. This includes constraining the rates of fluid venting and its potential to reach far up into the water column or atmosphere depending on how violent the release was, if submarine venting occurred.

The third objective was to characterize the emplacement environment and age of the hydrothermal vent complexes and how it changed in response to venting and rapid warming during the PETM. This characterization includes the changes in microfossil assemblages before, during, and after the PETM. We also set out to determine whether there is evidence for environmental changes in the immediate vicinity of the proposed source of greenhouse gases.

The fourth objective of Sites U1567 and U1568 was to date the prominent unconformity at the Modgunn Arch and the timing of uplift of the eye structure because this constrains the vertical movement of the margin, which is crucial input for melt generation models.

5.3.2. Operations

Operations at Site U1567 revolved around three holes. The first hole reached 195.9 mbsf. Three coring systems were used (Figure **F4**). The APC system was used from the seafloor to 52.9 mbsf. The HLAPC system was deployed for a single core between 52.9 and 54.1 mbsf. After reaching piston coring refusal, the XCB system was deployed for the remainder of the hole. Half-length advances of the XCB system were employed to 69.4 mbsf, and the remainder of the hole was cored using full-length advances. After coring operations ended in Hole U1567A, the hole was prepared

for wireline logging and then successfully logged with the triple combo and FMS-sonic tool strings.

Hole U1567B was offset ~165 m west of Hole U1567A in the direction of Site U1568. It was drilled without recovery to 25 mbsf and then cored with the APC system to 49.3 mbsf, where we experienced a partial stroke of the APC system on Core 396-U1567B-4H. We then switched to the XCB system and continued coring with half-length advances to maximize core recovery. Hole U1567B was terminated at 83 mbsf after retrieving Core 11X. After coring concluded, the drill string was pulled back above the seafloor and secured for transit under dynamic positioning (DP) mode to Site U1568. The bit cleared the seafloor at 1850 h on 23 August 2021, ending Hole U1567B.

The 0.25 nmi move to Site U1568 was completed at 1936 h. With the thrusters already down, the move from Site U1567 to Site U1568 consumed only 45 min of vessel operations. Operations at Site U1568 consisted of two holes. Hole U1568A reached 200.0 mbsf. Two coring systems were used in the coring operations (Figure **F4**). The APC system was used from the seafloor to 51.7 mbsf. The final two cores, 6H and 7H, were both incomplete strokes, and Core 7H advanced only 0.3 m into the formation. The XCB system was employed to advance the hole to the final depth of 200 mbsf. The hole was then prepared for logging, and we successfully conducted two passes each with the triple combo and FMS-sonic tool strings. With operations in Hole U1568A complete, the vessel was offset along the seismic line by approximately 165 m in the direction of Site U1567.

Hole U1568B was washed down to 30 mbsf. The APC system was deployed and advanced to 49.0 mbsf, where we experienced a partial stroke of the APC system on Core 3H. The XCB system was deployed, and coring continued with half-length advances to maximize core recovery to 114.8 mbsf. Hole U1568B was terminated at 124.6 mbsf after retrieving Core 17X with a full-length advance. After coring concluded, the drill string was pulled back above the seafloor and secured for the DP transit back to Site U1567, thus ending Hole U1568B at 1900 h on 26 August. After completing operations at Site U1568 and with the APC/XCB drill string still deployed, the vessel moved in DP mode to reoccupy Site U1567. A total of 71.50 h or 3.0 days elapsed while conducting operations at Site U1568.

A total of 43 cores were recovered at Site U1568 (Figure **F4**). The APC system was deployed nine times over a 70.7 m interval and recovered 72.03 m of core (102%). A total of 34 XCB cores were recovered over a 223.9 m interval. The XCB system recovered 75% of the interval cored or 167.34 m of core. The total interval cored at Site U1568 was 294.6 m; 239.37 m of core was recovered for an overall coring efficiency of 81%.

After completing coring operations at Site U1568, we set the end of the pipe at 1666 meters below rig floor (mbrf) and returned to Site U1567 in DP mode to core an additional hole between Holes U1567A and U1567B with the objective of improving the sampling across the Paleocene/Eocene boundary at this site. Once over the new hole coordinates, we spudded Hole U1567C at 2040 h on 26 August. The precision depth recorder seafloor depth was 1706.1 mbsl. We drilled to 30 mbsf without recovery and then APC/XCB cored to 106.0 mbsf (Cores 1H–14X). Coring operations were completed at 0820 h on 27 August, and the drill string was recovered back on board and secured for the sea passage to Site U1569. A total of 72.25 h or 3.0 days passed while conducting operations at Site U1567. A total of 46 cores were taken at this site. The total interval cored at Site U1567 was 329.9 m with 303.35 m of core recovered (92%).

5.3.3. Principal results

5.3.3.1. Lithostratigraphy

Sites U1567 and U1568 consist of five holes spread along a 500 m transect of infilled sediments associated with cratering in the Modgunn hydrothermal vent complex. The succession recovered at the two sites is divided into six lithostratigraphic units, all of which are identified in each of the five holes and are preliminarily tied based on unit boundaries. Generally, core recovery was high in all the holes, and the depths of most lithostratigraphic unit boundaries are well established. Unit I is gray clay with trace to rare dropstones. Unit II consists of dark brownish gray sediment (clay- to pebble-sized nodules) rich in manganese and iron in the uppermost interval and light yellowish brown sand-rich clay throughout. Unit III is pale yellow to very dark greenish gray clay with silt,

including clasts of clay and rare beds of siltstone. Unit IV is dark greenish gray to very dark gray claystone to siltstone with common volcanic ash beds. Unit V is very dark gray to black parallel laminated claystone with common volcanic ash and lacking bioturbation. Unit VI is very dark greenish gray clay- to siltstone with moderate bioturbation.

5.3.3.2. Biostratigraphy

A thin layer of Quaternary sediments (Lithostratigraphic Unit I) present in all holes in roughly equal thickness (~35 m) was assigned a Quaternary age based on planktonic foraminifer content. No Neogene sediments were identified. Below this, middle Early Eocene (Zone E3) sediments were sampled in Holes U1567A, U1567B, and U1568A. Biostratigraphic and palynological analyses indicated earliest Eocene sediments (Zone E1) were recorded in Hole U1568A, but their presence was not confirmed by biostratigraphic analyses in Holes U1568B and U1567A–U1567C. The PETM succession below is identified based on the presence of the dinocyst marker species *Apectodinium augustum* (Subzone P6b) and supported by diatom marker taxa (Figure **F9**). The extremely expanded PETM deposits sit below the middle Early or earliest Eocene sediments and span between ~20 m in Hole U1567A and a virtually unprecedented 70–80 m in Hole U1568A, given the combined biostratigraphic and lithostratigraphic constraints.

Hole U1567B, and perhaps Hole U1568B, may contain a latest Paleocene sequence (Subzone P6a), but this is not seen in any of the other holes, where the PETM succession rests unconformably on lower Upper to Middle Paleocene sedimentary successions.

5.3.3.3. Paleomagnetism

The sediments at Sites U1567 and U1568 show low magnetic intensity (less than ~10^{-3} A/m) in ~40% of the recovered sections. In some intervals, both the magnetic intensity and the magnetic inclination angle vary greatly (Figure **F13**). The consistent distribution of these intervals with depth and across holes suggests that the low intensity is determined by the detrital source rather than representing a drilling artifact. In such intervals, magnetic polarity cannot be reliably determined. The magnetic inclination data after 20 mT AF demagnetization is typically used to determine magnetic polarity and to place the core sections in a magnetostratigraphic age framework. On the other hand, there are also intervals with moderate to high magnetic intensity (greater than ~10^{-3} A/m). These present both magnetic reversals and magnetic excursions, particularly in Holes U1567A (Core 4H), U1567B (Core 2H), and U1568A (Sections 4H-3 through 5H-3). These reversals, having similar inclination angles in normal and reversed polarity, pass the polarity test and therefore are interpreted as recording the geomagnetic field. The uppermost cores of each hole show a dominantly normal polarity and an inclination close to the calculated geomagnetic dipole field inclination (~77°) for these latitudes. These characteristics suggest that the paleomagnetic data of the youngest sediments accurately capture the geomagnetic field and its periodic reversals.

5.3.3.4. Geochemistry

Almost 100 fluid and sediment samples were collected from the five holes along the transect between Holes U1567A and U1568A. For Hole U1568A, the site closest to the center of the Modgunn vent complex, several elemental profiles of IW diverge from the conservative behavior observed in most of the other holes. The first evidence for this can be seen in the transition between Lithostratigraphic Units I and II (36 mbsf), where some elements decrease significantly across the boundary. These include K (from 12 to 11 mM) and Mg (from >50 to <45 mM). Some of the analyzed elements increase in concentration across this boundary, with the clearest rises observable in the profiles of Ca (from >12 to 13.5 mM), Sr (from 80 to 110 mM), and Li (from 30 to 40 mM). These shifts suggest a complex diagenetic environment, with evidence of marine silicate weathering (e.g., increasing Na and K) but also ash alteration (e.g., rising Ca and decreasing Mg). The elemental data for Unit IV in Hole U1568A corroborate the anomalous values of alkalinity and pH in these strata. Contents of B, Ca, Mg, Si, Sr, and Li are all diminished with respect to overlying and underlying sediments. Mn, Fe, and PO_4^{3-} covary in Hole U1568A, displaying clear enrichments in the uppermost section of the hole and much lower values below 50 mbsf. Increased concentrations of these constituents in the upper sections lend support for microbially mediated oxidation of organic matter.

5.3.3.5. Physical properties

Physical properties were measured for all cores at Sites U1567 and U1568. Lithostratigraphic Unit I consists of up to 35 m thick Quaternary glacial and interglacial deposits with a mean bulk density of 1.81 g/cm^3 and porosities between 47% and 67%. The unit shows a relatively high gamma radioactivity with an across-borehole median of 40 counts/s. *P*-wave velocities measured using the Whole-Round Multisensor Logger (WRMSL) range 1480–2978 m/s (median = 1572 m/s), and SHMG *P*-wave point measurements never exceed 1702 m/s, attesting to the soft and poorly compacted nature of the sediments. Unit II is generally less than 2 m thick and consists of Quaternary clay characterized by a rapid decrease in velocity and density with respect to Unit I. Unit III is characterized by a gradual increase in density (mean = 1.71 g/cm^3) with a corresponding increase in MS that increases most substantially toward the base of the unit, reaching maximum values in all five holes. The peak MS transition associated with the Unit III/IV boundary generally decreases laterally from Hole U1568A (maximum = 1772 × 10^{-5} [SI]; mean = 451.3 × 10^{-5} [SI]) to Hole U1567A (maximum = 740.5 × 10^{-5} [SI]; mean = 225.3 × 10^{-5} [SI]). The highest MS above this horizon (>1700 × 10^{-5} [SI], as measured by the Section Half Multisensor Logger [SHMSL]) occur in the two holes most proximal to the center of the vent complex (U1568A and U1568B). We suggest that the basal high MS layer (with values greater than 1700 × 10^{-5} [SI]) in the two proximal boreholes may pinch out prior to reaching the three more distal Site U1567 boreholes, where values ~700–800 × 10^{-5} [SI] are recorded.

The recovered thickness of Unit IV varies from ~6 m in Hole U1567A to more than 65 m in Hole U1568A. The recorded *P*-wave velocity (mean = 1922 m/s; median = 1903 m/s) is the highest amongst all units, associated with a relatively high mean bulk density of 1.74 g/cm^3 and a relatively low MS of 90 × 10^{-5} [SI]. The general trend of decreasing MS with depth appears to be linked to a reduction of ash layers with depth in Unit IV. Units V and VI reveal generally low and consistent *P*-wave velocities of around 1600 m/s with accompanying low bulk densities with means of 1.43 and 1.42 g/cm^3, respectively. In summary, the cored sequences revealed physical properties that are consistent with a very weakly compacted mudstone-dominated sequence with fine-scale internal physical property variations linked to ash deposition.

5.3.3.6. Downhole measurements

Logging data were collected over a total open hole interval of ~112 m in Hole U1567A and ~105 m in U1568A, yielding high-quality data from both the modified triple combo and FMS-sonic tool strings. Four logging units for Hole U1567A and three for Hole U1568A were defined, and they broadly correspond to the lithostratigraphic units. Velocities and densities are low with few exceptions in the reference hole (U1567A) around 1.55 km/s and 1.45 g/cm^3, respectively. However, a well-defined NGR peak of 65 gAPI is clearly visible. The proximal vent hole (U1568A) shows a wider variation in seismic and NGR properties, with a velocity range of 1.5–2.7 km/s, densities from 1.55 to 1.9 g/cm^3, and NGR from 30 to 40 gAPI. FMS image log data from both holes display fine-scale sedimentary structures and stratification.

5.4. Sites U1569 and U1570

Sites U1569 and U1570 were drilled as a transect of five holes on the Mimir High, which is part of the Vøring Transform Margin. We recovered an expanded section of Paleocene and Eocene sediments, including a thick interval of PETM deposits, in three holes. The cores will allow us to constrain the climatic and environmental changes at high resolution and provide constraints on the biogeochemical changes influenced by hydrothermal venting. The expanded sedimentary sections show that the Vøring Transform Margin was a depocenter during Paleocene rifting and into the Early Eocene until the marginal high formed during passage of the Aegir Ridge some 5 My after breakup.

5.4.1. Background and objectives

Site U1569 and the ribbon of four boreholes that comprise Site U1570 are located on the Mimir High at a 2171–2270 m water depth. The Mimir High is a transform margin high on the Vøring Transform Margin (Figure **F14**). Such highs are characteristic structural elements of transform margins worldwide, such as offshore Ghana/Côte d'Ivoire, western Australia, and the Falklands (Basile and Allemand, 2002; Mercier de Lépinay et al., 2016; Baby et al., 2018; Lorenzo and Wessel,

1997). Transform margins are characterized by very narrow COBs and late uplift of the continental crust when the adjacent spreading center passes. Several processes are involved in the formation of the highs. They include lateral heat transport and associated thermal uplift as well as erosion-enhanced uplift (Vågnes, 1997; Basile and Allemand, 2002).

The Vøring Transform Margin is characterized by diminished breakup-related extrusive volcanism compared to the juxtaposed rifted margin segments of the Vøring and Møre Margins (Berndt et al., 2001a). Nevertheless, thin extrusive basalts, intrusions, and a high-velocity, lower crustal body have been documented for the Vøring Transform Margin (Gernigon et al., 2021; Mjelde et al., 2009). The reduced magmatic crustal thickening may be the result of cooling of the Norway Basin lithosphere by the continental Vøring Plateau lithosphere during initial seafloor spreading, lowering the ambient mantle temperature and resulting in reduced melt generation (Berndt et al., 2001b). As a result, the basalt cover on the Vøring Transform Margin is generally thin, and even absent, on the Mimir High (Figure **F14**). However, an erosional truncation at the top of the high does not preclude that some basalt may have been eroded.

The absence of basalt cover makes the Mimir High an exceptional place to study the stratigraphy at intervals coeval to and below the Paleogene basalt. These formations are not well known from drilling; the closest boreholes, 6504/5-15 and 6603/5-16, are more than 100 km away. However, the strata are subcropping along a kilometer-high escarpment on the southwest flank of the Mimir High. This escarpment was sampled during two cruises conducted in 2000 and 2013 using gravity corers, dredges, and an ROV (Polteau et al., 2020). The cruises documented the presence of Upper Cretaceous to Lower Eocene successions that include outcropping doleritic sills with columnar jointing. Although the recovered late Campanian and early Maastrichtian sediments were deposited in a coastal to shallow marine setting, the Paleocene samples indicate deep marine conditions with abrupt shoaling and formation of the Mimir High in the Early Eocene. Toward the Vøring Basin, seismic data clearly show several large sill intrusions that affected this part of the margin and indicate that the strata generally dips from the Mimir High to the northeast (Figure **F6**).

The first objective of Sites U1569 and U1570 was to constrain the paleoenvironmental conditions during the Paleocene–Eocene transition. In particular, we hoped to obtain high-resolution information about the timing, duration, and nature of the environmental changes due to rapid warming and subsequent cooling during the earliest Eocene. The second objective of Sites U1569 and U1570 was to tie the borehole stratigraphy with reflection seismic data to constrain the vertical movements of this margin segment as an input for geodynamic melt production models. In particular, the timing of uplift and any further constraints on the amount of crustal stretching are important. The third objective of Sites U1569 and U1570 was to characterize the Paleogene sediments and their potential for releasing hydrocarbons when intruded by sills. Here, the key parameter is the amount of TOC in the sediments that may be transformed to greenhouse gases by contact metamorphism.

In the case that any igneous rocks were sampled, a further objective was to constrain the melting and emplacement conditions. This includes the composition of the magma and in particular the temperatures at which melting took place.

5.4.2. Operations

The original plan for Site U1569 called for dual coring of key stratigraphic intervals, including a hole to 300 mbsf to be cored using the APC/XCB system and a second hole to 800 mbsf to be cored using the RCB system (Figure **F4**). In the case we could not properly sample the complete stratigraphic target at Site U1569, four offset holes of 200 m each were proposed along a transect of outcropping strata extending west of Site U1569, where deep stratigraphic targets were present at shallower subseafloor depths, as an alternative drilling strategy.

Hole U1569A was cored to the shortened depth of 404.6 mbsf after coring through the PETM, our scientific target, and penetrating 50 m into the Upper Paleocene. Estimating that the base of the Paleocene could be much deeper and to improve core recovery of the Paleocene/Eocene boundary, we ended coring in Hole U1569A in favor of sampling the older strata at much shallower

depths at alternate ribbon Site U1570. Coring the PETM strata at a shallower location also allowed us to sample less mature PETM sediments with better microfossil preservation.

After coring ended in Hole U1569A, we conditioned the hole and released the RCB bit at the bottom of Hole U1569A in preparation for wireline logging. A total of 44 RCB cores were retrieved from the site, five of which were half-length advances. The RCB system was used to core 404.6 m, and 144.91 m of core was recovered (36%). The hole was then displaced with 125 bbl of 10.5 lb/gal mud, and the end of the pipe was set at 84.0 mbsf. The triple combo tool string was rigged up and deployed. The initial logging run failed to pass a bridge at 127.4 mbsf. With very little open hole to log, the tools were pulled back to the surface and logging operations were terminated. After logging concluded, the drill string was pulled back to the surface. The remaining top half of the mechanical bit release (MBR) cleared the rotary table at 2220 h, ending Hole U1569A and Site U1569. A total of 74.25 h or 3.1 days were recorded while on Site U1569.

The coring plan at Site U1570 was the same for all four holes (Figure **F4**): to core to 200 mbsf and sample the Paleocene/Eocene boundary interval at considerably shallower depths than at Site U1569. Three of the four holes were completed to 200 mbsf, and the fourth one was terminated at 163.6 mbsf after we determined that the science objective for the hole had been met. All four holes were cored with the RCB system with a combination of half-length (4.6 m) and full-length (9.6 m) advances. The half-length advances were used to maximize core recovery in zones of interest at the expense of the additional wireline time. Coring in the final hole, U1570D, was ended after reaching the Environmental Protection and Safety Panel approved depth of 200 mbsf. After conditioning Hole U1570D for wireline logging, the RCB bit was released at the bottom of the hole and the end of pipe was set at 76.0 mbsf. The triple combo and FMS-sonic tool strings were successfully deployed to the full depth of the hole. After logging concluded, the drill string was pulled back to the surface. The bottom-hole assembly (BHA) was racked back in the derrick, and the outer core barrel was disassembled and inspected. The rig floor was secured at 2348 h, and the bridge was notified that operations were complete at Site U1570. A total of 112 RCB cores were taken at the site. The RCB system was used to core 763.6 m, and 270.09 m of core was recovered (35.4%). A total of 147.50 h or 6.2 days were recorded while on Site U1570.

5.4.3. Principal results

5.4.3.1. Lithostratigraphy

Sites U1569 and U1570 consist of five holes on the northeastern flank of the Mimir High. The holes sampled northeast dipping stratigraphy along a 5 km transect where Paleogene age seismic reflections truncate below thin Quaternary sediments at ribbon Site U1570. The succession recovered at the two sites is divided into ten lithostratigraphic units. As expected from the seismic interpretation of the high-resolution 3-D seismic data, none of the five holes include all ten units. Unit boundaries are identified based on lithologic change and supported by physical properties and biostratigraphy. Where recovery is high, boundaries between units are well established. Where core recovery is low, unit boundaries are placed at the top of the underlying unit.

Lithostratigraphic Unit I is grayish brown and brown unconsolidated mud. Unit II consists of dark greenish gray consolidated mud that is locally slightly bioturbated. Unit III is grayish brown sand rich clay with nodules. Unit IV is very dark gray mudstone. Unit V is divided into two subunits. Subunit Va is very dark gray mudstone with sparse parallel lamination and slight localized bioturbation along with rare limestone intervals and common ash beds. Subunit Vb is very dark gray mudstone with sparse parallel lamination and slight localized bioturbation along with common ash beds and diagenetic pyrite. Unit VI is hypohyaline garnet dacite with cordierite, pyrite, and graphite. Unit VII is dark gray ash-rich mudstone with parallel lamination and common pyrite. Unit VIII is dark greenish gray to dark gray bioturbated mudstone. Unit IX is light gray limestone. Unit X is very dark greenish gray bioturbated mudstone with common ash along with some beds of limestone and volcaniclastic conglomerate.

5.4.3.2. Biostratigraphy

Quaternary sediments from Holes U1569A and U1570A–U1570D (~10–80 m thick) are characterized by glacially influenced hemipelagic mud, which unconformably overlies Lower to Middle Miocene strata followed by uppermost Oligocene strata that unconformably overlies upper Lower

Eocene strata. Another stratigraphic break separates the upper Lower Eocene strata from the thick (>100 m) lower Lower Eocene deposits, and much of the Lower Eocene is apparently missing. The lower Lower Eocene deposits include a PETM succession that is at least 10–40 m thick. The sequences spanning the Paleocene/Eocene boundary do not show any record of the presence of uppermost Paleocene sediments. Dinocyst chronobiostratigraphy suggests that at least ~1 My of the latest Paleocene is missing. The oldest sediments recovered are assigned to the Middle Paleocene (Selandian; 61.6–59.2 Ma), recorded in samples from Holes U1569A and U1570C.

5.4.3.3. Paleomagnetism

For the post-PETM strata (Lithostratigraphic Units I–VI), the average intensity of magnetization varies from 2.26×10^{-2} to 3.22×10^{-2} A/m. The median coercivity varies from 1.06 to 2.17, indicating the magnetic mineralogy is dominated by diagenetic hematite or goethite. There are six conspicuous episodes of magnetic reversals marked by magnetic inclinations <0° (Figure **F13**). The bulk MS of one discrete sample (396-U1569A-23R, 28–30 cm) is over 1×10^{-3} [SI], indicating a small ferromagnetic contribution, possibly from magnetite. This is also the only discrete sample presenting subhorizontal magnetic fabrics. The rest of the samples are paramagnetic, with a bulk MS below 1×10^{-3} [SI], and have oblique magnetic fabrics, which may be owed to drilling-related disturbances. A low corrected degree of anisotropy ($P' < 1.028$) indicates the absence of micaceous minerals.

The average intensity of magnetization of PETM strata (Unit VIII) is lower than the post-PETM strata (0.06×10^{-2} to 0.13×10^{-2} A/m). However, the median coercivity is higher (1.32–3.04), indicating higher hematite or goethite proportions. At least two short-lived episodes of normal polarity truncated the dominantly reversed magnetic polarity. All four discrete samples present oblique magnetic fabrics, low bulk MS ($\kappa m \leq 0.4 \times 10^{-3}$ [SI]) and low corrected degree of anisotropy ($P' \leq 1.018$). Pre-PETM strata (Units VIII–X) have the highest coercivity compared to the post-PETM and PETM units. High coercivity may be due to higher proportions of hematite and goethite. Their intensity of magnetization (0.06×10^{-2} to 0.59×10^{-2} A/m) is lower than post-PETM strata but similar to PETM strata. All discrete samples have low bulk MS ($\kappa \leq 0.5 \times 10^{-3}$ [SI]) and a low corrected degree of magnetic anisotropy ($P' \leq 1.077$). Only two discrete samples (396-U1570B-21R, 56–58 cm, and 25R, 92–94 cm) present subhorizontal magnetic fabrics. The rest have oblique fabrics, possibly due to drilling-related disturbances.

5.4.3.4. Geochemistry

A total of 32 IW samples were collected from Hole U1569A, and 57 samples were collected from three holes at Site U1570. Geochemical data from these sites show substantial variability both downcore and between holes. In Hole U1569A, nonconservative behavior is observed for a range of measured IW variables, with periods of high pH and low alkalinity similar to those observed at Sites U1567 and U1568. This is also similar to the profiles observed in Hole U1570C and suggests that lithologic changes control the IW composition. In Holes U1570A and U1570B, however, elemental distributions appear to be primarily conservative, and they suggest diffusion and advection are the primary controls on IW composition, potentially linked to the extensive fracturing of these rocks. In all holes, carbonate content is high in the upper units before dropping to lower values farther downcore. Occasional peaks in carbonate and organic carbon content suggest infrequent authigenic mineral precipitation. Three hard rock samples from Lithostratigraphic Unit IV in Hole U1570D appear to be of dacitic composition. X-ray diffraction (XRD) analysis indicates the primary sedimentary components are quartz, calcite, and a range of clays. In some samples, it was possible to identify clinoptilite as the primary clay mineral, a form of zeolite linked to ash weathering. The direct impact of volcanic ash deposition is present in the form of a range of pyroxene minerals.

5.4.3.5. Physical properties

A total of 151 samples across the five holes were measured for MAD, and 1344 *P*-wave velocity measurements were made on discrete samples to constrain and supplement physical property measurements conducted on the WRMSL and SHMSL. The results showed distinct petrophysical properties for the 10 lithostratigraphic units described at the sites. Similarly to Sites U1567 and U1568, peaks in MS are related to the presence of ash beds, such as in Lithostratigraphic Subunit Va. However, the magnetic signature of ash beds dissipates in Subunit Vb, and this characteristic is

interpreted as evidence of increased alteration of the ashes. The dacitic Unit VI (Holes U1570A and U1570D) has noticeably higher seismic velocity, relatively high density, and low MS compared to surrounding sediments. However, the highest *P*-wave velocity of all five holes is recorded in Unit IX (mean = 4172.6 m/s), which represents the thin limestone bed found in Hole U1570B. This unit also has high density (GRA bulk density mean = 2.31 g/cm^3) and the lowest porosity (MAD porosity = 19%) values.

5.4.3.6. Downhole measurements

Wireline logging was conducted in Holes U1569A and U1570D, which extended to 404.6 and 200 m drilling depth below seafloor (DSF), respectively. Two wireline logging tool strings, the triple combo and the FMS-sonic, were planned for Hole U1569A; however, an obstruction encountered at 127.4 m wireline log depth below seafloor (WSF) during the first deployment of the triple combo prevented us from completing the logging plan. Two logging runs were performed successfully in Hole U1570D with the triple combo and the FMS-sonic tool strings over a total open hole logged interval of ~117 m.

Six logging units were defined in Hole U1570D, constrained by a combination of the lithostratigraphy, physical properties, and wireline data. In the main open hole logged interval of Hole U1570D, the wireline properties reveal several transitions that correspond closely to the lithostratigraphic units.

The open hole part of Logging Unit 2 reveals gamma radiation of ~45–50 gAPI, low bulk density of ~1.6–1.7 g/cm^3, and low consistent V_P of around ~1.65 km/s. Logging Unit 3 exhibits relatively high V_P (~1.8–2.3 km/s) and resistivity compared to its surrounding claystone-dominated sequence and corresponds closely to Lithostratigraphic Unit VI. Logging Unit 4 is characterized by relatively high gamma radiation that fluctuates between ~45 and 85 gAPI. Logging Unit 5 comprises a thin ~3 m thick interval with elevated density (~1.95 g/cm^3) and V_P (2 km/s) and extreme PEF enrichment up to ~33 b/e$^-$ coupled with a gamma radiation reduction. The remainder of the logged section is assigned to Logging Unit 6 and shows minor fluctuations in gamma radiation, density, and PEF.

5.5. Sites U1571 and U1572

Sites U1571 and U1572 sampled the upper portions of the Inner SDR on the central part of the Vøring Margin. At both sites, two holes were drilled, the first using the RCB system to sample the basaltic basement and the second one using the APC system to sample the overlying sediment package. The reason for drilling two sites only 5 km apart was the starkly different seismic characters of the top basalt surfaces at each site, which are interpreted to be the boundary between different emplacement environments where the upper sequence was emplaced into a wet environment (Planke et al., 2017). The sediments directly overlying igneous facies are of latest Early Eocene age, which could be consistent with relatively late emplacement of the last flood basalts on the Vøring Marginal High; however, it is equally possible that the overlying sediments were not deposited immediately after the lava flows.

5.5.1. Background and objectives

Sites U1571 and U1572 are located on the Skoll High on the Vøring Marginal High, about 15 km west of the Vøring Escarpment (Figure **F15**). The western part of the Vøring Marginal High is characterized by SDR sequences, first noted by Hinz and Weber (1976), that are interpreted as ≤6 km thick volcanic complexes near the COB (Skogseid and Eldholm, 1987, 1989). The first sampling of basalts on the Vøring Marginal High was DSDP Leg 38 (Talwani, Udintsev, et al., 1976). Holes 338 and 342 were drilled into igneous basement, and 11 and 12 m of basalt were recovered, respectively. Subsequently, a 1277 m deep borehole was drilled into the upper margin of the SDR during ODP Leg 104 (Eldholm et al., 1987). Hole 642E yielded more than 900 m of basalt and penetrated at least 135 lava flows and 3 dikes. The flows were interlayered with 59 volcaniclastic sedimentary units that mainly represent weathered basalt flow tops and one ignimbrite. Based on their geochemical and petrological composition, the volcanic succession was divided into an upper 800 m thick tholeiite series and a lower series that is at least 100 m thick and consists of dominantly basaltic andesite flows (Eldholm et al., 1987; Abdelmalak et al., 2016).

The extent and thickness of the breakup-related basaltic complex has subsequently been mapped along the mid-Norwegian continental margin using seismic volcanostratigraphy and igneous seismic geomorphology (Berndt et al., 2001b; Planke et al., 2000, 2017; Millett et al., 2022). The seismic reflection data reveal substantial differences in the volcanic emplacement environments across the Vøring Marginal High in time and space. Planke et al. (2017) documented distinct differences in the physical volcanology across the marginal high based on the igneous seismic geomorphology of the top basalt surface. The eastern parts of the margin are characterized by a lava flow field that suggests that lava was flowing from eruption centers in the west toward the paleocoastline in the east where they form a lava delta (Abdelmalak et al., 2016b). Incised valleys on the top basalt surface further suggest erosion by rivers flowing from west to east. The top basalt surface farther west is characterized by a rough morphology with numerous semicircular anomalies that have been interpreted as rootless cones due to lava flowing across a wet substrate leading to phreatomagmatic and phreatic eruptions. This pitted surface belongs to a seismic sequence that onlaps onto the eastern flow field and must be younger than the subaerial basalts drilled in Hole 642E (Figure **F7A**). Strikingly, the two domains also exhibit very different structural deformation. There are few normal faults with minimal displacement of the pitted surface; in contrast, the eastern subaerial lava flows are offset by numerous north–south trending normal faults with displacements of tens of meters.

Site U1571 is located on the eastern faulted lava flow field, whereas Site U1572 is located on the pitted surface farther west. The morphological difference between the two sites and the onlap relationship suggest that the lavas have been emplaced diachronously, possibly in different environments. The first objective of these sites was to obtain information on the emplacement environment based on the facies of the recovered basalt and sediments. This information will con-

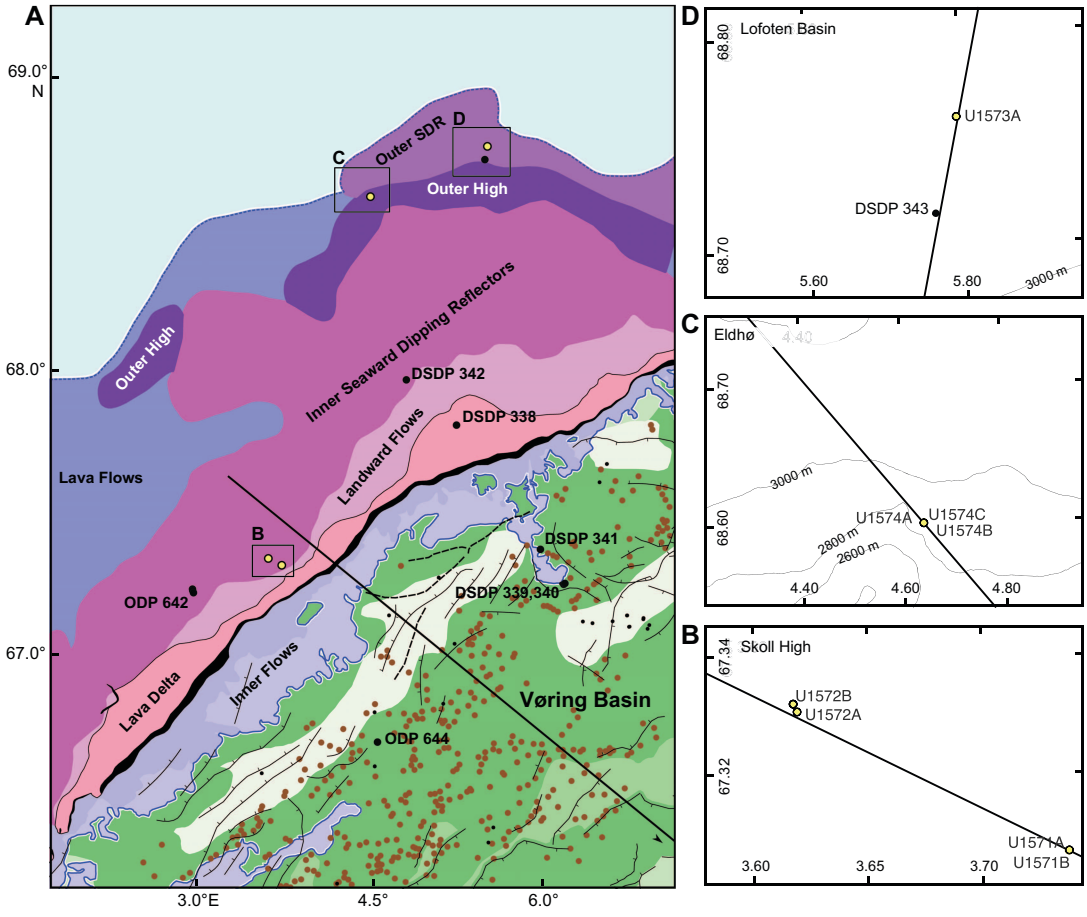

Figure F15. A. Tectonic and magmatic elements of the Vøring Basin. Legend in Figure F3. Brown dots = hydrothermal vent complexes. B. Skoll High (see Figures F2 and F3 in the U1571 and U1572 chapter [Planke et al., 2023f]). C. Eldhø (see Figure F1 in the U1574 chapter [Planke et al., 2023c]. D. Lofoten Basin (see Figure F1 in the U1573 chapter [Planke et al., 2023b].

strain the vertical movements of the margin, such as whether both facies were indeed emplaced in a subaerial environment or whether there is a difference between the relatively well-constrained subaerial flows in the east and the possibly shallow marine flows in the west. The second objective was to establish the time of emplacement of the two sequences to constrain the temporal evolution of the breakup volcanism. The third objective was closely linked to the first two; by analyzing the emplacement environment, we hoped to obtain information on the environmental and, by proxy, the climatic changes during and shortly after the main phase of volcanism. This will primarily be based on biostratigraphic and geochemical analysis of the sedimentary succession immediately above the top of the basalt and possibly the sedimentary layers between basalt flows. The fourth objective was to constrain the conditions in the melt region, specifically the composition of the mantle before melting and the ambient temperature from the geochemistry and petrology of the encountered rocks. Reaching this objective will help to parameterize geodynamic models that will distinguish between the relative importance of the drivers of excess volcanism.

Furthermore, Sites U1571 and U1572 will address two auxiliary objectives laid out in the *Scientific Prospectus*. First, we hope to provide information on the suitability of the breakup basalt sequences and interbedded sediments for permanent geological storage of CO_2. This will require obtaining information on their porosity and permeability as well as their geochemical composition, in particular the abundance of olivine, which may react with CO_2. Second, we hope to obtain information on the earliest incursion of deep water into the North Atlantic and the extent of major freshwater incursions into the young ocean (e.g., during the *Azolla* event) (Brinkhuis et al., 2006).

Finally, and akin to the other sites, we will use the drilling results to test and calibrate the volcanological predictions of seismic volcanostratigraphy and igneous seismic geomorphology for the Landward Flows and SDR and smaller scale volcanic elements identified in the seismic reflection data.

5.5.2. Operations

Site U1571 consists of two holes. Hole U1571A was cored using the RCB system to 247.6 mbsf and then logged with the triple combo, FMS-sonic, and UBI logging tool strings. Although the original plan called for a single hole to 240 mbsf, the poor recovery through a critical stratigraphic interval suggested an additional hole should be cored at the site. The APC/XCB system was selected for the second hole. Hole U1571B was cored with the APC system to refusal at 57.2 mbsf. The XCB coring system was deployed and cored with good results through 143.7 mbsf. Polycrystalline diamond compact (PDC) XCB cutting shoes were used to core through the hard layers between 125 and 143.7 mbsf. Coring in Hole U1571B was terminated at 1005 h on 11 September 2021. The drill string was pulled back to the surface after clearing the seafloor at 1110 h. On clearing the seafloor, the vessel began moving in DP mode to the next site, which is located 3.1 nmi away. The APC/XCB coring bit cleared the rotary table at 1351 h, ending Hole U1571B and Site U1571. A total of 124 h or 5.2 days were recorded while on Site U1571.

A total of 59 cores were taken at Site U1571. The RCB system was used for Hole U1571A and cored 247.6 m and recovered 116.55 m of core (47.1%). Hole U1571B used both the APC system and the XCB system. Seven APC cores were taken over a 57.2 m interval. Recovery was 58.73 m (102.7%). The XCB system was used for 13 cores over a 86.5 m interval and recovered 62.2% of the cored interval.

Site U1572 also consists of two holes. Hole U1572A was cored using the RCB system to 330.5 mbsf and then logged with the triple combo tool string. Further logging was canceled because of degrading hole conditions. The original plan called for a single hole to 320 mbsf. Poor recovery through a critical zone suggested an additional hole should be cored at the site. The APC/XCB coring system was selected for the second hole at the site. Hole U1572B was cored with the APC and HLAPC systems to APC refusal at 209.6 mbsf. The XCB system was deployed, and the basement contact interval was cored to 224.3 mbsf. PDC XCB cutting shoes were used to core through the hard layers between 209.6 and 224.3 mbsf. Coring in Hole U1572B was terminated at 1045 h on 16 September. The drill string was pulled back to the surface after clearing the seafloor at 1235 h. On clearing the rotary table, the APC/XCB BHA was secured at 1612 h, ending Hole U1572B. The bridge was notified that the drill floor activities were complete. The thrusters and hydro-

phones were pulled back inside the hull of the vessel, and the vessel began the sea passage to Site U1573. A total of 122.5 h or 5.1 days were recorded while on Site U1572.

A total of 79 cores were recorded at Site U1572. The RCB system was used for Hole U1572A to core 330.5 m and recover 139.53 m of core (42.2%). Hole U1572B used the APC, HLAPC, and XCB systems. There were 16 APC cores recorded over a 149.3 m interval. Recovery was 154.45 m (103.5%). The HLAPC system was used for 13 cores over a 60.3 m interval (recovery = 99.1%). The XCB system was used for 4 cores over a 14.7 m interval (recovery = 28.3%).

5.5.3. Principal results

5.5.3.1. Lithostratigraphy

The succession recovered from the four holes cored at Sites U1571 and U1572 is divided into eight lithostratigraphic units. Units I–VI are sedimentary, Unit VII is igneous, and Unit VIII is characterized by primarily igneous rock interbedded with sediment and volcaniclastics.

Units were determined based on macroscopic observations and microscopic analysis and are supported by physical properties and biostratigraphy. Hole U1572A is the only hole that includes all eight units. APC drilling was utilized in Holes U1572B and U1571B, where recovery of sediments is more than 100% in many sediment cores. Unit I is grayish brown and brown unconsolidated mud. Unit II is greenish gray consolidated mud and nannofossil ooze. Unit III is greenish gray mud, very dark gray diatomite, and diatom ooze. Unit IV consists of greenish gray radiolarian ooze interbedded with gray to black ash. Unit V is very dark gray mudstone with parallel lamination and dark gray ash. Unit VI is biosiliceous ooze with mudstone and common ash. Unit VII is basaltic andesite and basalt lava flows. Unit VIII consists of basalt and interbasalt sediments and is divided into two distinct subunits. Subunit VIIIa is composed of hyaloclastite alternating with volcanic mudstone. Subunit VIIIb is an alternation of basaltic lava flows and minor mudstone. The presence of Unit VII as the top basement unit at Site U1572 constitutes the main difference between the two sites and likely is the reason for the difference in seismic character.

5.5.3.2. Biostratigraphy

The Quaternary sediments recovered from the holes at Sites U1571 and U1572 (maximum = ~80 m) are characterized by glacially influenced hemipelagic muds, which typically unconformably overlie Miocene strata. Siliceous and organic-walled microfossils were found in various abundances below the Quaternary deposits. Also, indications are that the successions at Sites U1571 and U1572 are very similar; Lower to late Middle Miocene strata overlie upper Lower to Upper Eocene strata, with some Lower Oligocene sediments, especially in Hole U1572B.

In Holes U1571B, U1572A, and U1572B, sediments recovered from directly above the igneous basement yield *Azolla* spp. and associated dinocyst marker species. The well-documented Nordic Sea *Azolla* phase has been dated as occurring between ~49 and 48 Ma (mid-Chron C22n to mid-Chron C21r) at the end of the Early Eocene (Ypresian) (e.g., Brinkhuis et al., 2006; Barke et al., 2011). This constrains the earliest sediment accumulation to the very end of, or directly postdating, the EECO as defined by Westerhold et al. (2018). The Middle to Late Eocene appears to be marked by a progressive deepening or increasing distance to shore. Because of the general absence of microfossils, no biostratigraphic age constraints are available from between the igneous units.

The microfossil-rich sedimentary succession in Hole U1572B was utilized to construct an integrated age-depth model, and the correlation to the shipboard paleomagnetic reversal interpretation and lithostratigraphic units is shown in Figures **F16** and **F17** and Table **T5**.

5.5.3.3. Paleomagnetism

The low recovery in Holes U1571A and U1572A prevents the construction of a meaningful magnetostratigraphic record; however, better magnetostratigraphic results were obtained from Holes U1571B and U1572B. Lithostratigraphic Unit I shows mainly normal polarities in the uppermost 40 m, although the increase of the I_{20mT}/NRM ratio with depth suggests a possible climatic change. The upper and lowermost parts of Unit II show normal polarity with a reversed polarity in the lower part. Unit III has the lowest magnetic intensities ($I_{NRM} < 10^{-4}$ A/m) for these sites. The dominantly normal polarities might be caused by drilling-induced magnetization. Unit IV shows

evenly normal and reversed polarities. Unit V has exclusively normal polarities that are validated by discrete samples. Unit VI shows a mixture of normal and reversed polarities. The basaltic sequences show strong magnetization intensities with dominantly reversed polarities, all validated by discrete samples. The magnetic carrier in these basalts has a low coercivity and may potentially carry a viscous remanent magnetization that could be used for core reorientation. The anisotropy of MS (AMS) of sediments shows that correction of magnetic inclination for inclination shallowing will not be necessary (Figure **F13**). The basalts carry a strong AMS resulting from viscous flow.

5.5.3.4. Geochemistry

The recovered basalt sequence from the Skoll High shows chemical and spatial variations between Sites U1571 and U1572. For example, TiO_2 concentrations indicate the presence of occasional high-Ti basalts, usually associated with LIPs and overlap with high-Ti basalts from East Greenland and flows found during previous drilling in Hole 642E during ODP Leg 104 (Figure **F11**). The compositions of the uppermost basalts at the two sites appear to be representative of two different flow units. This supports the lithostratigraphic interpretation of an additional unit (Lithostratigraphic Unit VII) at the top of the Unit VIII basalts at Site U1572. IW recovered from interbasalt

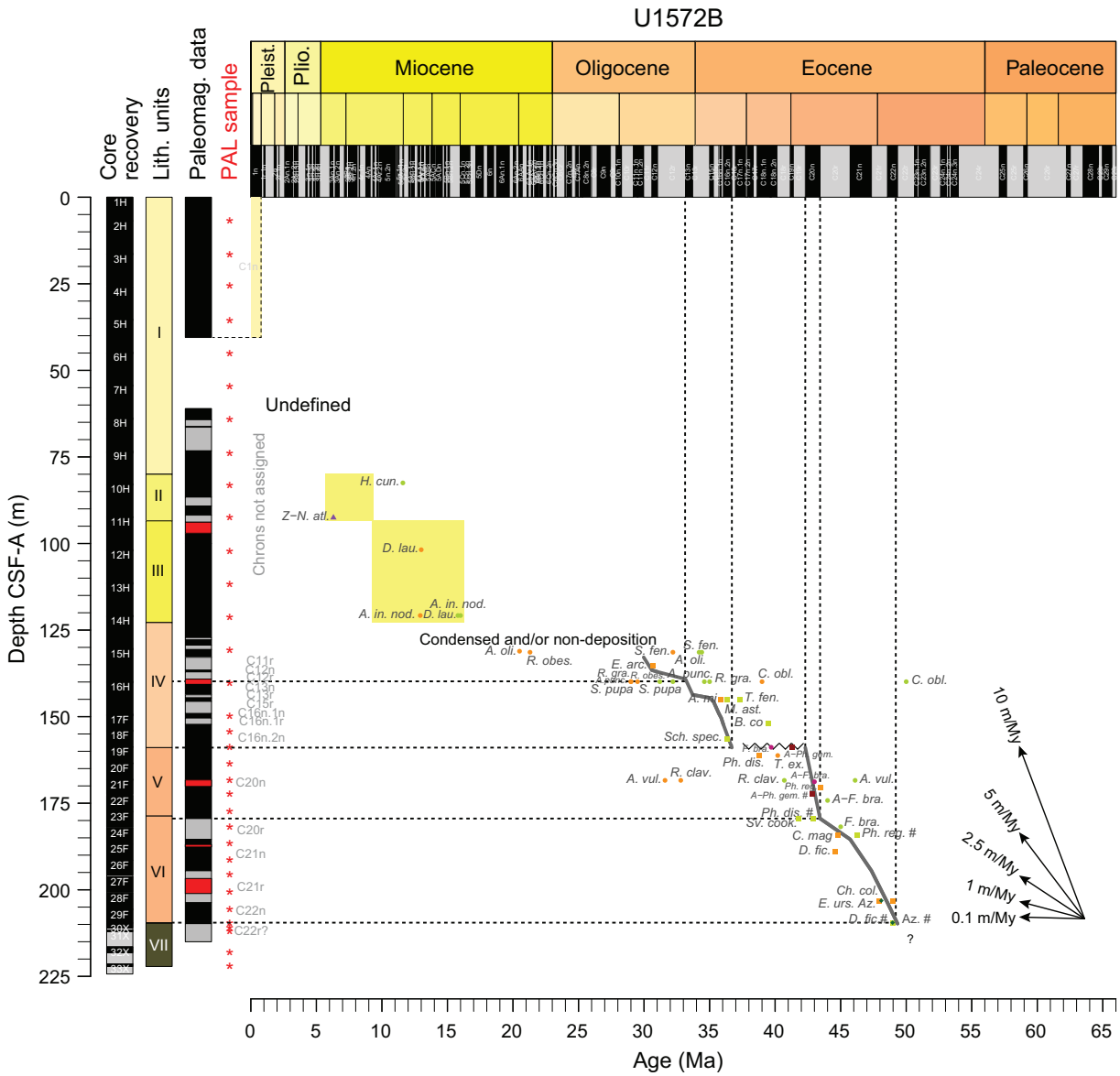

Figure F16. Age-depth estimates, Hole U1572B. Interpretation utilizes paleomagnetic reversal data, lithostratigraphic analyses, trends in physical property data, and bioevents. Abbreviations of bioevents are in Table T5. PAL = micropaleontological samples.

sediments shows unusually high pH and low alkalinity for saline water. Basalt alteration and associated clay authigenesis at Sites U1571 and U1572 likely result in enriched IW calcium contents (released during clay formation) and depleted Mg and K as these elements are incorporated into the clays. Elements in IW samples from the basalt–sediment transition to 50–100 m above it show largely conservative behavior downcore. Dissolved Si concentrations are sporadically enriched, and these intervals correspond to ash- or diatom-rich strata or both (e.g., Unit III). This is indicative of marine silicate weathering, and the high interstitial silica preserves some original features of volcanic glass, diatoms, and organic matter.

5.5.3.5. Physical properties

Lithostratigraphic Unit I comprises relatively high GRA bulk densities (~1.74 g/cm^3) and NGR (42 counts/s) that transition abruptly downward into Units II and III, which generally comprise lower GRA bulk density (~1.4–1.5 g/cm^3) and NGR (~23–25 counts/s) with an accompanying reduction in MS. The underlying Miocene to Eocene strata comprising Units IV–VI are best preserved in Hole U1572B, where Units IV and VI reveal elevated NGR (mean = >30 counts/s) compared with the intervening Unit V (mean = 21 counts/s); MS is also elevated in these intervals, which is likely linked to increased ash content in the Eocene.

The basaltic andesite–dominated Unit VII is characterized by high GRA bulk densities (2.53 g/cm^3) and *P*-wave velocities (4120 m/s) and low NGR (11 counts/s) in line with the data recorded for the basalt interiors found in Subunit VIIIb but at slightly higher NGR associated with the more evolved compositions. Point MS (MSP) and MS (592 and 401 × 10^{-5} [SI]) are a factor of 10 higher than for the overlying sedimentary units but about half that observed for the underlying basalt-dominated Unit VIII.

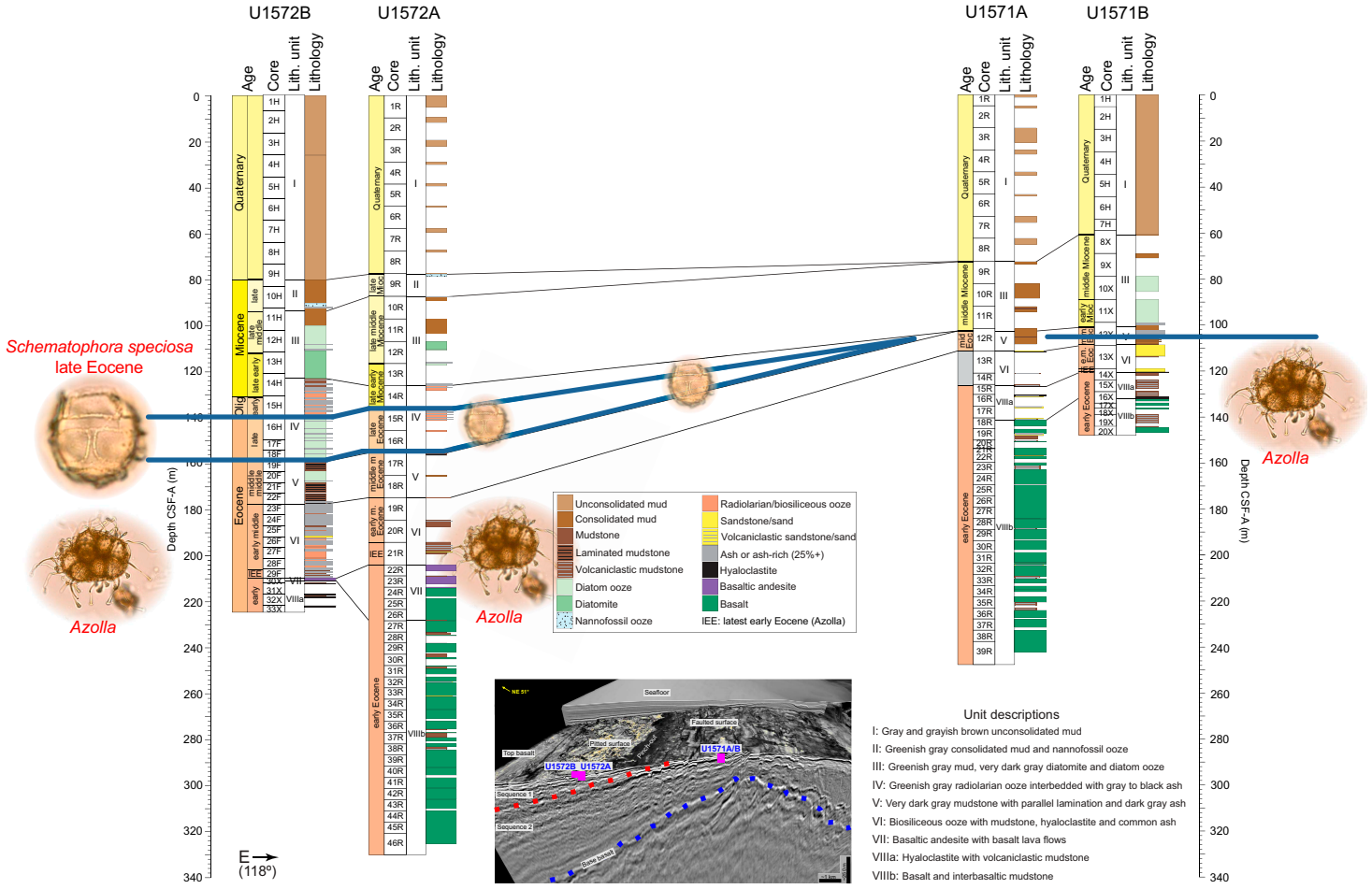

Figure F17. Lithostratigraphic and chronobiostratigraphic correlation panel, Sites U1571 and U1572. Note the absence of the Upper Eocene section at Site U1571. ? = unknown age.

A clear distinction is seen between the hyaloclastite Subunit VIIIa and lava-dominated Subunit VIIIb. The former has relatively low *P*-wave velocities (~1800 m/s) and GRA bulk densities (~1.55 g/cm^3) more in line with the low velocity, low bulk density interbasaltic sediments. Subunit VIIIb lavas reveal clear asymmetrical profiles of *P*-wave velocity and GRA bulk density ranging from ~5000 m/s and 2.9 g/cm^3, respectively, in the massive flow interiors to as low as ~2000 m/s and 1.5 g/cm^3, respectively, for porous and variably altered flow tops and bases. Calculated grain densities average 3 g/cm^3 for the basaltic sequences and exceed 3.1 g/cm^3 in some cases, attesting to the undifferentiated nature of the basaltic magmas that fed the sequence. Abundant primary pore spaces in the form of unfilled vesicles are identified throughout the volcanic sequence, leading to calculated porosities commonly >30%, whereas in certain cases these pores are filled with secondary minerals such as calcite and zeolite.

Table T5. Calcareous, biosiliceous, and organic microfossil biostratigraphic tie points used in the Hole U1572B age-depth model and abbreviations of taxa used in Figure F16. **Download table in CSV format.**

Bioevent	Top depth CSF-A (m)	Abbreviation	Age (Ma)	Reference	Type
FO *H. cuneiformis*	82.50	H.cun.	<11.6	J.A. Barron, 2021 database (Lazarus et al., 2014 in Janus)	DIAT
Zone *Neogloboquadrina atlantica* (sin.)	92.53	Z-N.atl.	6.3	Spiegler and Jansen, 1989	FORAM
LO *D. lauta*	101.80	D.lau.	13.0	J.A. Barron, 2021 database (Lazarus et al., 2014 in Janus)	DIAT
FO *A. ingens nodus*	120.80	A.in.nod.	15.8	J.A. Barron, 2021 database (Lazarus et al., 2014 in Janus)	DIAT
FO *D. lauta*	120.80	D.lau.	16.0	J.A. Barron, 2021 database (Lazarus et al., 2014 in Janus)	DIAT
LO *A. ingens nodus*	120.80	A.in.nod.	13.0	J.A. Barron, 2021 database (Lazarus et al., 2014 in Janus)	DIAT
LO *A. oligocenica*	131.10	A.oli.	20.5	J.A. Barron, 2021 database (Lazarus et al., 2014 in Janus)	DIAT
FO *A. oligocenica*	131.40	A.oli.	34.4	J.A. Barron, 2021 database (Lazarus et al., 2014 in Janus)	DIAT
FO *S. fennerae*	131.40	S.fen.	34.2	J.A. Barron, 2021 database (Lazarus et al., 2014 in Janus)	DIAT
LO *R. obesa*	131.40	R.obes.	21.3	J.A. Barron, 2021 database (Lazarus et al., 2014 in Janus)	DIAT
LO *S. fennerae*	131.40	S.fen.	32.2	J.A. Barron, 2021 database (Lazarus et al., 2014 in Janus)	DIAT
LO *E. arcuata*	135.42	E.arc.	30.7	Köthe et al., 2008	DINO
FO *A. punctifera*	139.90	A.punc.	35.0	J.A. Barron, 2021 database (Lazarus et al., 2014 in Janus)	DIAT
FO *C. oblongus*	139.90	C.obl.	50.0	J.A. Barron, 2021 database (Lazarus et al., 2014 in Janus)	DIAT
FO *R. granda*	139.90	R.gra.	34.6	J.A. Barron, 2021 database (Lazarus et al., 2014 in Janus)	DIAT
FO *R. obesa*	139.90	R.obes.	31.2	J.A. Barron, 2021 database (Lazarus et al., 2014 in Janus)	DIAT
FO *S. pupa*	139.90	S.pupa	32.2	J.A. Barron, 2021 database (Lazarus et al., 2014 in Janus)	DIAT
LO *A. punctifera*	139.90	A.punc.	29.0	J.A. Barron, 2021 database (Lazarus et al., 2014 in Janus)	DIAT
LO *C. oblongus*	139.90	C.obl.	39.0	J.A. Barron, 2021 database (Lazarus et al., 2014 in Janus)	DIAT
LO *R. granda*	139.90	R.gra.	29.5	J.A. Barron, 2021 database (Lazarus et al., 2014 in Janus)	DIAT
LO *S. pupa*	139.90	S.pupa	29.0	J.A. Barron, 2021 database (Lazarus et al., 2014 in Janus)	DIAT
FO *M. asterium*	144.95	M.ast.	36.34	Heilmann-Clausen and van Simaeys, 2005	DINO
FO *T. fenestrata*	144.95	T.fen.	37.29	Average from Bijl et al., 2021	DINO
LO *A. michoudii*	144.95	A.mi	35.85	Eldrett et al., 2004	DINO
FO *B. compta*	151.94	B.co	39.45	Williams et al., 1993	DINO
FO *Sch. spec.*	156.52	Sch.spec.	36.37	Average from Bijl et al., 2021	DINO
Acme *Ph. geminatum*	158.85	A-Ph.gem.	41.27	Eldrett et al., 2004	DINO
LO *F. brachiata*	158.85	F.bra.	39.7	J.A. Barron, 2021 database (Lazarus et al., 2014 in Janus)	DIAT
LO *Ph. distinctum*	161.22	Ph.dis.	38.8	Average from Eldrett et al., 2004	DINO
LO *T. excavata*	161.22	T.ex.	40.2	J.A. Barron, 2021 database (Lazarus et al., 2014 in Janus)	DIAT
FO *A. vulgaris*	168.40	A.vul.	46.1	J.A. Barron, 2021 database (Lazarus et al., 2014 in Janus)	DIAT
FO *R. claviger*	168.40	R.clav.	40.7	J.A. Barron, 2021 database (Lazarus et al., 2014 in Janus)	DIAT
LO *A. vulgaris*	168.40	A.vul.	31.6	J.A. Barron, 2021 database (Lazarus et al., 2014 in Janus)	DIAT
LO *R. claviger*	168.40	R.clav.	32.8	J.A. Barron, 2021 database (Lazarus et al., 2014 in Janus)	DIAT
LO *F. brachiata* acme	168.80	A-F.bra.	43	J.A. Barron, 2021 database (Lazarus et al., 2014 in Janus)	DIAT
LO *Ph. regalis*	170.35	Ph.reg.	43.44	Average from Eldrett et al., 2004	DINO
Acme *Ph. geminatum*	172.36	A-Ph.gem.#	42.87	Eldrett et al., 2004	DINO
FO *F. brachiata* acme	174.20	A-F.bra.	44	J.A. Barron, 2021 database (Lazarus et al., 2014 in Janus)	DIAT
FO *Ph. Distinctum*	179.56	Ph.dis.#	42.9	Average from Eldrett et al., 2004	DINO
FO *Sv. cooksoniae*	179.56	Sv.cook.	41.8	Average from Eldrett et al., 2004	DINO
FO *F. brachiata*	181.80	F.bra.	<45	Eldrett and Harding, 2009	DIAT
LO *T. heibergii*	181.80	T.hei.	<53.9	J.A. Barron, 2021 database (Lazarus et al., 2014 in Janus)	DIAT
LO *T. regina*	181.80	T.reg.	<54.5	J.A. Barron, 2021 database (Lazarus et al., 2014 in Janus)	DIAT
FO *Ph. regalis*	184.18	Ph.reg.#	46.27	Average from Eldrett et al., 2004	DINO
LO *C. magna*	184.18	C.mag	44.77	Average from Eldrett et al., 2004	DINO
LO *D. ficusoides*	189.02	D.fic.	44.58	Average from Eldrett et al., 2004	DINO
LO *Azolla*	203.13	Az.	48.1	Eldrett et al., 2004	AZOL
LO *Ch. columna*	203.13	Ch.col.	48.96	Average from Eldrett et al., 2004	DINO
LO *E. ursulae*	203.13	E.urs.	47.96	Eldrett et al., 2004	DINO
FO *Azolla*	209.49	Az.#	48.96	Eldrett et al., 2004	AZOL
FO *D. ficusoides*	209.49	D.fic.#	48.96	Eldrett et al., 2004	DINO

5.5.3.6. Downhole measurements

Wireline logging operations delivered a comprehensive data set covering approximately 147 m (about 80 m basaltic basement) in Hole U1571A and approximately 157 m (about 45 m basaltic basement) in Hole U1572A (Figure **F12**). Gamma radiation logging data aided in constraining the nature and distribution of more evolved igneous compositions in Lithostratigraphic Subunit VIIIa. A key objective of the Skoll High sites was to constrain the nature of different seismic facies associated with the top basalt reflector between the two sites, in particular the pitted surface seismic facies associated with Hole U1572A. The transition from sediment- to volcanic-dominated sequences in Hole U1571A comprises a more protracted sequence of interlayered hard volcanic units and softer sediments. In contrast, the transition from the sediments to the volcanic sequence in Hole U1572A is sharper, with an initial abrupt increase in density, PEF, and MS followed by a gradual increase in density over the following ~10 m culminating in a sharp increase in resistivity at ~220 m. Core observations suggest abundant lava-water interaction for Unit VIII, suggesting massive subaqueous flows and volcaniclastic units. This is consistent with the wireline data.

Gamma radiation also aided the identification and thickness quantification of several interlava sedimentary units that will form key future targets for palynology and isotopic age dating efforts to appraise the timing and environmental conditions of the eruption sequence. FMS image log data revealed high-resolution imaging of intricate volcanic intrafacies features such as ubiquitous unfilled vesicles, mineralized amygdules, pipe vesicles, and pillow lava features indicative of aqueous eruptions during the volcanic pile evolution.

5.6. Site U1573

Site U1573 consists of one RCB hole that aimed to characterize the basement nature of the Outer SDR. Hole U1573A resulted in coring about 90 m of late Early Eocene sediments that lie on top of basaltic basement. The 54 m of drilled basement consists of massive sheet flows that were emplaced in a shallow marine setting and are interlayered by sediments. The upper 300 m of the shallow sediments at the site were washed because an approaching storm did not leave enough time to core the entire hole.

5.6.1. Background and objectives

Site U1573 is located in the southern part of the Lofoten Basin just north of the Vøring Plateau at a 3167 m water depth (Figure **F15**) and on Magnetic Anomaly 23 near the border between the Vøring and Lofoten Margins. This part of the Vøring Margin has rarely been explored since the 1960s and 1970s. The only available basement samples prior to Expedition 396 in this area are from DSDP Leg 38 Site 343 (Talwani, Udintsev, et al., 1976), during which basement from 253 to 284 mbsf was drilled and about 5 m of highly altered basalts that were interpreted to be part of a sill intrusion were recovered.

Compared to the Vøring Margin, the Lofoten Margin is characterized by a narrower rift system, less extensive breakup-related magmatic crustal thickening, and a rapid increase of water depth from the shelf into the Lofoten Basin. The Lofoten Margin consists of three segments that are characterized by different fault dip directions and separated by crustal transfer systems (Tsikalas et al., 2001). The southernmost transfer system, the Bivrost Lineament, separates the Lofoten Margin from the Vøring Margin. Wide-angle seismic data suggest ~12 km thick oceanic crust in the southern part of the Lofoten Basin, much thinner than the about 20 km thick crust of the Vøring Plateau (Breivik et al., 2009). This difference in crustal thickness should have resulted in a vertical movement history of the Lofoten Margin that is very different than that of the Vøring Margin. The Early Eocene bathymetric gradient from the Vøring to the Lofoten Margins predicts a 500–1000 m water depth on the Lofoten Margin during breakup (Tsikalas et al., 2008). This implies contemporaneous submarine lava emplacement on the Lofoten Margin and subaerial lava emplacement on the Vøring Margin (Eldholm et al., 1989). This bathymetric gradient has been attributed to rapid initial margin subsidence along a deep-rooted low-angle detachment fault (Tsikalas et al., 2008). Reflection seismic data reveal a horizontal basement reflection underlain by SDR with lower seismic amplitude and shorter lateral extent than the main set of SDR on the Vøring Margin.

The stark difference between the subaerial lava flows at ODP Site 642 and the submarine conditions predicted by gravity modeling require distinctly different subsidence histories for the Vøring and Lofoten Margins. Thus, the first objective of drilling Site U1573 was to obtain information on the emplacement environment based on the facies of the recovered basalt and sediments. As such, reaching this first objective directly tests the predictions of seismic volcanostratigraphy. The second objective was to establish the timing of volcanism on the Lofoten Margin, in particular whether there is evidence of a time gap between the emplacement of the SDR of the Vøring Margin on Skoll High (Sites U1571 and U1572) and the Outer SDR. The third objective of Site U1573 was to constrain the conditions in the melt region during this presumably late phase of breakup volcanism. This includes not only any constraints on the composition of the mantle before melting and the ambient temperature and pressure from the geochemistry and petrology of the encountered rocks but also any signs of evolution of the melts in crustal magma chambers during breakup volcanism.

5.6.2. Operations

Site U1573 consists of a single hole drilled first without coring using the RCB system with a center bit from the seafloor to 300.0 mbsf and then cored to a final depth of 440.9 mbsf, including 54.4 m into basement. The average penetration rate in the basement section was ~1.82 m/h. There were frequent jammed liners and core catchers that contributed to relatively low core recovery rates within the basement (average = 43%). Coring in Hole U1573A was terminated at 1830 h on 20 September 2021 because of severe weather and heavy sea conditions that were expected over the operational area for the following day. The last core recovered was Core 19R at 1925 h on 20 September. The drill string was pulled back on board at 2200 h. The BHA was broken down, and the drill collars were secured in the drill collar rack. The rig floor was secured at 0705 h on 21 September, ending Hole U1573A and Site U1573. A total of 101.0 h or 4.2 days were spent on site. A total of 18 cores were recovered using the RCB system over 140.9 m recovering 101 m (72%).

5.6.3. Principal results

5.6.3.1. Lithostratigraphy

Site U1573 consists of a single hole that was drilled to 440.9 m CSF-A, with the recovered core interval spanning 300 to 440.9 m CSF-A. The 140.9 m thick succession consists of both sediments and basalts that are divided into four lithostratigraphic units. The criteria for the division of the units are based on significant lithologic changes, which are supported by physical properties variability. Lithostratigraphic Units I–III are sedimentary, and Unit IV consists of basalt and interbasaltic sediments.

Unit I consists of dark greenish gray to very dark gray claystone with rare weak parallel lamination or fining-upward sequences. Slight to heavy bioturbation is present throughout the unit, and diagenetic pyrite is observed locally. Unit II consists of dark greenish gray to very dark gray claystone with moderate bioturbation alternating with very dark gray organic-rich claystone with thin parallel lamination. Rare ash beds or ash-rich beds are present locally. Unit III consists of very dark gray to very dark bluish gray volcaniclastic claystone mudstone with sand. Unit IV consists mainly of gray to dark gray aphyric aphanitic to phaneritic basalt and interbasaltic claystone to sandstone.

5.6.3.2. Biostratigraphy

All sedimentary core catcher samples and selected samples from intercalated sedimentary beds in the igneous facies from Hole U1573A were processed for calcareous, siliceous, and organic microfossils. Calcareous and siliceous biogenic material was largely absent, with the exception of rare calcareous nannofossil occurrences in the lower several meters above basalt. However, most samples were productive for palynology, including some samples from between the igneous facies, and most yielded age diagnostic dinocysts, which indicate a late Early Eocene age for the entire interval.

5.6.3.3. Paleomagnetism

Lithostratigraphic Unit I is characterized by an average intensity of magnetization of 0.05 A/m and a median coercivity of 2.73. This coercivity may be owed to sedimentary hematite or goethite. The

unique discrete sample measured is not ferromagnetic, devoid of magnetite, because the average bulk MS is 0.447×10^{-3} [SI].

Unit II has an 0.05 A/m average intensity of magnetization. The median coercivity (3.04), MS ($\kappa < 1.03 \times 10^{-3}$ [SI]), and corrected degree of anisotropy ($P' < 1.105$) are higher than in Unit I. High κ results from small contributions from magnetite. High coercivity and P' may be due to a higher goethite/hematite ratio or a larger iron sulfide (e.g., pyrrhotite) population in the ash or both. Multiple minerals carrying remanence are evident from the three types of remanent magnetization identified in four discrete samples. The low- and medium-coercivity component is erased by AFs of 20 and 70 mT, respectively. The high-coercivity component is stable throughout the demagnetization process, specifically in the 120 mT field.

Unit III has an average intensity of magnetization of 0.07 A/m, which is slightly higher than in Units I and II. In contrast, the medium coercivity (2.53) is lower than in Units I and II. Lower median coercivity can be related to domination of volcanic material, which usually is richer in iron sulfide (e.g., pyrrhotite) but poorer in goethite and hematite. Note that goethite and hematite have higher coercivity than iron sulfides. No discrete samples were measured.

Unit IV has high average intensity of magnetization (2.6 A/m) and high median coercivity (6.02). Such high coercivities may be owed to a larger goethite/hematite ratio. The unit is ferromagnetic with the highest bulk MS of all the units, indicating the dominance of magnetite. However, the corrected degree of anisotropy is the lowest among all the units. This indicates that the magnetic fabrics are carried dominantly by magnetite and the populations of pyrrhotite and hematite are small. Three magnetization components are conspicuous from the demagnetization behavior of the discrete samples.

Unit I has four short periods of magnetic reversals between Sections 396-U1573A-2R-1 (300 mbsf) and 2R-5 (306.71 m). This is followed by a long episode of magnetic reversal in Sections 4R-2 (321.05 mbsf) through 5R-5 (333.91 mbsf) in Unit II. After this, the magnetic polarity flips several times at a relatively higher frequency (within a couple meters) to Section 7R-3 (350.98 mbsf); it then remains reversed through Section 8R-3 (361.72 mbsf). After that, the polarity stays dominantly normal in the rest of the hole through Section 18R-2 (436.74 mbsf). Preliminary data from paleomagnetic analyses suggest a predominance of normal polarity at the top of the cored succession, which we tentatively assign to Magnetochron C22n (48.57–49.34 Ma).

5.6.3.4. Geochemistry

Site U1573 provided a unique opportunity to sample an Outer SDR sequence on a magma-rich passive continental margin. The sampled lavas are noteworthy in that the higher silica and low-Ti compositions are chemically distinct from both typical mid-ocean-ridge basalts and LIP magmatism. The sedimentary package recovered above the lavas is limited to 100 m. As seen at previous sites, high organic matter production or preservation is found in volcaniclastic sediments, suggesting a causal relationship. The IW samples show a diagenetic environment controlled by basalt weathering, with processes consuming alkalinity in the overlying sedimentary strata. There is also strong evidence of authigenic carbonate formation above the sediment/basalt contact, linked to the liberation of Ca during the weathering of primary silicates.

5.6.3.5. Physical properties

Lithostratigraphic Units I and II are characterized by downward increasing density (from ~1.6 to ~2 g/cm^3) consistent with increasing compaction. NGR fluctuates between ~30 and 60 counts/s and displays a general increase with depth. Increased scatter in MS is observed over ash-rich intervals within sedimentary sections. The hard rock basement sequence comprises generally very low NGR, typically <10 counts/s, consistent with the basalt-dominated compositions, and has generally high density (mean GRA bulk density = 2.28 g/cm^3; mean MAD grain density = 2.83 g/cm^3) and velocities (mean = 3660 m/s). The presence and nature of interlava sediments with lower velocity (~2000 m/s) compared to the higher velocity basaltic flows (~4500 m/s) give first insights into the geological causes of the Outer SDR seismic reflectivity.

5.7. Site U1574

Three holes were drilled at Site U1574 targeting the basement and the overlying sedimentary sequence of an Outer High, Eldhø, located on the northern flank of the Vøring Plateau. Hole U1574A was drilled with the RCB system and sampled 94 m of pillow basalts, hyaloclastites, and a ~30 m thick interbasaltic sedimentary interval. Both triple combo and FMS-sonic wireline log data were acquired in the basement. Only one APC core was collected in Hole U1574B, whereas a 170 m thick sequence of sediments was almost completely recovered using APC coring in Hole U1574C. The last core of the expedition was an XCB core recovering 1.5 m of pillow and massive basalts, sediments, and hyaloclastites.

5.7.1. Background and objectives

Site U1574 probes the top of an Outer High called Eldhø (Figure **F15**). It is located on the northern flank of the Vøring Plateau at a 2825 m water depth. Outer Highs are conspicuous volcanic seismic facies units that are located seaward of the Inner SDR facies units (Hopper et al., 1992; Planke et al., 2000; Franke et al., 2019). Although most volcanic seismic facies units are relatively continuous along a rifted margin, Outer Highs have a limited lateral extent of typically 10–20 km (Berndt et al., 2001a). They form elongate structures that rise above the top of the adjacent Inner and Outer SDR. Seismically, Outer Highs frequently display a high-amplitude top reflection of normal seismic polarity, chaotic internal reflection patterns, and high-amplitude reflections that extend from the Outer High into adjacent sedimentary sequences that overlie the SDR.

Because Outer Highs are characteristic features of volcanic rifted margins located between Inner and Outer SDR, their presence likely signifies specific geological processes and provides clues to the evolution of volcanic passive margins. Precruise interpretations of Outer Highs mainly relied on seismic volcanostratigraphic interpretations, field analogs, and geological reasoning. The facies unit was interpreted as dominantly hyaloclastite deposits formed when the eruption fissures were submerged during the initial phase of seafloor spreading. In this situation, eruptions would happen at sea level or in shallow marine conditions and lava would get into direct contact with seawater, leading to phreatomagmatic eruptions. The formation of Surtsey between 1964 and 1968 may serve as a recent analog (Kokelaar, 1983).

The structure targeted at Site U1574 is a typical example of an Outer High (Figure **F7B**). We call this structure Eldhø, meaning fire mountain in Scandinavian languages. The name is also inspired by the achievements of Professor Olav Eldholm, a pioneer in drilling and defining the concepts of volcanic margins and LIPs (e.g., Eldholm et al., 1989). Eldhø rises more than 1500 m above the adjacent Inner SDR in the southeast and about 650 m above the Outer SDR in the northwest with numerous high-amplitude seismic reflections that transgress into the adjacent sedimentary basins south of the high. Its lateral extent is about 17 km in the dip direction (northwest–southeast) and about 30 km along strike (southwest–northeast). A sedimentary basin, the Eldhø Basin, which has kilometer-thick postbasalt sediment deposits, is located landward of Eldhø.

The first objective of Site U1574 was to obtain information on the emplacement environment based on observations of the drilled volcanic facies. If Eldhø was indeed emplaced close to sea level, this will validate these aspects of seismic volcanostratigraphy, and their presence may then be used as a marker for vertical movement. The second objective was to constrain the conditions in the melt region, specifically the composition of the mantle before melting and the ambient temperature and pressure conditions in the melt region during the late phase of breakup volcanism based on the geochemical composition and petrology of the encountered rocks. Reaching the first two objectives will allow us to parameterize geodynamic models for excessive breakup volcanism.

Site U1574 was also drilled to provide information on the suitability of the breakup basalt sequences and interbedded sediments for permanent geological storage of CO_2. If the Outer Highs indeed consist mainly of hyaloclastite deposits as postulated, they should be characterized by high porosity and permeability, which may make them a suitable target CO_2 storage. Finally, we hoped to obtain information on the earliest incursion of deep water into the North Atlantic and the extent of freshwater incursions into the young ocean during the Early to Middle Eocene (Brinkhuis et al., 2006) by coring the overlying sedimentary strata.

5.7.2. Operations

Site U1574 consists of three holes. The first hole was cored using the RCB coring system (Figure F4) from the seafloor to 260.0 mbsf and then logged with the triple combo and FMS-sonic logging tool strings. The original plan for Site U1574 was to core a single hole to 310 mbsf, but the objectives were achieved by 260 mbsf. After completing Hole U1574A, it was decided that the remaining expedition time would be used to piston core the sediment section above the basement and to attempt to improve recovery of the sediment/basement interface. The APC/XCB coring system was selected for the second hole at the site. After assembling and lowering the APC/XCB system to the seafloor, the first APC core misfired and penetrated the seafloor at least twice. Hole U1574B was terminated after the poor mudline core at 9.5 mbsf. The vessel was offset 20 m south, and Hole U1574C was APC cored to 169.2 mbsf. We conducted four borehole temperature measurements with the advanced piston corer temperature (APCT-3) tool on Cores 4H (38.0 mbsf), 7H (66.1 mbsf), 10H (94.6 mbsf), and 13H (118.7 mbsf). The Icefield MI-5 core orientation tool was deployed for the first 10 cores. The XCB coring system was deployed after the last APC core and immediately cored the basement. A PDC XCB cutting shoe was used to core a hard layer at 169.2 mbsf. Coring in Hole U1574C was terminated at 1630 h on 1 October 2021 at a final depth of 171.5 mbsf. The last core was on deck at 1655 h. All coring tools were put away. The drill string was pulled back to the surface after clearing the seafloor at 1920 h. The drill collars were laid out to the drill collar racks, and the outer core barrel was disassembled and secured. The drill floor was secured for transit at 0231 h on 2 October, ending Hole U1574C and Site U1574. A total of 182.5 h or 7.6 days were recorded while on Site U1574.

A total of 59 cores were recorded for the site. The RCB system was used exclusively for Hole U1574A, coring 260.0 m and recovering 88.41 m of core (34%). The APC system was used in both Holes U1574B and U1574C. A total of 20 APC cores were recovered over a 178.7 m interval, recovering 183.27 m of core (103%). The XCB system was used for one core over a 2.3 m interval and recovered 64% of the cored interval.

5.7.3. Principal results

5.7.3.1. Lithostratigraphy

Site U1574 is located on the lower slope of the Vøring Plateau, on the southern flank of Eldhø. This Outer High was likely formed by subaqueous volcanism during the initial phase of seafloor spreading. The succession of recovered material consists of both sediments and basalts and is divided into five lithostratigraphic units. The division of the units is based on changes in lithology, which coincide with changes in physical property trends. Lithostratigraphic Units I–IV are sedimentary, and Unit V consists of basalt, hyaloclastite, and minor interbasaltic sediments.

Unit I consists of brown and brownish gray unconsolidated mud with intervals of rare pebbles, likely related to ice-rafted debris, and rare to common foraminifers. Unit II consists of pale yellow and grayish green consolidated mud, in which the first Eocene-aged dinocyst zonations are encountered. Unit III is very dark gray mudstone with rare beds of sandstone and ash and some parallel lamination and bioturbation, showing an increase in organic content downhole. Unit IV is very dark gray to very dark grayish brown organic rich mudstone with thin parallel lamination. Compared to the overlying units, Unit IV is richer in foraminifers and nannofossils, with abundances increasing downhole in the unit.

Unit V mainly consists of aphyric- to plagioclase-phyric pillow basalt with localized hyaloclastite and rare interbedded mudstone. Unit V is divided into two subunits (Va and Vb) based on lithologic and geochemical variations. Both subunits are separated by a large interval of no recovery to very poor recovery of sediments, and both are overlain by hyaloclastites. Subunit Va contains both massive and pillow basalts and shows significant variation of composition with depth. Subunit Vb contains primarily pillow basalt and presents remarkably uniform composition.

5.7.3.2. Biostratigraphy

Except for Cores 396-U1574A-1R through 3R, all sedimentary core catcher samples from Hole U1574A were processed for palynology. These samples, including two taken from between basalt flows (Samples 32R-CC and 33R-CC), are assigned a late Early Eocene age based on marker dino-

cyst taxa and broader assemblage characteristics. The overlying Quaternary strata yield calcareous and rare biosiliceous fossil remains, but these are largely absent from most of the expanded late Early Eocene strata. A significant exception is the lower ~20 m of sediment on top of the igneous basement (Samples 17R-CC and 18R-CC), which contains calcareous remains, including calcareous nannofossils, planktonic and benthic foraminifers, (micro)molluscs, and fine preservation of aragonitic pteropods. Benthic foraminifers are mostly mineral filled, and diatoms are replaced by or coated with pyrite (micro)framboids. These samples are tentatively attributed to planktonic foraminifer Zone E7a of Wade et al. (2011), in line with inferences from dinocyst biostratigraphy.

5.7.3.3. Paleomagnetism

Lithostratigraphic Units I–III are characterized by low average intensity of magnetization (0.02, 0.006, and 0.02 A/m, respectively), whereas their median coercivity is 1.69, 1.31, and 0.87, respectively. The lower intensity of magnetization and coercivity may be owed to a smaller population of magnetic minerals. No discrete samples were measured for these three units. Unit IV has a slightly higher average intensity of magnetization (0.006 A/m) than Units I–II. The bulk MS is 1.06×10^{-3} to 0.014×10^{-3} [SI], indicating a ferro + paramagnetic AMS without magnetite. Median coercivity is much higher than in Units I–III. The corrected degree of anisotropy in the range of ~1.1 and median coercivity of 2.61 indicate the absence of micaceous minerals and a higher population of goethite and hematite, respectively. Only one of the two discrete samples presents stable magnetization directions (Sample 396-U1574A-17R-1, 111–113 cm). The low-coercivity remanent magnetization component is erased by a field of 10 mT. The high-coercivity component is removed at an applied field of 100 mT.

The average intensity of magnetization (4.38 A/m) in Unit V is several orders of magnitude higher than in the other units. The median coercivity (2.61) is the same as in Unit IV. The bulk MS is $\sim 15 \times 10^{-3}$ [SI], and the corrected degree of anisotropy is P' ~1.1. Two magnetization components are evident. The low-coercivity component is erased by application of a field of 10 mT. The high-coercivity component is removed by a field of 40–60 mT. The magnetic signals are apparently carried by magnetite.

Magnetic polarity is normal through Section 396-U1574A-4R-2 (31.05 mbsf). The polarity then remains dominantly reversed to the bottom of the hole (Section 38R-3; 258.15 mbsf). This long, dominantly reversed polarity episode is truncated by short-lived positive polarity events.

5.7.3.4. Geochemistry

At Site U1574, Lithostratigraphic Unit IV consists of low-Ti basalts. Significant variability of some geochemical parameters (TiO_2, Mg#, Ni, and Zr) downcore suggests recovery of multiple flow units. Interbasalt sediments contain what appears to be dolomite.

IW compositions in Units I–III indicate a diagenetic environment dominated by the weathering of primary silicate phases and the formation of authigenic clays and carbonate. Calcium and Sr decrease downcore due to their release in the formation of smectite and other clay minerals. The same formation reactions lead to the removal of Mg and K from the IW, resulting in decreasing Mg and K content downcore. Enrichment of other elements (e.g., Si and B) in the upper 40 m of the core suggest a lithology-controlled elemental composition of the IW.

5.7.3.5. Physical properties

Lithostratigraphic Unit I has high bulk densities (mean = 1.82 g/cm^3) and NGR (average = 38 counts/s) and relatively low *P*-wave velocities (~1575 m/s) and MS ($\sim 45 \times 10^{-5}$ [SI]). Eight MAD samples collected throughout this unit have an average bulk density of 1.82 g/cm^3, grain density of 2.76 g/cm^3, and porosity of 54%. Six thermal conductivity measurements range 1.1–1.5 W/(m·K) (average = 1.3 W/[m·K]).

In Unit II, *P*-wave velocities, GRA bulk densities, MS, and NGR average ~1550 m/s, 1.43 g/cm^3, $\sim 21 \times 10^{-5}$ [SI], and 19 counts/s, respectively. Analysis of two MAD samples revealed very high porosities of 83%, a grain density of 2.70 g/cm^3, and a bulk density of 1.31 g/cm^3, consistent with poorly compacted clay-rich sediments.

A total of 25 discrete MAD sample analyses indicate a mean bulk density of 1.59 g/cm^3 for the ~90 m thick Eocene Unit III, slightly lower than the mean GRA bulk density of 1.62 g/cm^3. Porosities range 37%–82%. The baseline values of the measured physical properties generally increase with depth throughout Unit III. Whole-round *P*-wave velocities average 1560 m/s, ~250 m/s slower than velocities measured through 30 discrete *P*-wave caliper measurements using the SHMG, and have a significant spread with a standard deviation of 120.5 m/s. MS increases compared to Unit II (average = 105 × 10^{-5} [SI]) and features increased scattering linked to the occurrence of ash layers.

Reduced MS scatter (mean = ~90 × 10^{-5} [SI]) is observed for Unit IV. Mean GRA (~1.83 g/cm^3) and MAD (~1.73 g/cm^3; n = 8) bulk densities correspond well to an associated average porosity of 59%. Whole-round *P*-wave velocities with a mean of 1565 m/s are within 20 m/s of the mean recorded using *P*-wave caliper measurements and similar to average *P*-wave velocities found for Unit III. NGR increases slightly compared to the overlying unit and has a constant value around 51 counts/s.

The massive basalt and pillow basalts from Unit V have significantly higher *P*-wave velocities, bulk densities (2.4–2.6 g/cm^3), and MS (1000–2000 × 10^{-5} [SI]) than those found for the overlying sedimentary successions. Similar to interbasaltic sediments, the NGR counts, *P*-wave velocities, and bulk densities measured for the hyaloclastite intervals feature a similar but inverse response to those measured for the pillow and massive basalts because *P*-wave velocities were on average 1000–1500 m/s lower than the 4000–5000 m/s typically associated with the pillow lavas and massive intervals. Mean *P*-wave velocities of the massive basalt intervals typically featured on the lower end of this range. The unit has relatively low porosities (15%–20%), although significantly higher porosities are recorded for the interbasaltic layers.

5.7.3.6. Downhole logging

Logging operations collected important data for intervals with poor core recovery in challenging logging conditions where hole instability resulted in only partial data collection for the bottom ~50 m of the open hole section. The basaltic composition pillow lavas are characterized by high densities (~2.6 g/cm^3) and fluctuating velocities ranging ~3–5.2 km/s with associated low gamma radiation (~9 gAPI). FMS imaging of the formation reveals pillow structures and the presence of lava flow units, which correspond to highly vesicular basalt in the recovered core. Wireline data also show the presence of three thin elevated gamma radiation sediment layers along with a much thicker interval of high gamma radiation (~70 gAPI) stratigraphy associated with an interval of ~30 m with almost no core recovery. This layer is imaged with the FMS, which records a resistive fractured nature with traces of potential pillow-like features and possible sediment layering toward the base.

6. Preliminary scientific assessment

During Expedition 396, we collected data from 21 boreholes in five different geological settings along the volcanic rifted margin off mid-Norway. The boreholes probe almost all elements of a typical volcanic rifted margin and the associated sedimentary archive. Recovery ranges from the subbasalt stratigraphy through hydrothermal vent complex deposits, thick flood basalts deposits in SDR sequences to postbreakup phreatomagmatic volcanoes, and basalts representing thickened oceanic crust formed during early seafloor spreading. The cored sediments include a comprehensive record of the Upper Paleocene and Lower Eocene strata, including expanded sections of the PETM. Thick Lower Eocene sediments recovered above the uppermost basalt horizon document the environment and subsidence history of the margin during the initial stages of northeast Atlantic Ocean formation. Along with an enormous amount of high-quality 2-D and 3-D seismic data and legacy boreholes from DSDP, ODP, and the NPD, Expedition 396 results will allow us to assess and reevaluate the development of volcanic rifted margins and the implications of LIPs on paleoclimate and mass extinctions.

In spite of the ambitious work program set out in the *Scientific Prospectus*, it was possible to significantly surpass our operational and scientific objectives. The expedition results provide a scien-

tific database much broader than anticipated and should allow us to reach all the expedition's objectives during postcruise work.

6.1. Primary objectives

The first main objective of the expedition was to constrain the tectonomagmatic processes that lead to excess volcanism during the formation of a new ocean. Magmatism is controlled by the composition and rheological properties of the upper mantle, the initial pressure and temperature conditions, and the tectonically controlled unloading of the mantle through space and time. These boundary conditions will ultimately control the response of the system, including induced convection, passive, and active upwelling—processes that move mantle material into the melt window. We drilled 587 m of breakup-related basalts in eight different holes that cover a wide range of compositions. Cores from these holes will allow us to constrain the pressure and temperature conditions and the composition of the upper mantle during various phases of breakup volcanism through geochemical analyses, whereas the age of the magmatism will be constrained by geochronology. The igneous rocks comprise the main Inner SDR units, the Outer High, and the Outer SDR unit as well as an enigmatic dacitic unit along the Vøring Transform Margin. These Expedition 396 data will be complemented by boreholes into a lava delta on the Møre Margin by NPD and samples of the earliest lava flows on the Vøring Margin that were recovered in ODP Hole 642E. High-precision radiometric dating, biostratigraphy of interbasalt sediments, and paleomagnetic studies will allow us to constrain the age and rates of the magmatism in unprecedented detail. Furthermore, the samples allow a direct assessment of the paleowater depth, specifically, subaerial versus marine emplacement of the extrusive basalts. Along with paleoenvironmental studies of the immediate sedimentary succession above the basalts by biostratigraphic and sedimentological analyses, this will constrain the vertical movements of the margin and by proxy (and in conjunction with the geophysically constrained magmatic crustal thickening) the rifting history of the margin. This is a main boundary condition for numerical simulation of the tectonomagmatic breakup processes that will allow us to reach the first objective of the expedition.

The second main objective of the expedition was to study the environmental consequences of breakup volcanism through time. Breakup volcanism in the northeast Atlantic was accompanied by a phase of rapid global warming, the so-called PETM. With the results of Expedition 396, and Sites U1567 and U1568 specifically, we will test if the observed global warming may have been induced by magmatic intrusions into the surrounding sedimentary basins. It has been proposed that the intrusions led to contact metamorphism in the host rock and expulsion of carbon-bearing hydrothermal fluids through pipe-like vent complexes into the young ocean basin and from there onward into the atmosphere.

During Expedition 396, we successfully recovered 240 m of sediments of PETM age from eight boreholes in vent structures and their immediate vicinity in the southern Vøring Basin (Figure **F8**). These cores will allow us to test the hypothesis by biostratigraphic, sedimentological, and geochemical analyses along with integration of wireline logs and high-resolution 3-D seismic data. A total of 1955 m of Paleocene and Eocene age sedimentary rocks were drilled during Expedition 396, with a recovery of 1125 m (58%) (Table **T6**). These cores represent a comprehensive archive of the environmental changes that took place from the onset of the EECO through the PETM and into the Middle and Late Eocene. The proxy data derived from the postcruise analyses will provide insights into the various drivers and responses in the earth system during these times of a global hothouse climate and subsequent cooling.

6.2. Secondary objectives

The comprehensive Expedition 396 database will also be used to study the opening of the north Atlantic seaways, the onset of ocean circulation patterns, and the occurrence of freshwater incursions into the young ocean basins. We have encountered the remains of the freshwater fern *Azolla* spp. in several of the expedition boreholes, and further analyses will provide a crucial documentation between its massive occurrence in the Arctic Ocean, Norwegian Greenland Sea, and North Sea areas and sites in the Labrador Sea on the east coast of North America.

Table T6. Assessment, Expedition 396. **Download table in CSV format.**

Location	Proposed drilling	Target	Max depth (mbsf)	Drilled holes	Main result	Logs	Total (m)	Recovery (m)	Target (m)	Comments
Kolga High basalts	20A 1 hole	Subbasalt	200 (30)	U1565 2 holes	Monzogranite basement		60	20	11	Target reached. Initial basalt and interbasalt sediments cored and logged in Hole U1566A. Subbasalt granitic rocks cored at both sites.
	23A 1 hole	Initial basalt and subbasalt	200 (25)	U1566 1 hole	Basalt flows with sediments, alkali granite below	4 runs	182	100	158	
N Modgunn vent complex	31A 1 hole	Sediments across PE transition	200 (55)	U1567 3 holes	Paleocene, Paleocene–Eocene transition, PETM, vent infill	2 runs	384	303	282	Target reached. Hole U1567A is a reference hole across the Paleocene/Eocene boundary. The other four holes provide a detailed sampling of the vent complex in-fill, including the PETM. Abundant ash layers recovered, and two holes were logged.
	40B 2 holes	Vent complex, Paleogene	200 (55)	U1568 2 holes	Vent infill, PETM, Late Paleocene	2 runs	325	239	252	
Mimir High Paleogene	55B 2 holes	Early Eocene to Late Paleocene	800 (255)	U1569 1 hole	Expanded Early Eocene, PETM, Late Paleocene	Bridge	405	145	268	Target reached. Site U1569 sampled the Early Eocene, the PETM, and the Late Paleocene before total depth at 405 mbsf. Ribbon sites provided complimentary sampling of the Early Eocene, the PETM, and Middle and Late Paleocene, with very pristine microfossils. Abundant ash layers. A thin igneous unit was cored in two holes.
	56A (alt) ribbon	Paleocene to earliest Eocene	200	U1570 4 holes	Expanded Early Eocene, PETM, Paleocene; dacite unit	2 runs	764	270	603	
Skoll High basalts	61A 1 hole	Lava field—Landward Flows	240 (125)	U1571 2 holes	Subaerial basalt flows with sediments	3 runs	391	229	164	Target reached. Hole U1571A cored and logged a sequence of subaerial tabular lava flows and interbasalt red sediments. A very different basalt sequence was sampled in the upper 50 m of the basalt basement in U1572A, likely deposited in an aquatic environment; interlava black sediments.
	7A 1 hole	Pitted basalt flows/SDR	320 (220)	U1572 2 holes	Mixed basalts with various sediments	1 run collapse	555	359	142	
Lofoten Basin Eldhø basalts	9A 2 holes	Basalts of Outer SDR	550 (450)	U1573 1 hole	Sheet flows with interbasalt sediments		441	141	59	Target reached. Hole U1573A cored a sequence of basalt flows with interbedded marine sediments, one of which could be data. A very different basalt sequence was sampled at U1574, including hyaloclastites, pillow basalts, and massive flows. Dominantly Eocene and some Quaternary sediment cores above the basaltic basement. Note: Hole U1574B (10 m) failed.
	80A 1 hole	Volcanoclastic Outer High	310 (210)	U1574 3 holes	Hyaloclastite, pillow basalts, massive flows with Eocene sediments	2 runs	442	273	96	
Totals:	12 holes		3720 (1935)	21 holes		17 runs	3949	2079	2035	Note: In total, 385 m was washed.

Finally, the recovered 587 m of various basaltic facies units will be invaluable to achieve the other secondary objective, namely, the study of the suitability of the breakup basalt successions for the permanent storage of CO_2. Some of the recovered basalts are very vesicular, providing large reaction surfaces that make them potential reservoir rocks for permanent carbon storage. Detailed analyses and integration with geophysical data will allow us to extrapolate these findings in three dimensions and form the basis for a robust assessment of the storage potential.

References

Aarnes, I., Svensen, H., Connolly, J.A.D., and Podladchikov, Y.Y., 2010. How contact metamorphism can trigger global climate changes: modeling gas generation around igneous sills in sedimentary basins. Geochimica et Cosmochimica Acta, 74(24):7179–7195. **https://doi.org/10.1016/j.gca.2010.09.011**

Abdelmalak, M.M., Faleide, J.I., Planke, S., Gernigon, L., Zastrozhnov, D., Shephard, G.E., and Myklebust, R., 2017. The T-reflection and the deep crustal structure of the Vøring margin, offshore mid-Norway. Tectonics, 36(11):2497–2523. **https://doi.org/10.1002/2017TC004617**

Abdelmalak, M.M., Meyer, R., Planke, S., Faleide, J.I., Gernigon, L., Frieling, J., Sluijs, A., Reichart, G.J., Zastrozhnov, D., Theissen-Krah, S., Said, A., and Myklebust, R., 2016a. Pre-breakup magmatism on the Vøring margin: insight from new sub-basalt imaging and results from Ocean Drilling Program Hole 642E. Tectonophysics, 675:258–274. **https://doi.org/10.1016/j.tecto.2016.02.037**

Abdelmalak, M.M., Planke, S., Faleide, J.I., Jerram, D.A., Zastrozhnov, D., Eide, S., and Myklebust, R., 2016b. The development of volcanic sequences at rifted margins: new insights from the structure and morphology of the Vøring Escarpment, mid-Norwegian Margin. Journal of Geophysical Research: Solid Earth, 121(7):5212–5236. **https://doi.org/10.1002/2015JB012788**

Abdelmalak, M.M., Planke, S., Polteau, S., Hartz, E.H., Faleide, J.I., Tegner, C., Jerram, D.A., Millett, J.M., and Myklebust, R., 2019. Breakup volcanism and plate tectonics in the NW Atlantic. Tectonophysics, 760:267–296. **https://doi.org/10.1016/j.tecto.2018.08.002**

Anagnostou, E., John, E.H., Edgar, K.M., Foster, G.L., Ridgwell, A., Inglis, G.N., Pancost, R.D., Lunt, D.J., and Pearson, P.N., 2016. Changing atmospheric CO_2 concentration was the primary driver of early Cenozoic climate. Nature, 533(7603):380–384. **https://doi.org/10.1038/nature17423**

Baby, G., Guillocheau, F., Boulogne, C., Robin, C., and Dall'Asta, M., 2018. Uplift history of a transform continental margin revealed by the stratigraphic record: the case of the Agulhas transform margin along the Southern African Plateau. Tectonophysics, 731–732:104–130. **https://doi.org/10.1016/j.tecto.2018.03.014**

Bakke, V.N., 2017. Volcanic rocks at the Møre marginal high: geochemistry, petrogenesis and emplacement mechanisms [MS thesis]. University of Bergen, Norway. **https://bora.uib.no/bora-xmlui/handle/1956/15974**

Barke, J., Abels, H.A., Sangiorgi, F., Greenwood, D.R., Sweet, A.R., Donders, T., Reichart, G.-J., Lotter, A.F., and Brinkhuis, H., 2011. Orbitally forced Azolla blooms and middle Eocene Arctic hydrology: clues from palynology. Geology, 39(5):427–430. **https://doi.org/10.1130/G31640.1**

Basile, C., and Allemand, P., 2002. Erosion and flexural uplift along transform faults. Geophysical Journal International, 151(2):646–653. **https://doi.org/10.1046/j.1365-246X.2002.01805.x**

Berndt, C., Hensen, C., Mortera-Gutierrez, C., Sarkar, S., Geilert, S., Schmidt, M., Liebetrau, V., Kipfer, R., Scholz, F., Doll, M., Muff, S., Karstens, J., Planke, S., Petersen, S., Böttner, C., Chi, W.-C., Moser, M., Behrendt, R., Fiskal, A., Lever, M.A., Su, C.-C., Deng, L., Brennwald, M.S., and Lizarralde, D., 2016. Rifting under steam—how rift magmatism triggers methane venting from sedimentary basins. Geology, 44(9):767–770. **https://doi.org/10.1130/G38049.1**

Berndt, C., Mjelde, R., Planke, S., Shimamura, H., and Faleide, J.I., 2001a. Controls on the tectono-magmatic evolution of a volcanic transform margin: the Vøring transform margin, NE Atlantic. Marine Geophysical Research, 22:133–152. **https://doi.org/10.1023/A:1012089532282**

Berndt, C., Planke, S., Alvestad, E., Tsikalas, F., and Rasmussen, T., 2001b. Seismic volcanostratigraphy of the Norwegian Margin: constraints on tectonomagmatic break-up processes. Journal of the Geological Society (London, UK), 158(3):413–426. **https://doi.org/10.1144/jgs.158.3.413**

Berndt, C., Planke, S., Teagle, D., Huismans, R., Torsvik, T., Frieling, J., Jones, M.T., Jerram, D.A., Tegner, C., Faleide, J.I., Coxall, H., and Hong, W.-L., 2019. Northeast Atlantic breakup volcanism and consequences for Paleogene climate change – MagellanPlus Workshop report. Scientific Drilling, 26:69–85. **https://doi.org/10.5194/sd-26-69-2019**

Bijl, P.K., Bendle, J.A.P., Bohaty, S.M., Pross, J., Schouten, S., Tauxe, L., Stickley, C.E., McKay, R.M., Röhl, U., Olney, M., Sluijs, A., Escutia, C., and Brinkhuis, H., 2013. Eocene cooling linked to early flow across the Tasmanian Gateway. Proceedings of the National Academy of Sciences of the United States of America, 110(24):9645–9650. **https://doi.org/10.1073/pnas.1220872110**

Bijl, P.K., Frieling, J., Cramwinckel, M.J., Boschman, C., Sluijs, A., and Peterse, F., 2021. Maastrichtian–Rupelian paleoclimates in the southwest Pacific – a critical re-evaluation of biomarker paleothermometry and dinoflagellate cyst paleoecology at Ocean Drilling Program Site 1172. Climate of the Past, 17(6):2393–2425. **https://doi.org/10.5194/cp-17-2393-2021**

Bijl, P.K., Schouten, S., Sluijs, A., Reichart, G.-J., Zachos, J.C., and Brinkhuis, H., 2009. Early Palaeogene temperature evolution of the southwest Pacific Ocean. Nature, 461(7265):776–779. **https://doi.org/10.1038/nature08399**

Boldreel, L.O., and Andersen, M.S., 1994. Tertiary development of the Faroe-Rockall Plateau based on reflection seismic data. Bulletin of the Geological Society of Denmark, 41:162–180.

Bond, D.P.G., and Wignall, P.B., 2014. Large igneous provinces and mass extinctions: an update. In Keller, G., and Kerr, A.C. (Eds.), Volcanism, Impacts, and Mass Extinctions: Causes and Effects. Special Paper – Geological Society of America, 505. **https://doi.org/10.1130/2014.2505(02)**

Boutilier, R.R., and Keen, C.E., 1999. Small-scale convection and divergent plate boundaries. Journal of Geophysical Research: Solid Earth, 104(B4):7389–7403. **https://doi.org/10.1029/1998JB900076**

Bown, J.W., and White, R.S., 1994. Variation with spreading rate of oceanic crustal thickness and geochemistry. Earth and Planetary Science Letters, 121(3–4):435–449. **https://doi.org/10.1016/0012-821X(94)90082-5**

Breivik, A.J., Faleide, J.I., Mjelde, R., and Flueh, E.R., 2009. Magma productivity and early seafloor spreading rate correlation on the northern Vøring Margin, Norway — constraints on mantle melting. Tectonophysics, 468(1–4):206–223. **https://doi.org/10.1016/j.tecto.2008.09.020**

Breivik, A.J., Mjelde, R., Faleide, J.I., and Murai, Y., 2006. Rates of continental breakup magmatism and seafloor spreading in the Norway Basin–Iceland plume interaction. Journal of Geophysical Research: Solid Earth, 111(B7):B07102. **https://doi.org/10.1029/2005JB004004**

Brekke, H., 2000. The tectonic evolution of the Norwegian Sea Continental Margin with emphasis on the Vøring and Møre Basins. Geological Society Special Publication, 167(1):327–378. **https://doi.org/10.1144/gsl.Sp.2000.167.01.13**

Brinkhuis, H., Schouten, S., Collinson, M.E., Sluijs, A., Sinninghe Damsté, J.S., Dickens, G.R., Huber, M., Cronin, T.M., Onodera, J., Takahashi, K., Bujak, J.P., Stein, R., van der Burgh, J., Eldrett, J.S., Harding, I.C., Lotter, A.F., Sangiorgi, F., van Konijnenburg-van Cittert, H., de Leeuw, J.W., Matthiessen, J., Backman, J., and Moran, K., 2006. Episodic fresh surface waters in the Eocene Arctic Ocean. Nature, 441(7093):606–609. **https://doi.org/10.1038/nature04692**

Brown, E.L., and Lesher, C.E., 2014. North Atlantic magmatism controlled by temperature, mantle composition and buoyancy. Nature Geoscience, 7(11):820–824. **https://doi.org/10.1038/ngeo2264**

Bujak, J., and Mudge, D., 1994. A high-resolution North Sea Eocene dinocyst zonation. Journal of the Geological Society (London, UK), 151(3):449–462. **https://doi.org/10.1144/gsjgs.151.3.0449**

Bünz, S., and Shipboard Scientists, 2020. CAGE-20-4 cruise report. High-resolution 2D and 3D seismic investigations on the Møre and Vøring margins. UiT The Arctic University of Norway report, 47.

Champion, M.E.S., White, N.J., Jones, S.M., and Lovell, J.P.B., 2008. Quantifying transient mantle convective uplift: an example from the Faroe-Shetland Basin. Tectonics, 27(1):1–18. **https://doi.org/10.1029/2007TC002106**

Courtillot, V.E., and Renne, P.R., 2003. On the ages of flood basalt events. Comptes Rendus Geoscience, 335(1):113–140. **https://doi.org/10.1016/S1631-0713(03)00006-3**

Cramwinckel, M.J., Huber, M., Kocken, I.J., Agnini, C., Bijl, P.K., Bohaty, S.M., Frieling, J., Goldner, A., Hilgen, F.J., Kip, E.L., Peterse, F., van der Ploeg, R., Röhl, U., Schouten, S., and Sluijs, A., 2018. Synchronous tropical and polar temperature evolution in the Eocene. Nature, 559(7714):382–386. **https://doi.org/10.1038/s41586-018-0272-2**

Davison, I., Stasiuk, S., Nuttall, P., and Keane, P., 2010. Sub-basalt hydrocarbon prospectivity in the Rockall, Faroe–Shetland and Møre basins, NE Atlantic. Geological Society of London, Petroleum Geology Conference Series, 7(1):1025–1032. **https://doi.org/10.1144/0071025**

Dickens, G.R., 2011. Down the rabbit hole: toward appropriate discussion of methane release from gas hydrate systems during the Paleocene-Eocene Thermal Maximum and other past hyperthermal events. Climate of the Past, 7(3):831–846. **https://doi.org/10.5194/cp-7-831-2011**

Dickens, G.R., O'Neil, J.R., Rea, D.K., and Owen, R.M., 1995. Dissociation of oceanic methane hydrate as a cause of the carbon isotope excursion at the end of the Paleocene. Paleoceanography, 10(6):965–971. **https://doi.org/10.1029/95PA02087**

Duncan, R.A., Larsen, H.C., Allan, J.F., et al., 1996. Proceedings of the Ocean Drilling Program, Initial Reports, 163: College Station, TX (Ocean Drilling Program). **https://doi.org/10.2973/odp.proc.ir.163.1996**

Eldholm, O., Thiede, J., and Taylor, E., 1989. The Norwegian continental margin: tectonic, volcanic, and paleoenvironmental framework. In Eldholm, O., Thiede, J., Taylor, E., et al., Proceedings of the Ocean Drilling Program, Scientific Results. 104: College Station, TX (Ocean Drilling Program), 5–26. **https://doi.org/10.2973/odp.proc.sr.104.110.1989**

Eldholm, O., and Grue, K., 1994. North Atlantic volcanic margins: dimensions and production rates. Journal of Geophysical Research: Solid Earth, 99(B2):2955–2968. **https://doi.org/10.1029/93JB02879**

Eldholm, O., Thiede, J., and Taylor, E., 1987. Evolution of the Norwegian continental margin: background and objectives. In Eldholm, O., Thiede, J., and Taylor, E., et al., Proceedings of the Ocean Drilling Program, Initial Reports. 104: College Station, TX (Ocean Drilling Program), 5–26. **https://doi.org/10.2973/odp.proc.ir.104.101.1987**

Eldholm, O., and Thomas, E., 1993. Environmental impact of volcanic margin formation. Earth and Planetary Science Letters, 117(3–4):319–329. **https://doi.org/10.1016/0012-821X(93)90087-P**

Eldrett, J.S., and Harding, I.C., 2009. Palynological analyses of Eocene to Oligocene sediments from DSDP Site 338, Outer Vøring Plateau. Marine Micropaleontology, 73(3–4):226–240. **https://doi.org/10.1016/j.marmicro.2009.10.004**

Eldrett, J.S., Harding, I.C., Firth, J.V., and Roberts, A.P., 2004. Magnetostratigraphic calibration of Eocene–Oligocene dinoflagellate cyst biostratigraphy from the Norwegian–Greenland Sea. Marine Geology, 204(1–2):91–127. **https://doi.org/10.1016/S0025-3227(03)00357-8**

Elliott, G.M., and Parson, L.M., 2008. Influence of margin segmentation upon the break-up of the Hatton Bank rifted margin, NE Atlantic. Tectonophysics, 457(3):161–176. **https://doi.org/10.1016/j.tecto.2008.06.008**

Ernst, R.E., 2014. Large Igneous Provinces: Cambridge, United Kingdom (Cambridge University Press). **https://doi.org/10.1017/CBO9781139025300**

Ernst, R.E., and Youbi, N., 2017. How Large Igneous Provinces affect global climate, sometimes cause mass extinctions, and represent natural markers in the geological record. Palaeogeography, Palaeoclimatology, Palaeoecology, 478:30–52. **https://doi.org/10.1016/j.palaeo.2017.03.014**

Fitton, J.G., Larsen, L.M., Saunders, A.D., Hardarson, B.S., and Kempton, P.D., 2000. Palaeogene continental to oceanic magmatism on the SE Greenland continental margin at 63°N; a review of the results of Ocean Drilling Program Legs 152 and 163. Journal of Petrology, 41(7):951–966. **https://doi.org/10.1093/petrology/41.7.951**

Fitton, J.G., Saunders, A.D., Larsen, L.M., Hardarson, B.S., and Norry, M.J., 1998. Volcanic rocks from the southeast Greenland margin at 63°N: composition, petrogenesis, and mantle sources. In Saunders, A.D., Larsen, H.C., and Wise, S.W., Jr. (Eds.), Proceedings of the Ocean Drilling Program, Scientific Results. 152: College Station, TX (Ocean Drilling Program), 331–150. **https://doi.org/10.2973/odp.proc.sr.152.233.1998**

Foulger, G.R., Doré, T., Emeleus, C.H., Franke, D., Geoffroy, L., Gernigon, L., Hey, R., Holdsworth, R.E., Hole, M., Höskuldsson, Á., Julian, B., Kusznir, N., Martinez, F., McCaffrey, K.J.W., Natland, J.H., Peace, A.L., Petersen, K., Schiffer, C., Stephenson, R., and Stoker, M., 2020. The Iceland microcontinent and a continental Greenland-Iceland-Faroe Ridge. Earth-Science Reviews, 206:102926. **https://doi.org/10.1016/j.earscirev.2019.102926**

Fram, M.S., Lesher, C.E., and Volpe, A.M., 1998. Mantle melting systematics; transition from continental to oceanic volcanism on the Southeast Greenland margin. In Saunders, A.D., Larsen, H.C., and Wise, S.W., Jr. (Eds.), Proceedings of the Ocean Drilling Program, Scientific Results. 152: College Station, TX (Ocean Drilling Program), 373–386. **https://doi.org/10.2973/odp.proc.sr.152.236.1998**

Franke, D., Klitzke, P., Barckhausen, U., Berglar, K., Berndt, C., Damm, V., Dannowski, A., Ehrhardt, A., Engels, M., Funck, T., Geissler, W., Schnabel, M., Thorwart, M., and Trinhammer, P., 2019. Polyphase magmatism during the formation of the northern East Greenland continental margin. Tectonics, 38(8):2961–2982. **https://doi.org/10.1029/2019TC005552**

Frieling, J., Svensen, H.H., Planke, S., Cramwinckel, M.J., Selnes, H., and Sluijs, A., 2016. Thermogenic methane release as a cause for the long duration of the PETM. Proceedings of the National Academy of Sciences of the United States of America, 113(43):12059–12064. **https://doi.org/10.1073/pnas.1603348113**

Frost, B.R., Barnes, C.G., Colins, W.J., Arculus, R.J., Ellis, D.J., and Frost, C.D., 2001. A geochemical classification for granitic rocks. Journal of Petrology, 42(11):2033–2048. **https://doi.org/10.1093/petrology/42.11.2033**

Geissler, W.H., Gaina, C., Hopper, J.R., Funck, T., Blischke, A., Arting, U., Horni, J.A., Péron-Pinvidic, G., and Abdelmalak, M.M., 2016. Seismic volcanostratigraphy of the NE Greenland continental margin. Geological Society of London Collection. **https://doi.org/10.6084/m9.figshare.c.3593780**

Gernigon, L., Blischke, A., Nasuti, A., and Sand, M., 2015. Conjugate volcanic rifted margins, seafloor spreading, and microcontinent: Insights from new high-resolution aeromagnetic surveys in the Norway Basin. Tectonics, 34(5):907–933. **https://doi.org/10.1002/2014TC003717**

Gernigon, L., Franke, D., Geoffroy, L., Schiffer, C., Foulger, G.R., and Stoker, M., 2020. Crustal fragmentation, magmatism, and the diachronous opening of the Norwegian-Greenland Sea. Earth-Science Reviews, 206:102839. **https://doi.org/10.1016/j.earscirev.2019.04.011**

Gernigon, L., Ringenbach, J.C., Planke, S., Gall, B.L., and Jonquet-Kolstø, H., 2003. Extension, crustal structure and magmatism at the outer Vøring Basin, Norwegian margin. Journal of the Geological Society (London, UK), 160(2):197–208. **https://doi.org/10.1144/0016-764902-055**

Gernigon, L., Zastrozhnov, D., Planke, S., Manton, B., Abdelmalak, M.M., Olesen, O., Maharjan, D., Faleide, J.I., and Myklebust, R., 2021. A digital compilation of structural and magmatic elements of the mid-Norwegian continental margin. Norwegian Journal of Geology, 101. **https://doi.org/10.17850/njg101-3-2**

Gutjahr, M., Ridgwell, A., Sexton, P.F., Anagnostou, E., Pearson, P.N., Pälike, H., Norris, R.D., Thomas, E., and Foster, G.L., 2017. Very large release of mostly volcanic carbon during the Palaeocene-Eocene Thermal Maximum. Nature, 548(7669):573–577. **https://doi.org/10.1038/nature23646**

Hartley, R.A., Roberts, G.G., White, N., and Richardson, C., 2011. Transient convective uplift of an ancient buried landscape. Nature Geoscience, 4(8):562–565. **https://doi.org/10.1038/ngeo1191**

Heilmann-Clausen, C., and Van Simaeys, S., 2005. Dinoflagellate cysts from the middle Eocene to ?lowermost Oligocene succession in the Kysing research borehole, central Danish basin. Palynology, 29(1):143–204. **https://doi.org/10.1080/01916122.2005.9989606**

Hinz, K., 1981. A hypothesis on terrestrial catastrophes wedges of very thick oceanward dipping layers beneath passive continental margins; their origin and paleoenvironmental significance. Geologisches Jahrbuch, Reihe E: Geophysik, 22:3–28.

Hinz, K., and Weber, J., 1976. Zum geologischen aufbau des Norwegischen kontinentalrandes und der Barents-See nach reflexionsseismischen Messungen. Erdöl und Kohle, Erdgas, Petrochemie, 3-29.

Holbrook, W.S., Larsen, H.C., Korenaga, J., Dahl-Jensen, T., Reid, I.D., Kelemen, P.B., Hopper, J.R., Kent, G.M., Lizarralde, D., Bernstein, S., and Detrick, R.S., 2001. Mantle thermal structure and active upwelling during continental breakup in the North Atlantic. Earth and Planetary Science Letters, 190(3):251–266. **https://doi.org/10.1016/S0012-821X(01)00392-2**

Hole, M.J., and Millett, J.M., 2016. Controls of mantle potential temperature and lithospheric thickness on magmatism in the North Atlantic igneous province. Journal of Petrology, 57(2):417–436. **https://doi.org/10.1093/petrology/egw014**

Hole, M.J., and Natland, J.H., 2020. Magmatism in the North Atlantic igneous province; mantle temperatures, rifting and geodynamics. Earth-Science Reviews, 206:102794. **https://doi.org/10.1016/j.earscirev.2019.02.011**

Hollis, C.J., Taylor, K.W.R., Handley, L., Pancost, R.D., Huber, M., Creech, J.B., Hines, B.R., Crouch, E.M., Morgans, H.E.G., Crampton, J.S., Gibbs, S., Pearson, P.N., and Zachos, J.C., 2012. Early Paleogene temperature history of the Southwest Pacific Ocean: reconciling proxies and models. Earth and Planetary Science Letters, 349–350:53–66. **https://doi.org/10.1016/j.epsl.2012.06.024**

Horni, J.Á., Hopper, J.R., Blischke, A., Geisler, W.H., Stewart, M., McDermott, K., Judge, M., Erlendsson, Ö., and Árting, U., 2017. Regional distribution of volcanism within the North Atlantic Igneous Province. Geological Society Special Publications, 447(1):105–125. **https://doi.org/10.1144/SP447.18**

Huismans, R., and Beaumont, C., 2011. Depth-dependent extension, two-stage breakup and cratonic underplating at rifted margins. Nature, 473(7345):74–78. **https://doi.org/10.1038/nature09988**

Huismans, R.S., and Beaumont, C., 2014. Rifted continental margins: the case for depth-dependent extension. Earth and Planetary Science Letters, 407:148–162. **https://doi.org/10.1016/j.epsl.2014.09.032**

Inagaki, F., Hinrichs, K.U., Kubo, Y., Bowles, M.W., Heuer, V.B., Hong, W.L., Hoshino, T., Ijiri, A., Imachi, H., Ito, M., Kaneko, M., Lever, M.A., Lin, Y.S., Methé, B.A., Morita, S., Morono, Y., Tanikawa, W., Bihan, M., Bowden, S.A., Elvert, M., Glombitza, C., Gross, D., Harrington, G.J., Hori, T., Li, K., Limmer, D., Liu, C.H., Murayama, M., Ohkouchi, N., Ono, S., Park, Y.S., Phillips, S.C., Prieto-Mollar, X., Purkey, M., Riedinger, N., Sanada, Y., Sauvage, J., Snyder, G., Susilawati, R., Takano, Y., Tasumi, E., Terada, T., Tomaru, H., Trembath-Reichert, E., Wang, D.T., and Yamada, Y., 2015. Exploring deep microbial life in coal-bearing sediment down to ~2.5 km below the ocean floor. Science, 349(6246):420–424. **https://doi.org/10.1126/science.aaa6882**

Jamtveit, B., Svensen, H., Podladchikov, Y.Y., and Planke, S., 2004. Hydrothermal vent complexes associated with sill intrusions in sedimentary basins. In Breitkreuz, C., and Petford, N. (Eds.), Physical Geology of High-Level Magmatic Systems. Geological Society Special Publication, 234: 233–241. **https://doi.org/10.1144/GSL.SP.2004.234.01.15**

Jones, M.T., Jerram, D.A., Svensen, H.H., and Grove, C., 2016. The effects of large igneous provinces on the global carbon and sulphur cycles. Palaeogeography, Palaeoclimatology, Palaeoecology, 441:4–21. **https://doi.org/10.1016/j.palaeo.2015.06.042**

Kjoberg, S., Schmidedel, T., Planke, S., Svensen, H.H., Millett, J.M., Jerram, D.A., Galland, O., Lecomte, I., Scnhofield, N., Haug, Ø.T., and Helsem, A., 2017. 3D structure and formation of hydrothermal vent complexes at the Paleocene-Eocene transition, the Møre Basin, mid-Norwegian margin. Interpretation, 5(3):1A–T449. **https://doi.org/10.1190/INT-2016-0159.1**

Koch, S., Berndt, C., Bialas, J., Haeckel, M., Crutchley, G., Papenberg, C., Klaeschen, D., and Greinert, J., 2015. Gas-controlled seafloor doming. Geology, 43(7):571–574. **https://doi.org/10.1130/G36596.1**

Kokelaar, B.P., 1983. The mechanism of Surtseyan volcanism. Journal of the Geological Society (London, UK), 140(6):939–944. **https://doi.org/10.1144/gsjgs.140.6.0939**

Köthe, A., Gaedicke, C., and Lutz, R., 2008. Erratum: the age of the Mid-Miocene Unconformity (MMU) in the G-11-1 borehole, German North Sea sector. Zeitschrift der Deutschen Gesellschaft für Geowissenschaften, 159(4):687–689. **https://doi.org/10.1127/1860-1804/2008/0159-0687**

Kusznir, N.J., Hunsdale, R., and Roberts, A.M., 2004. Timing of depth-dependent lithosphere stretching on the S. Lofoten rifted margin offshore mid-Norway: pre-breakup or post-breakup? Basin Research, 16(2):279–296. **https://doi.org/10.1111/j.1365-2117.2004.00233.x**

Larsen, H.C., Saunders, A.D., Clift, P.D., et al., 1994. Proceedings of the Ocean Drilling Program, Initial Reports, 152: College Station, TX (Ocean Drilling Program). **https://doi.org/10.2973/odp.proc.ir.152.1994**

Larsen, H.C., and Saunders, A.D., 1998. Tectonism and volcanism at the Southeast Greenland rifted margin: a record of plume impact and later continental rupture. In Saunders, A.D., Larsen, H.C., and Wise, S.W., Jr. (Eds.), Proceedings of the Ocean Drilling Program, Scientific Results. 152: 503–533. **https://doi.org/10.2973/odp.proc.sr.152.240.1998**

Larsen, L.M., Rex, D.C., Watt, W.S., and Guise, P.G., 1999. ^{40}Ar–^{39}Ar dating of alkali basaltic dykes along the southwest coast of Greenland: Cretaceous and Tertiary igneous activity along the eastern margin of the Labrador Sea. Geology of Greenland Survey Bulletin, 184:19–29. **https://doi.org/10.34194/ggub.v184.5227**

Lazarus, D., Barron, J., Renaudie, J., Diver, P., and Türke, A., 2014. Cenozoic planktonic marine diatom diversity and correlation to climate change. PloS One, 9(1):e84857. **https://doi.org/10.1371/journal.pone.0084857**

Leifer, I., and Judd, A., 2015. The UK22/4b blowout 20 years on: investigations of continuing methane emissions from sub-seabed to the atmosphere in a North Sea context. Marine and Petroleum Geology, 68:706–717. **https://doi.org/10.1016/j.marpetgeo.2015.11.012**

Lorenzo, J.M., and Wessel, P., 1997. Flexure across a continent–ocean fracture zone: the northern Falkland/Malvinas Plateau, South Atlantic. Geo-Marine Letters, 17(1):110–118. **https://doi.org/10.1007/s003670050015**

Lu, G., and Huismans, R.S., 2021. Melt volume at Atlantic volcanic rifted margins controlled by depth-dependent extension and mantle temperature. Nature Communications, 12(1):3894. **https://doi.org/10.1038/s41467-021-23981-5**

Lundin, E.R., and Doré, A.G., 2005. NE Atlantic break-up: a re-examination of the Iceland mantle plume model and the Atlantic–Arctic linkage. Geological Society of London, Petroleum Geology Conference Series, 6(1):739–754. **https://doi.org/10.1144/0060739**

Mahoney, J.J., and Coffin, M.F. (Eds.), 1997. Large Igneous Provinces: Continental, Oceanic, and Planetary Flood Volcanism. Geophysical Monograph, 100. **https://doi.org/10.1029/GM100**

Manton, B., 2015. The mechanics of sill propagation and associated venting investigated using 3D seismic data from offshore Norway [PhD dissertation]. Cardiff University, Cardiff, England. **http://orca.cardiff.ac.uk/id/eprint/75498**

Matter, J.M., Stute, M., Snæbjörnsdottir, S.Ó., Oelkers, E.H., Gislason, S.R., Aradottir, E.S., Sigfusson, B., Gunnarsson, I., Sigurdardottir, H., Gunnlaugsson, E., Axelsson, H.A., Woff-Boenisch, D., Mesfin, K., de la Reguera Taaya, D.F., Hall, J., Diderikson, K., and Broecker, W.S., 2016. Rapid carbon mineralization for permanent disposal of anthropogenic carbon dioxide emissions. Science, 352(6291):1312–1314. **https://doi.org/10.1126/science.aad8132**

Mazzini, A., Svensen, H., Akhmanov, G.G., Aloisi, G., Planke, S., Malthe-Sørenssen, A., and Istadi, B., 2007. Triggering and dynamic evolution of the LUSI mud volcano, Indonesia. Earth and Planetary Science Letters, 261(3):375–388. **https://doi.org/10.1016/j.epsl.2007.07.001**

McGrail, B.P., Spane, F.A., Sullivan, E.C., Bacon, D.H., and Hund, G., 2011. The Wallula basalt sequestration pilot project. Energy Procedia, 4:5653–5660. **https://doi.org/10.1016/j.egypro.2011.02.557**

McKenzie, D., and Bickle, M.J., 1988. The volume and composition of melt generated by extension of the lithosphere. Journal of Petrology, 29(3):625–679. **https://doi.org/10.1093/petrology/29.3.625**

Mercier de Lépinay, M., Loncke, L., Basile, C., Roest, W.R., Patriat, M., Maillard, A., and De Clarens, P., 2016. Transform continental margins – Part 2: A worldwide review. Tectonophysics, 693:96–115. **https://doi.org/10.1016/j.tecto.2016.05.038**

Meyer, R., Hertogen, J., Pedersen, R.B., Viereck-Götte, L., and Abratis, M., 2009. Interaction of mantle derived melts with crust during the emplacement of the Vøring Plateau, N.E. Atlantic. Marine Geology, 261(1–4):3–16. **https://doi.org/10.1016/j.margeo.2009.02.007**

Millett, J.M., Hole, M.J., Jolley, D.W., Passey, S.R., and Rossetti, L., 2020. Transient mantle cooling linked to regional volcanic shut-down and early rifting in the North Atlantic Igneous Province. Bulletin of Volcanology, 82(8):61. **https://doi.org/10.1007/s00445-020-01401-8**

Millett, J.M., Manton, B.M., Zastrozhnov, D., Planke, S., Maharjan, D., Bellwald, B., Gernigon, L., Faleide, J.I., Jolley, D.W., Walker, F., Abdelmalak, M.M., Jerram, D.A., Myklebust, R., Kjølhamar, B.E., Halliday, J., and Birch-Hawkins, A., 2022. Basin structure and prospectivity of the NE Atlantic volcanic rifted margin: cross-border examples from the Faroe–Shetland, Møre and Southern Vøring Basins. In Krmíček, L., and Chalapathi Rao, N.V. (Eds.), Lamprophyres, Lamproites and Related Rocks: Tracers to Supercontinent Cycles and Metallogenesis. Geological Society Special Publication, 495. **https://doi.org/10.1144/sp495-2019-12**

Mjelde, R., Raum, T., Breivik, A., Shimamura, H., Murai, Y., Takanami, T., and Faleide, J.I., 2005. Crustal structure of the Vøring margin, NE Atlantic: a review of geological implications based on recent OBS data. Geological Society of London, Petroleum Geology Conference Series, 6(1):803–813. **https://doi.org/10.1144/0060803**

Mjelde, R., Raum, T., Kandilarov, A., Murai, Y., and Takanami, T., 2009. Crustal structure and evolution of the outer Møre Margin, NE Atlantic. Tectonophysics, 468(1):224–243. **https://doi.org/10.1016/j.tecto.2008.06.003**

Mutter, J.C., Buck, W.R., and Zehnder, C.M., 1988. Convective partial melting: 1. A model for the formation of thick basaltic sequences during the initiation of spreading. Journal of Geophysical Research: Solid Earth, 93(B2):1031–1048. **https://doi.org/10.1029/JB093iB02p01031**

Ogg, J.G., 2012. Geomagnetic Polarity Time Scale. In Gradstein, F.M., Ogg, J.G., Schmitz, M.D. and Ogg, G.M., The Geologic Time Scale. Boston (Elsevier), 85–113. **https://doi.org/10.1016/B978-0-444-59425-9.00005-6**

Omosanya, K.O., Eruteya, O.E., Siregar, E.S.A., Zieba, K.J., Johansen, S.E., Alves, T.M., and Waldmann, N.D., 2018. Three-dimensional (3-D) seismic imaging of conduits and radial faults associated with hydrothermal vent complexes (Vøring Basin, offshore Norway). Marine Geology, 399:115–134. **https://doi.org/10.1016/j.margeo.2018.02.007**

Pagani, M., Pedentchouk, N., Huber, M., Sluijs, A., Schouten, S., Brinkhuis, H., Sinninghe Damsté, J.S., Dickens, G.R., and the Expedition 302 Scientists, 2006. Arctic hydrology during global warming at the Palaeocene/Eocene Thermal Maximum. Nature, 442(7103):671–675. **https://doi.org/10.1038/nature05043**

Parnell-Turner, R., Cann, J.R., Smith, D.K., Schouten, H., Yoerger, D., Palmiotto, C., Zheleznov, A., and Bai, H., 2014. Sedimentation rates test models of oceanic detachment faulting. Geophysical Research Letters, 41(20):7080–7088. **https://doi.org/10.1002/2014GL061555**

Perez-Garcia, C., Feseker, T., Mienert, J., and Berndt, C., 2009. The Håkon Mosby mud volcano: 330,000 years of focused fluid flow activity at the SW Barents Sea slope. Marine Geology, 262(1–4):105–115. **https://doi.org/10.1016/j.margeo.2009.03.022**

Planke, S., 1994. Geophysical response of flood basalts from analysis of wire line logs; Ocean Drilling Program Site 642, Vøring volcanic margin. Journal of Geophysical Research: Solid Earth, 99(B5):9279–9296. **https://doi.org/10.1029/94JB00496**

Planke, S., Bellwald, B., Millett, J., Planke, E.E.E., Zastrozhnov, D., Carlevaris, P., Rosenqvist, M., Jerram, D.A., Schmid, D., Berndt, C., Kjølhamar, B., and Myklebust, R., 2021. Permanent carbon sequestration potential in offshore basalt sequences on the NW European continental margins. Conference Proceedings, 82nd EAGE Annual Conference & Exhibition, 2021:1–5. **https://doi.org/10.3997/2214-4609.202011841**

Planke, S., Berndt, C., Alvarez Zarikian, C.A., Agarwal, A., Andrews, G.D.M., Betlem, P., Bhattacharya, J., Brinkhuis, H., Chatterjee, S., Christopoulou, M., Clementi, V.J., Ferré, E.C., Filina, I.Y., Frieling, J., Guo, P., Harper, D.T., Jones, M.T., Lambart, S., Longman, J., Millett, J.M., Mohn, G., Nakaoka, R., Scherer, R.P., Tegner, C., Varela, N., Wang, M., Xu, W., and Yager, S.L., 2023a. Site U1565. In Planke, S., Berndt, C., Alvarez Zarikian, C.A., and the Expedition 396 Scientists, Mid-Norwegian Margin Magmatism and Paleoclimate Implications. Proceedings of the International Ocean Discovery Program, 396: College Station, TX (International Ocean Discovery Program). **https://doi.org/10.14379/iodp.proc.396.103.2023**

Planke, S., Berndt, C., Alvarez Zarikian, C.A., Agarwal, A., Andrews, G.D.M., Betlem, P., Bhattacharya, J., Brinkhuis, H., Chatterjee, S., Christopoulou, M., Clementi, V.J., Ferré, E.C., Filina, I.Y., Frieling, J., Guo, P., Harper, D.T., Jones, M.T., Lambart, S., Longman, J., Millett, J.M., Mohn, G., Nakaoka, R., Scherer, R.P., Tegner, C., Varela, N., Wang, M., Xu, W., and Yager, S.L., 2023b. Site U1573. In Planke, S., Berndt, C., Alvarez Zarikian, C.A., and the Expedition 396 Scientists, Mid-Norwegian Margin Magmatism and Paleoclimate Implications. Proceedings of the International Ocean Discovery Program, 396: College Station, TX (International Ocean Discovery Program). **https://doi.org/10.14379/iodp.proc.396.108.2023**

Planke, S., Berndt, C., Alvarez Zarikian, C.A., Agarwal, A., Andrews, G.D.M., Betlem, P., Bhattacharya, J., Brinkhuis, H., Chatterjee, S., Christopoulou, M., Clementi, V.J., Ferré, E.C., Filina, I.Y., Frieling, J., Guo, P., Harper, D.T., Jones, M.T., Lambart, S., Longman, J., Millett, J.M., Mohn, G., Nakaoka, R., Scherer, R.P., Tegner, C., Varela, N., Wang, M., Xu, W., and Yager, S.L., 2023c. Site U1574. In Planke, S., Berndt, C., Alvarez Zarikian, C.A., and the Expedition 396 Scientists, Mid-Norwegian Margin Magmatism and Paleoclimate Implications. Proceedings of the International Ocean Discovery Program, 396: College Station, TX (International Ocean Discovery Program). **https://doi.org/10.14379/iodp.proc.396.109.2023**

Planke, S., Berndt, C., Alvarez Zarikian, C.A., Agarwal, A., Andrews, G.D.M., Betlem, P., Bhattacharya, J., Brinkhuis, H., Chatterjee, S., Christopoulou, M., Clementi, V.J., Ferré, E.C., Filina, I.Y., Frieling, J., Guo, P., Harper, D.T., Jones, M.T., Lambart, S., Longman, J., Millett, J.M., Mohn, G., Nakaoka, R., Scherer, R.P., Tegner, C., Varela, N., Wang, M., Xu, W., and Yager, S.L., 2023d. Sites U1567 and U1568. In Planke, S., Berndt, C., Alvarez Zarikian, C.A., and the Expedition 396 Scientists, Mid-Norwegian Margin Magmatism and Paleoclimate Implications. Proceedings of the International Ocean Discovery Program, 396: College Station, TX (International Ocean Discovery Program). **https://doi.org/10.14379/iodp.proc.396.105.2023**

Planke, S., Berndt, C., Alvarez Zarikian, C.A., Agarwal, A., Andrews, G.D.M., Betlem, P., Bhattacharya, J., Brinkhuis, H., Chatterjee, S., Christopoulou, M., Clementi, V.J., Ferré, E.C., Filina, I.Y., Frieling, J., Guo, P., Harper, D.T., Jones, M.T., Lambart, S., Longman, J., Millett, J.M., Mohn, G., Nakaoka, R., Scherer, R.P., Tegner, C., Varela, N., Wang, M., Xu, W., and Yager, S.L., 2023e. Sites U1569 and U1570. In Planke, S., Berndt, C., Alvarez Zarikian, C.A., and the Expedition 396 Scientists, Mid-Norwegian Margin Magmatism and Paleoclimate Implications. Proceedings of the International Ocean Discovery Program, 396: College Station, TX (International Ocean Discovery Program). **https://doi.org/10.14379/iodp.proc.396.106.2023**

Planke, S., Berndt, C., Alvarez Zarikian, C.A., Agarwal, A., Andrews, G.D.M., Betlem, P., Bhattacharya, J., Brinkhuis, H., Chatterjee, S., Christopoulou, M., Clementi, V.J., Ferré, E.C., Filina, I.Y., Frieling, J., Guo, P., Harper, D.T., Jones, M.T., Lambart, S., Longman, J., Millett, J.M., Mohn, G., Nakaoka, R., Scherer, R.P., Tegner, C., Varela, N., Wang, M., Xu, W., and Yager, S.L., 2023f. Sites U1571 and U1572. In Planke, S., Berndt, C., Alvarez Zarikian, C.A., and the Expedition 396 Scientists, Mid-Norwegian Margin Magmatism and Paleoclimate Implications. Proceedings of the International Ocean Discovery Program, 396: College Station, TX (International Ocean Discovery Program). **https://doi.org/10.14379/iodp.proc.396.107.2023**

Planke, S., Millett, J.M., Maharjan, D., Jerram, D.A., Mansour Abdelmalak, M., Groth, A., Hoffmann, J., Berndt, C., and Myklebust, R., 2017. Igneous seismic geomorphology of buried lava fields and coastal escarpments on the Vøring volcanic rifted margin. Interpretation, 5(3):SK161–SK177. **https://doi.org/10.1190/INT-2016-0164.1**

Planke, S., Rasmussen, T., Rey, S.S., and Myklebust, R., 2005. Seismic characteristics and distribution of volcanic intrusions and hydrothermal vent complexes in the Vøring and Møre Basins. Geological Society of London, Petroleum Geology Conference Series, 6(1):833–844. **https://doi.org/10.1144/0060833**

Planke, S., Symonds, P.A., Alvestad, E., and Skogseid, J., 2000. Seismic volcanostratigraphy of large-volume basaltic extrusive complexes on rifted margins. Journal of Geophysical Research: Solid Earth, 105(B8):19335–19351. **https://doi.org/10.1029/1999JB900005**

Polteau, S., Planke, S., Zastrozhnov, D., Abdelmalak, M.M., Lebedeva-Ivanova, N., Planke, E.E., Svensen, H.H., Mazzini, A., Gernigon, L., Myklebust, R., Kjølhamar, B.E., Pedersen, R.B., Sandstå, N.R., and Bünz, S., 2020. Upper Cretaceous-Paleogene stratigraphy and development of the Mímir high, Vøring transform margin, Norwegian Sea. Marine and Petroleum Geology, 122:104717. **https://doi.org/10.1016/j.marpetgeo.2020.104717**

Reynolds, P., Planke, S., Millett, J.M., Jerram, D.A., Trulsvik, M., Schofield, N., and Myklebust, R., 2017. Hydrothermal vent complexes offshore northeast Greenland: a potential role in driving the PETM. Earth and Planetary Science Letters, 467:72–78. **https://doi.org/10.1016/j.epsl.2017.03.031**

Rickwood, P.C., 1989. Boundary lines within petrologic diagrams which use oxides of major and minor elements. Lithos, 22(4):247–263. **https://doi.org/10.1016/0024-4937(89)90028-5**

Ritchie, J.D., Gatliff, R.W., and Richards, P.C., 1999. Early Tertiary magmatism in the offshore NW UK margin and surrounds. In Fleet, A.J., and Boldy, S.A.R. (Eds.), Petroleum Geology of Northwest Europe: Proceedings of the 5th Conference. Petroleum Geology Conference Series, 5: 573–584. **https://doi.org/10.1144/0050573**

Roelofse, C., Alves, T.M., and Omosanya, K.d.O., 2021. Reutilisation of hydrothermal vent complexes for focused fluid flow on continental margins (Modgunn Arch, Norwegian Sea). Basin Research, 33(2):1111–1134. **https://doi.org/10.1111/bre.12507**

Saunders, A.D., Jones, S.M., Morgan, L.A., Pierce, K.L., Widdowson, M., and Xu, Y.G., 2007. Regional uplift associated with continental large igneous provinces: the roles of mantle plumes and the lithosphere. Chemical Geology, 241(3–4):282–318. **https://doi.org/10.1016/j.chemgeo.2007.01.017**

Saunders, A.D., Larsen, H.C., and Fitton, J.G., 1998. Magmatic development of the Southeast Greenland margin and evolution of the Iceland plume; geochemical constraints from Leg 152. In Saunders, A.D., Larsen, H.C. and Wise, S.W., Jr., Proceedings of the Ocean Drilling Program, Scientific Results. 152: College Station, TX (Ocean Drilling Program), 479–501. **https://doi.org/10.2973/odp.proc.sr.152.239.1998**

Sengör, A.M.C., and Burke, K., 1978. Relative timing of rifting and volcanism on Earth and its tectonic implications. Geophysical Research Letters, 5(6):419–421. **https://doi.org/10.1029/GL005i006p00419**

Skogseid, J., and Eldholm, O., 1989. Vøring Plateau continental margin: seismic interpretation, stratigraphy, and vertical movements. In Eldholm, O., Thiede, J., Taylor, E., et al., Proceedings of the Ocean Drilling Program, Scientific Results. 104: College Station, TX (Ocean Drilling Program), 993–1030. **https://doi.org/10.2973/odp.proc.sr.104.151.1989**

Skogseid, J., and Eldholm, O., 1987. Early Cenozoic crust at the Norwegian continental margin and the conjugate Jan Mayen Ridge. Journal of Geophysical Research: Solid Earth, 92(B11):11471–11491. **https://doi.org/10.1029/JB092iB11p11471**

Skogseid, J., Planke, S., Faleide, J.I., Pedersen, T., Eldholm, O., and Neverdal, F., 2000. NE Atlantic continental rifting and volcanic margin formation. Geological Society Special Publication, 167(1):295–326. **https://doi.org/10.1144/GSL.SP.2000.167.01.12**

Spiegler, D., and Jansen, E., 1989. Planktonic foraminifer biostratigraphy of Norwegian Sea sediments: ODP Leg 104. In Eldholm, O., Thiede, J., Taylor, E., et al., Proceedings of the Ocean Drilling Program, Scientific Results. 104: College Station, TX (Ocean Drilling Program), 681–696. **https://doi.org/10.2973/odp.proc.sr.104.157.1989**

Storey, M., Duncan, R.A., and Swisher, C.C., III, 2007a. Paleocene-Eocene Thermal Maximum and the opening of the northeast Atlantic. Science, 316(5824):587–589. **https://doi.org/10.1126/science.1135274**

Storey, M., Duncan, R.A., and Tegner, C., 2007b. Timing and duration of volcanism in the North Atlantic Igneous Province: implications for geodynamics and links to the Iceland hotspot. Chemical Geology, 241(3):264–281. **https://doi.org/10.1016/j.chemgeo.2007.01.016**

Suan, G., Popescu, S.-M., Suc, J.-P., Schnyder, J., Fauquette, S., Baudin, F., Yoon, D., Piepjohn, K., Sobolev, N.N., and Labrousse, L., 2017. Subtropical climate conditions and mangrove growth in Arctic Siberia during the early Eocene. Geology, 45(6):539–542. **https://doi.org/10.1130/G38547.1**

Svensen, H., Jamtveit, B., Planke, S., and Chevallier, L., 2006. Structure and evolution of hydrothermal vent complexes in the Karoo Basin, South Africa. Journal of the Geological Society (London, UK), 163(4):671–682. **https://doi.org/10.1144/1144-764905-037**

Svensen, H., Planke, S., Jamtveit, B., and Pedersen, T., 2003. Seep carbonate formation controlled by hydrothermal vent complexes: a case study from the Vøring Basin, the Norwegian Sea. Geo-Marine Letters, 23(3):351–358. **https://doi.org/10.1007/s00367-003-0141-2**

Svensen, H., Planke, S., Malthe-Sørenssen, A., Jamtveit, B., Myklebust, R., Rasmussen Eidem, T., and Rey, S.S., 2004. Release of methane from a volcanic basin as a mechanism for initial Eocene global warming. Nature, 429(6991):542–545. **https://doi.org/10.1038/nature02566**

Svensen, H., Planke, S., Polozov, A.G., Schmidbauer, N., Corfu, F., Podladchikov, Y.Y., and Jamtveit, B., 2009. Siberian gas venting and the end-Permian environmental crisis. Earth and Planetary Science Letters, 277(3–4):490–500. **https://doi.org/10.1016/j.epsl.2008.11.015**

Svensen, H.H., Iyer, K., Schmid, D.W., and Mazzini, A., 2018. Modelling of gas generation following emplacement of an igneous sill below Lusi, East Java, Indonesia. Marine and Petroleum Geology, 90:201–208. **https://doi.org/10.1016/j.marpetgeo.2017.07.007**

Svensen, H.H., Jerram, D.A., Polozov, A.G., Planke, S., Neal, C.R., Augland, L.E., and Emeleus, H.C., 2019. Thinking about LIPs: a brief history of ideas in large igneous province research. Tectonophysics, 760:229–251. **https://doi.org/10.1016/j.tecto.2018.12.008**

Talwani, M., Udintsev, G., et al., 1976. Initial Reports of the Deep Sea Drilling Project, 38: Washington, DC (US Government Printing Office). **https://doi.org/10.2973/dsdp.proc.38.1976**

Talwani, M., and Eldholm, O., 1977. Evolution of the Norwegian-Greenland Sea. Geological Society of America Bulletin, 88(7):969–999. **https://doi.org/10.1130/0016-7606(1977)88%3C969:EOTNS%3E2.0.CO;2**

Tegner, C., Lesher, C.E., Larsen, L.M., and Watt, W.S., 1998. Evidence from the rare-earth-element record of mantle melting for cooling of the Tertiary Iceland plume. Nature, 395(6702):591–594. **https://doi.org/10.1038/26956**

Thatje, S., Gerdes, D., and Rachor, E., 1999. A seafloor crater in the German Bight and its effects on the benthos. Helgoland Marine Research, 53(1):36–44. **https://doi.org/10.1007/PL00012136**

Theissen-Krah, S., Zastrozhnov, D., Abdelmalak, M.M., Schmid, D.W., Faleide, J.I., and Gernigon, L., 2017. Tectonic evolution and extension at the Møre margin – offshore mid-Norway. Tectonophysics, 721:227–238. **https://doi.org/10.1016/j.tecto.2017.09.009**

Tsikalas, F., Faleide, J.I., and Kusznir, N.J., 2008. Along-strike variations in rifted margin crustal architecture and lithosphere thinning between northern Vøring and Lofoten margin segments off mid-Norway. Tectonophysics, 458(1–4):68–81. **https://doi.org/10.1016/j.tecto.2008.03.001**

Tsikalas, F., Inge Faleide, J., and Eldholm, O., 2001. Lateral variations in tectono-magmatic style along the Lofoten–Vesterålen volcanic margin off Norway. Marine and Petroleum Geology, 18(7):807–832. **https://doi.org/10.1016/S0264-8172(01)00030-7**

Vågnes, E., 1997. Uplift at thermo-mechanically coupled ocean–continent transforms: Modeled at the Senja Fracture Zone, southwestern Barents Sea. Geo-Marine Letters, 17(1):100–109. **https://doi.org/10.1007/s003670050014**

Vogt, P.R., 1972. Evidence for global synchronism in mantle plume convection, and possible significance for geology. Nature, 240(5380):338–342. **https://doi.org/10.1038/240338a0**

Wade, B.S., Pearson, P.N., Berggren, W.A., and Pälike, H., 2011. Review and revision of Cenozoic tropical planktonic foraminiferal biostratigraphy and calibration to the geomagnetic polarity and astronomical time scale. Earth-Science Reviews, 104(1–3):111–142. **https://doi.org/10.1016/j.earscirev.2010.09.003**

Westerhold, T., Röhl, U., Donner, B., Frederichs, T., Kordesch, W.E.C., Bohaty, S.M., Hodell, D.A., Laskar, J., and Zeebe, R.E., 2018. Late Lutetian Thermal Maximum—crossing a thermal threshold in Earth's climate system? Geochemistry, Geophysics, Geosystems, 19(1):73–82. **https://doi.org/10.1002/2017GC007240**

White, R., and McKenzie, D., 1989. Magmatism at rift zones: the generation of volcanic continental margins and flood basalts. Journal of Geophysical Research: Solid Earth, 94(B6):7685–7729. **https://doi.org/10.1029/JB094iB06p07685**

Wignall, P.B., 2001. Large igneous provinces and mass extinctions. Earth-Science Reviews, 53(1):1–33. **https://doi.org/10.1016/S0012-8252(00)00037-4**

Wilkinson, C.M., Ganerød, M., Hendriks, B.W.H., and Eide, E.A., 2017. Compilation and appraisal of geochronological data from the North Atlantic Igneous Province (NAIP). Geological Society Special Publications, 447(1):69–103. **https://doi.org/10.1144/sp447.10**

Williams, G.L., Stover, L.E., and Kidson, E.J., 1993. Morphology and stratigraphic ranges of selected Mesozoic-Cenozoic dinoflagellate taxa in the Northern Hemisphere. Geology. **https://doi.org/10.4095/183916**

Wright, K.A., Davies, R.J., Jerram, D.A., Morris, J., and Fletcher, R., 2012. Application of seismic and sequence stratigraphic concepts to a lava-fed delta system in the Faroe-Shetland Basin, UK and Faroes. Basin Research, 24(1):91–106. **https://doi.org/10.1111/j.1365-2117.2011.00513.x**

Zastrozhnov, D., Gernigon, L., Gogin, I., Abdelmalak, M.M., Planke, S., Faleide, J.I., Eide, S., and Myklebust, R., 2018. Cretaceous-Paleocene evolution and crustal structure of the northern Vøring margin (offshore mid-Norway): results from integrated geological and geophysical study. Tectonics, 37(2):497–528. **https://doi.org/10.1002/2017TC004655**

Zastrozhnov, D., Gernigon, L., Gogin, I., Planke, S., Abdelmalak, M.M., Polteau, S., Faleide, J.I., Manton, B., and Myklebust, R., 2020. Regional structure and polyphased Cretaceous-Paleocene rift and basin development of the mid-Norwegian volcanic passive margin. Marine and Petroleum Geology, 115:104269. **https://doi.org/10.1016/j.marpetgeo.2020.104269**

Ziegler, P.A., and Cloetingh, S., 2004. Dynamic processes controlling evolution of rifted basins. Earth-Science Reviews, 64(1):1–50. **https://doi.org/10.1016/S0012-8252(03)00041-2**